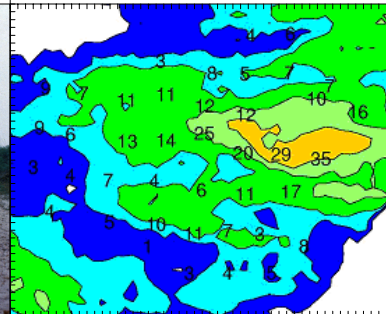


Rainfall Measurements *with the* Polarimetric WSR-88D Radar



Prepared by:
A. Ryzhkov

with contributions by:
S. Giangrande and T. Schuur

September 2003



National Oceanic and Atmospheric Administration
National Severe Storms Laboratory
Norman, Oklahoma

University of Oklahoma
**Cooperative Institute for
Mesoscale Meteorological Studies**



Contents

Preamble	2
1. Introduction	3
2. Radar data set	6
2.1 Observed rain events	6
2.2 Data processing and quality control	7
2.2.1 Data processing	7
2.2.2 Calibration of Z and Z_{DR}	10
2.2.3 Statistical measurement errors of radar variables and rainfall estimates	12
3. Polarimetric rainfall relations	13
4. Validation and optimization of polarimetric rainfall algorithms using the ARS Micronet gages	15
4.1 Statistical properties of different rainfall estimators	15
4.2 Analysis of individual events and hours of observations	29
5. The quality of rainfall estimation as a function of range	27
6. Conclusions	38
References	39
Appendix A. Effective raindrop shape and its variability	42
Appendix B. Summary of individual hours of rainfall measurements.	47

Preamble

Over the years NSSL has been providing technical information to the National Weather Service. This exchange had many forms, from formal reports and algorithms to consultations and supply of radar data in real time to the Weather Services Forecast Office. After the decision to evolve its network of WSR-88Ds to keep pace with emerging knowledge and technology, the NWS provided a spare WSR-88D to NSSL. Hence, NSSL became the principal NOAA Laboratory for evolutionary and revolutionary enhancements of weather radar science and technology. At that time (mid nineties) Doppler Radar and Remote Sensing Research group committed to document in report form all significant innovations, changes, and results deemed of special value for operational applications regardless whether such writing was formally required. This is the twelfth report in the series since 1997. It deals with polarimetric rainfall estimation with the research WSR-88D during the Joint POLarization Experiment (JPOLE) from spring of 2002 until summer of 2003. I was fortunate to share the work on the upgrade with scientists and engineers second to none. Allen Zahrai led the team of engineers who designed the new processor which enabled scanning strategies and allowed more flexibility than the old system. Mike Schmidt ably assisted with Richard Wahkinney made extensive modifications of microwave circuitry and controls. John Carter contributed to design of microwave circuits and with Valery Melnikov made numerous calibration measurements of the two channels. As always I relied on my colleague Dick Doviak for support, advice, and technical help. Alan Siggia from Sigmet resolved numerous technical details needed to operate the RVP7 processor in dual polarization mode. The Radar Operations Center (ROC) of NWS contributed the basic RVP7 processor and display, which was subsequently enhanced to process dual polarization signals.

Over the last few years modest support for this work was provided by the NWS Office of Hydrology. Furthermore, this is the first year that NWS's Office of Science and Technology specifically and generously contributed to the dual polarization effort at NSSL. Thus the report fulfils our commitment to the Office of Hydrology and is part of a cumulative contribution to the Office of Science and Technology.

September 2003 in Norman
Dusan S. Zrnica

1. Introduction.

Improvement of Quantitative Precipitation Estimation (QPE) is one of the primary benefits of a dual-polarization radar. In addition to conventional radar reflectivity factor Z , a polarimetric radar is capable to measure differential reflectivity Z_{DR} , specific differential phase K_{DP} , and the cross-correlation coefficient ρ_{hv} between two orthogonally polarized radar returns. Using multiparameter radar information instead of radar reflectivity alone helps to significantly improve the radar data quality, distinguish rain echoes from the radar signals caused by other scatterers (snow, ground clutter, insects, birds, chaff, etc.), and to reduce an impact of drop size distribution (DSD) variability on the quality of rainfall estimation. Differential reflectivity Z_{DR} is a good measure of the median drop diameter that should be taken into account for more accurate rain measurements. Among the indisputable advantages of polarimetric rainfall estimation based on specific differential phase K_{DP} is its immunity to radar miscalibration, attenuation in precipitation, and partial blockage of radar beam (Zrnice and Ryzhkov 1996).

Several different polarimetric relations for rain rate estimation have been suggested during the last two decades. These relations utilize Z , Z_{DR} , and K_{DP} in different combinations. The relations were obtained for different radar wavelengths using either simulated or measured drop size distributions (DSDs) and various assumptions about the size and shape dependence of raindrops. The performance of many suggested polarimetric rainfall estimation techniques has been tested on several extended data sets from Oklahoma (Ryzhkov and Zrnice 1996, Ryzhkov et al. 2000, Ryzhkov et al. 2002), Colorado and Kansas (Brandes et al. 2001), Florida (Brandes et al. 2002, 2003) for S-band radars, Australia (May et al. 1999) for C-band radar, and Virginia (Matrosov et al. 2002) for X-band radar.

All of the above validation studies have shown that (a) there is an improvement in rainfall estimation if a dual-polarization radar is used and (b) polarimetric rainfall estimation techniques are more robust with respect to DSD variations than are the conventional $R(Z)$ relations. At the moment, however, there is no consensus on the degree of improvement and the choice of an optimal polarization relation. The most significant improvement was reported in the latest study in Oklahoma (Ryzhkov et al. 2002) using the $R(K_{DP}, Z_{DR})$ relation. Relatively modest improvement was observed in Florida (Brandes et al. 2002, 2003a) with the best results obtained from the $R(Z, Z_{DR})$ relation.

At least two new approaches were suggested recently to further improve polarimetric rainfall estimation. One of them implies polarimetric DSD retrieval prior to calculation of rain rate. In several studies, it was shown that three parameters of a Gamma drop size distribution expressed as

$$N(D) = N_0 D^\mu \exp(-\Lambda D), \quad (1)$$

can be estimated with a good accuracy from the measured values of Z , Z_{DR} , and K_{DP} (Bringi et al. 2002a, 2003, Brandes et al. 2003b,c). In (1), N_0 ($\text{mm}^{-\mu-1}\text{m}^{-3}$) is a number concentration parameter, μ is a DSD shape parameter, Λ (mm^{-1}) is a slope term, and D (mm) is the drop equivolume diameter. Results of radar DSD retrievals were found to

agree well with direct measurements of DSD using 2D-video disdrometers (2DVD) in different field campaigns.

Three radar variables are needed to retrieve three parameters of DSD. One of the radar measurands, K_{DP} , is quite noisy at low rain rates and might be significantly biased if the radar resolution volume is not uniformly filled (Ryzhkov and Zrnich 1998). Thus, its use for the DSD retrieval might be severely limited. Bringi et al. (2002a) avoid using K_{DP} if it is less than $0.3^\circ \text{ km}^{-1}$ ($R < 20 \text{ mm h}^{-1}$) for their DSD retrieval. Brandes et al. 2002, 2003a,b,c capitalize on the fact that at least the two of DSD parameters, μ and Λ , are well correlated and there is no need to measure K_{DP} at all. The Brandes et al. technique demonstrates good quality of the DSD retrieval but doesn't show any improvement in rainfall estimation compared with the traditional $R(Z, Z_{DR})$ power law relation (Brandes et al. 2003a).

Polarimetric variables such as Z_{DR} and K_{DP} are more prone to statistical measurement errors than the conventional radar reflectivity factor Z . Additional averaging in space is required to reduce statistical errors of the K_{DP} and Z_{DR} estimates. This inevitably leads to degradation in spatial resolution. Bringi et al. (2002b) come up with an idea to combine superior spatial resolution of Z with the capability of a dual-polarization radar to capture the DSD variations by applying polarimetrically-tuned $R(Z)$ estimator of the form $Z = a R^{1.5}$ where the coefficient 'a' is continuously tuned based on measured K_{DP} and Z_{DR} .

Second approach addresses the problem of raindrop shape and orientation uncertainty that affects the performance of all polarimetric techniques for rain estimation. An assumption of equilibrium raindrop shape (Beard and Chuang 1987) has been widely used for simulating polarimetric variables in rain and deriving polarimetric relations for rainfall estimation. There is, however, mounting evidence from radar measurements that the actual average drop shape is more spherical than equilibrium drop shape (e.g., Brandes et al. 2002, Ryzhkov et al. 2001 among others). The magnitudes of K_{DP} and Z_{DR} measured with a radar are usually lower than the corresponding values computed from the DSDs obtained by a 2DVD if equilibrium raindrop shape is assumed. Also, the $R(K_{DP})$ and $R(Z, Z_{DR})$ relations derived for equilibrium axis ratios persistently underestimate and overestimate rainfall respectively. Laboratory measurements indicate that oscillating drops have a less oblate shape on average than equilibrium drops (Andsager et al. 1999). Recently, Gorgucci et al. (2000) proposed a polarimetric technique to determine the "effective" slope (β_{eff}) of the mean axis ratio versus equivolume raindrop diameter. After β_{eff} is estimated from Z , Z_{DR} , and K_{DP} , the coefficients in the polarimetric power-law relations for rain estimation are tuned in accord with β_{eff} . This technique has not been tested on a large data set and some methodological issues remain open. For example, it is not clear if the technique should be applied on a "pixel" basis, or "prevailing" β_{eff} over sufficiently large area has to be taken into account; this is because the β_{eff} estimate is rather noisy and, again, can not be obtained with confidence in the areas of light rain where the K_{DP} estimates are not reliable (see discussion in Brandes et al. (2003c)).

As part of continuous modernization of the nationwide network of the NEXRAD weather radars, the US National Weather Service considers adding polarimetric capability to existing operational radars. The proof-of-concept was tested on the NSSL's research WSR-88D radar, and its operational demonstration started in March 2002. In the

past year, the National Severe Storms Laboratory has been conducting an operational demonstration of the polarimetric utility of the KOUN WSR-88D radar. This demonstration project, referred as the Joint POLarization Experiment (JPOLE) seeks to evaluate the engineering design of the polarimetric WSR-88D radar and demonstrate the utility and feasibility of the radar data and products including rainfall estimation and hydrometeor classification.

There are at least four important practical issues regarding polarimetric rainfall estimation that have to be addressed with the polarimetric WSR-88D radar in operational environment.

First of all, the polarimetric NEXRAD prototype was designed to transmit and receive horizontally (H) and vertically (V) polarized waves - henceforth called SHV mode (Doviak et al. 2000). Although the SHV mode of operation has many advantages, it potentially may cause problems for accurate rain estimation and hydrometeor classification due to a stronger coupling between two orthogonal components of the radar return than in a conventional alternate transmission / reception mode.

Second, with few exceptions, the majority of the dual-polarization radar - gage comparisons were made for warm season precipitation and at distances less than 100 km from the radar. It is important to assess the performance of polarimetric rainfall estimation techniques at larger distances, especially for cold season precipitation when bright band contamination and overshooting of precipitation by the radar beam are more likely to occur.

Third, most polarimetric data in the previous research studies were collected with relatively slow antenna rotation rates (usually not exceeding 1 rpm). This was dictated by the need to reduce statistical measurement errors and isolate them from the rain estimation errors due to other physical factors. Routine NEXRAD volume scanning strategies (VCP) imply at least three times higher antenna rotation rates and shorter dwell times. Therefore, the algorithms for polarimetric rainfall estimation should be tested with VCPs consistent with existing NEXRAD VCPs.

Fourth issue is selection of the rainfall estimation algorithm that is optimal and robust for operational environment. In this study, we try to capitalize on the most recent ideas for polarimetric rainfall estimation and, at the same time, make the algorithm reasonably simple, understandable, and suitable for real-time implementation.

One of the NWS requirements for the JPOLE is to demonstrate compatibility of the polarimetric WSR-88D prototype with existing operational WSR-88D radars, i.e., to show that existing capabilities of the WSR-88D radar are not compromised with adding polarization diversity. This implies comparison of the quality of non-polarimetric radar variables (radar reflectivity, mean Doppler velocity, and spectrum width) and radar products (including rain accumulations) obtained from the KOUN radar and the reference operational radar. Operational KTLX WSR-88D radar was used as a non-polarimetric reference radar. The KTLX radar is located at about 20 km NE from the polarimetric prototype (Fig. 1a). Rainfall products from both radars are compared and validated using two raingage networks: the Oklahoma Mesonet and the Agricultural Research Service (ARS) Micronet. The Mesonet network numbers 115 gages with average gage spacing of 30 km, whereas the Micronet consists of 42 gages with average spacing of 5 km (Fig. 1b). Both networks provide 5-minute rain accumulation data.

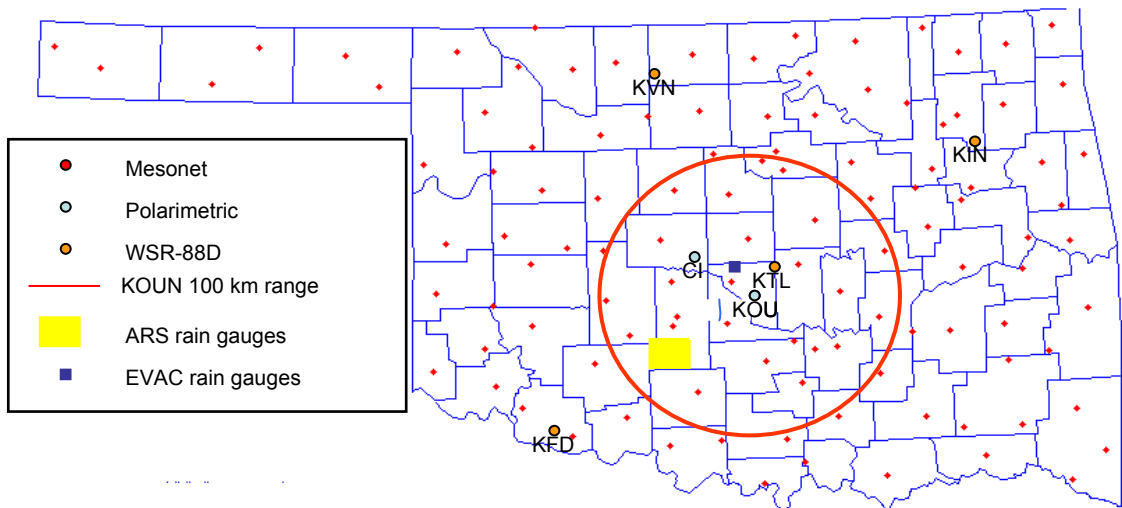


Fig. 1a Instrumentation for rainfall measurements in Oklahoma

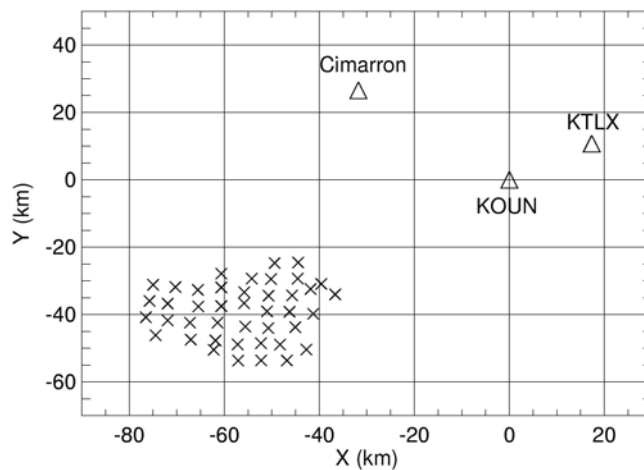


Fig. 1b Radar locations with respect to the ARS micronetwork

2. Radar data set.

2.1 Observed rain events

Data collection with the WSR-88D KOUN prototype dual-polarized radar started on 19 March 2002. Since then, the polarimetric data have been collected and archived for about 100 days of observation. Ancillary data from the operational KTLX WSR-88D radar have been collected for the majority of precipitation events. We have selected for in-depth analysis two big datasets. One of them consists of 24 rain events with 50 hours of observations for which the ARS gages recorded sizeable amount of precipitation. A list of these rain events that were observed during the period from June 2002 to June 2003 is presented in Table 1. Fig. 2a illustrates number of rain events and hours of observations

for different months during the JPOLE. The data set contains 18 convective and 6 stratiform rain events. Both "warm season" and "cold season" rain events are well represented in this data set. "Cold season" stratiform rain with relatively low bright band mostly occurred in the month of October, 2002.

Table 1. List of rain events for which the ARS gages have been used for ground validation.

Number	Date	Time (hour, UTC)	Type of event
1	06/13/02	16 - 17	Stratiform part of MCS
2	06/16/02	2 - 4	MCS
3	08/14/02	1 - 4	Clustered convection
4	09/08/02	18 - 21	Tropical rain
5	09/09/02	16 - 17	Tropical rain
6	09/14/02	7 - 9	Convective bands
7	09/19/02	4 - 6	MCS
8	10/08/02	17 - 20, 22 - 23	Stratiform rain
9	10/09/02	1 - 3, 13 - 14	Stratiform rain
10	10/19/02	19 - 20, 21 - 22	Stratiform with embedded convection
11	10/23/02	16 - 17	Weak convective rainbands
12	10/24/02	15 - 17, 19 - 21	Stratiform rain
13	10/27/02	13 - 14	Stratiform rain
14	10/28/02	19 - 20	Squall line
15	12/03/02	22 - 23	Stratiform rain
16	12/04/02	1 - 2	Stratiform rain
17	04/19/03	11 - 13	Squall line
18	04/23/03	22 - 23	Convective cells with hail
19	05/14/03	7 - 9	Convective rain with large hail
20	05/20/03	2 - 5	Convective rain with hail
21	06/05/03	10 - 13, 14 - 15	MCS
22	06/06/03	3 - 6	Squall line
23	06/12/03	2 - 3	MCS
24	06/13/03	11 - 13	Convective rain

Similar radar data set for comparisons with the Mesonet gages is illustrated in Table 2 and Fig. 2b. The second data set is comprised of 22 rain events and 83 hours of observations for the cases observed from August 2002 to June 2003. 108 Oklahoma Mesonet gages were used to validate the results of radar rain measurements in a broad range of distances between 25 and 290 km from the radar.

2.2 Radar data processing and quality control.

2.2.1 Data processing

Radar variables Z , Z_{DR} , K_{DP} , and ρ_{hv} were estimated using quite short dwell time (48 radar samples) in order to satisfy the NEXRAD requirement for rapid antenna rotation rate (3 rpm) and the 1° azimuthal resolution. Update times for rain rate estimates,

however, were different for the cases observed in 2002 and 2003. In 2002, volume coverage pattern (VCP) included only two lowest elevation tilts: 0.5° and 1.5° , whereas in 2003 the VCP consisting of 14 – 15 elevation angles was implemented. Thus, the update times for rain rate estimates were about 2 and 6 minutes in 2002 and 2003 respectively.

Table 2. List of rain events for which the Oklahoma Mesonet gages have been used for ground validation.

Number	Date	Time (hour, UTC)	Type of event
1	8/14/2002	1-4	Clustered convection
2	9/8/2002	18-21	Tropical rain
3	9/9/2002	16-17	Tropical rain
4	9/14/2002	6-11	Convective bands
5	9/19/2002	2-7	MCS
6	10/8/2002	17-20, 22-23	Stratiform rain
7	10/9/2002	1-3, 4-5, 13-14	Stratiform rain
8	10/19/2002	19-20, 21-22	Straiform with embedded convection
9	10/24/2002	15-17, 19-21	Stratiform rain
10	10/28/2002	19-20	Squall line
11	4/19/2003	10-14	Squall line
12	4/23/2003	22-23	Convective rain with hail
13	5/14/2003	5-11	Convective rain with large hail
14	5/16/2003	5-10	Convective rain with large hail
15	5/20/2003	1-5	Convective rain with hail
16	6/2/2003	3-6	Convective cells
17	6/4/2003	12-14, 15-17	MCS
18	6/5/2003	10-15	MCS
19	6/6/2003	2-7	Squall line
20	6/11/2003	0-1, 2-6	Convective rain
21	6/12/2003	0-5	MCS
22	6/13/2003	10-14	Convective rain

The KOUN radar data processor RVP7 provides raw multiparameter data including radar reflectivity at horizontal polarization Z , differential reflectivity Z_{DR} , cross-correlation coefficient ρ_{hv} , and total differential phase Φ_{DP} with range resolution of 267 m (corresponding to sampling rate of the RVP7) and azimuthal resolution of about 1° . Total number of range gates depends on VCP. Maximal number of gates is 1125.

Raw radar data are processed in the following order.

1. Z , Z_{DR} , and ρ_{hv} are smoothed along the radial using averaging windows of 3, 5, and 5 gates respectively.
2. Z_{DR} and ρ_{hv} are corrected for noises in the two orthogonal channels.

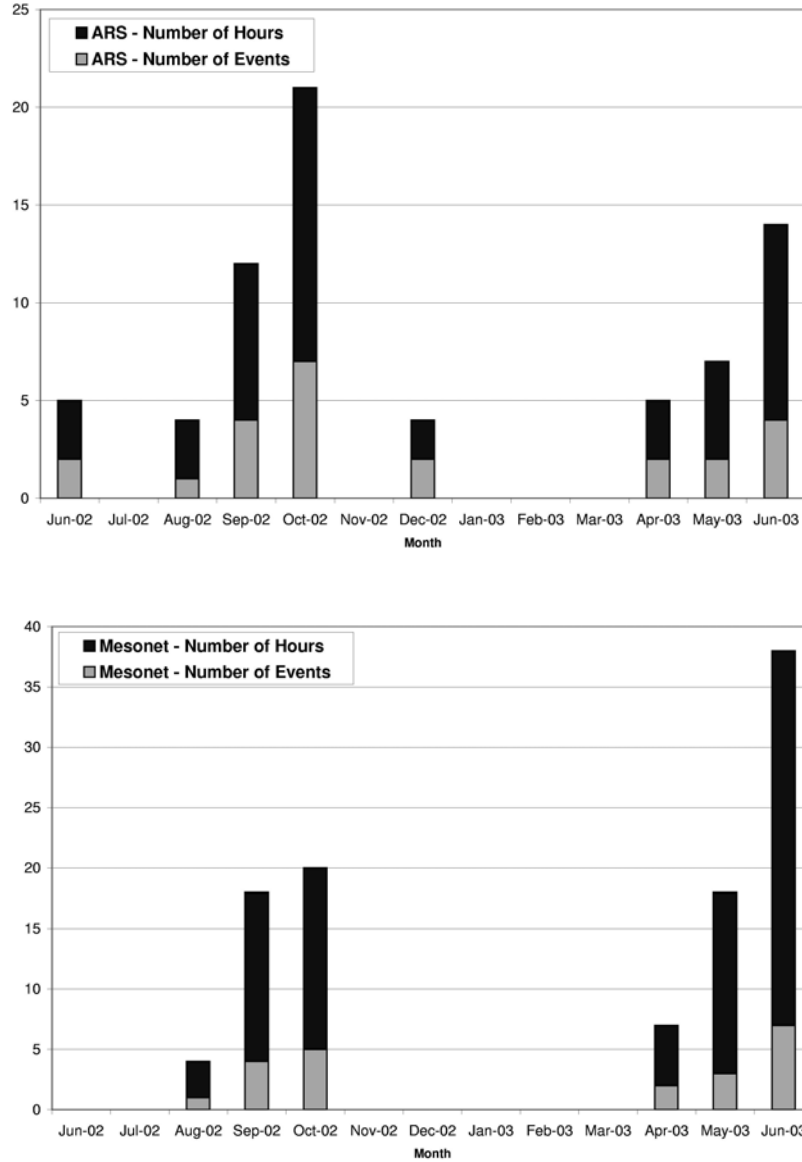


Fig 2. Monthly distribution of rain events and hours of observations during JPOLE that are used for comparisons with (a) ARS gages and (b) Oklahoma Mesonet gages.

3. Total differential phase Φ_{DP} is edited, unfolded, and smoothed along the radial using two averaging windows corresponding to 9 and 25 successive gates. Thus, “lightly filtered” and “heavily filtered” radial profiles of Φ_{DP} are obtained. The need for unfolding differential phase is dictated by the fact the RVP7 processor allows to measure Φ_{DP} unambiguously only within the 180° range although unambiguous estimates of Φ_{DP} within the 360° interval are possible in the simultaneous transmission / reception mode of operation. This problem is supposed to be fixed in the RVP8 data processor.
4. Z and Z_{DR} are corrected for attenuation using “heavily filtered” Φ_{DP} and simple relations ΔZ (dB) = 0.04 Φ_{DP} (deg) and ΔZ_{DR} (dB) = 0.004 Φ_{DP} (deg) (Ryzhkov and Zrnich 1995a).

5. Two estimates of specific differential phase K_{DP} are obtained from the filtered Φ_{DP} as a slope of a least squares fit for two range averaging intervals corresponding to 9 and 25 successive gates. For any particular range gate, the “lightly filtered” estimate of K_{DP} is selected if $Z < 40$ dBZ, and “heavily filtered estimate” otherwise (Ryzhkov and Zrnice 1996). Thus, radial resolution of the K_{DP} estimate is about 6 km for relatively light rain ($R < 12$ mm h⁻¹) and about 2 km for more intense rain.
6. The estimates of Z and K_{DP} are converted into rain rates $R(Z)$ and $R(K_{DP})$ for each gate.
7. The ρ_{hv} threshold of 0.85 is used to filter out the echoes of non-meteorological origin (ground clutter, AP, biological scatterers, chaff, etc).
8. For radar-gage comparisons, the estimates of $R(Z)$, $R(K_{DP})$, and Z_{DR} are subjected to additional averaging over two radials and 5 range gates closest to the gage. This means that the gage rain total is compared to the radar estimate averaged over an area of about 1 km x 1° centered on the gage.

2.2.2 Calibration of Z and Z_{DR} .

Radar reflectivity calibration for the KOUN radar was performed either by matching one-hour areal rainfall estimate using the standard $R(Z)$ algorithm with the one obtained from the operational KTLX radar, or by applying a polarimetric consistency technique (Goddard et al. 1994, Gorgucci et al. 1999). The latter capitalizes on interdependence of Z , Z_{DR} , and K_{DP} in rain medium. According to this approach, radar reflectivity factor can be roughly estimated from Z_{DR} and K_{DP} using the following relation

$$Z = a + b \log(K_{DP}) + c Z_{DR} \quad (2)$$

where Z is expressed in dBZ, Z_{DR} – in dB, and K_{DP} – in deg/km. The coefficients a , b , and c in (2) depend on a radar wavelength, the assumption about raindrop shape, and are relatively insensitive to the DSD variations. Since K_{DP} can be quite noisy, especially in light rain, it is more convenient to solve Eq (1) for K_{DP} as a function of Z and Z_{DR} and examine its integral, the total differential phase

$$\Phi_{DP}^{est}(R) = 2 \int_0^R K_{DP}(Z, Z_{DR}) dr \quad (3)$$

Radial profile of the measured differential phase Φ_{DP} is then compared to the radial profile of estimated differential phase Φ_{DP}^{est} . If the radar is perfectly calibrated then the two radial profiles should be very close to each other in rain medium. The mismatch between these two profiles indicates possible calibration error of Z . This error can be determined as an adjustment to Z that is required to match the two profiles of differential phase. This method works only if differential phase is sufficiently large. In our methodology, we require that there are sufficient number of rays for which maximal Φ_{DP} is larger than 20°, i.e, there is enough rain along the ray.

We have examined different consistency relations available in literature, derived our own based on the existing statistics of DSD measurements in central Oklahoma, and finally came up with the one that is well matched with local DSD statistics and gives results that are consistent with the estimates from direct comparisons with the KTLX radar (see details in Appendix A). In this relation, $a = 48.5$, $b = 11.4$, and $c = 0.94$. Fig. 3

illustrates results of Z calibration obtained from direct comparisons with the KTLX radar and from the polarimetric self-consistency technique. The two curves that characterize a bias of Z obtained from two methods show high degree of correlation.

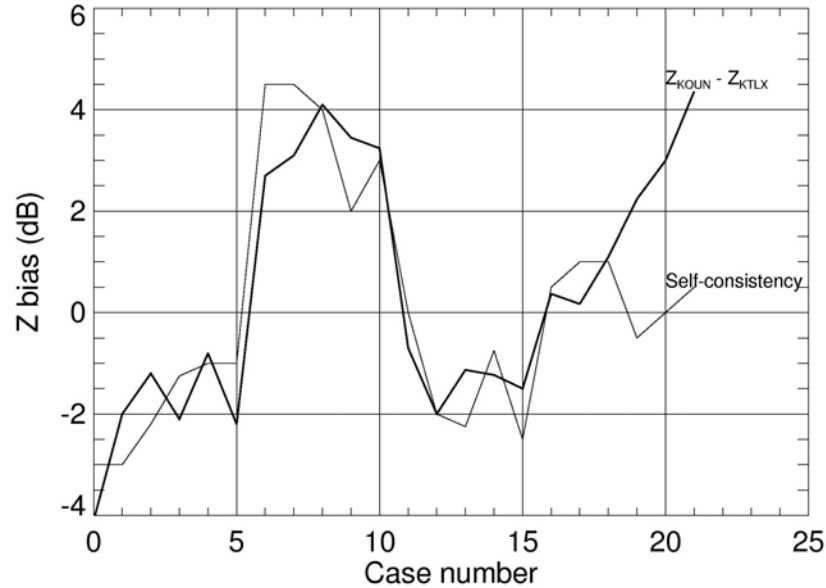


Fig. 3 Results of the estimation of the Z bias from (a) direct comparisons between the KOUN and KTLX WSR-88D radars and (b) polarimetric self-consistency test for different rain cases ranked in chronological order.

Although high correlation between two estimates gives us more confidence in the self-consistency method, we can not draw ultimate conclusions about its accuracy because the KTLX radar is not an ideal validation tool. There are numerous indications that the KTLX radar itself experienced certain calibration problems in the past (Ryzhkov et al. 2002) and is not completely free of them now (Gourley et al. 2003). In our assessment of the Z calibration bias, we use an average of the two bias estimates (from KTLX and self-consistency) if they do not differ by more than 2 dB and resort to the one from the comparison with the KTLX radar if the discrepancy is larger or precipitation is light and the self-consistency procedure is not applicable.

Differential reflectivity Z_{DR} was calibrated as described by Melnikov et al. (2003). There are several approaches to calibrate Z_{DR} . They include the use of test signals in two orthogonal channels, sun checks, and weather targets with known and low-varying intrinsic Z_{DR} . We can not use the measurements with vertically pointing antenna to estimate the overall system bias of Z_{DR} as suggested by Bringi and Chandrasekar (2001) because the WSR-88D radar can elevate its antenna only up to 60° . Routine comparisons of the results of Z_{DR} calibration using different techniques show that the system differential reflectivity was estimated with an accuracy better than 0.2 dB (Melnikov et al. 2003).

2.2.3 Statistical measurement errors of radar variables and rainfall estimates.

The accuracy of rainfall estimates is affected by the measurement errors of radar variables. Here we analyze the uncertainty of the one-hour rain total estimates due to statistical measurement errors of Z , Z_{DR} , and K_{DP} . The standard error of Z estimate depends on a dwell time and Doppler spectrum width σ_v , whereas the measurement errors of Z_{DR} and total differential phase Φ_{DP} are also substantially affected by the magnitude of the cross-correlation coefficient ρ_{hv} .

For dwell time corresponding to 48 successive pulses (about 0.1 s for low pulse repetition frequency (PRF) of 446 Hz and 0.05 s for high PRF of 1013 Hz typically used for the KOUN radar), the standard error of Z varies between 1 and 2 dB depending on σ_v (Bringi and Chandrasekar 2001). Our observations show that typical values of ρ_{hv} in pure rain are within 0.985 – 0.995 range at relatively close distances from the radar where the radar resolution volume is not too big. Theoretical analysis in (Bringi and Chandrasekar 2001) and our experimental estimates show that for such values of ρ_{hv} and 48 pairs of simultaneous H and V radar samples the standard error of differential reflectivity $SD(Z_{DR})$ is between 0.2 and 0.3 dB and the standard error of total differential phase $SD(\Phi_{DP})$ varies from 1° to 2°. The magnitude of ρ_{hv} tends to decrease with range mainly due to effects of non-uniform beam filling. Therefore, those accuracies degrade with distance from the radar, especially in the regions of high azimuthal and vertical gradients of Φ_{DP} .

The standard deviation of K_{DP} estimate can be expressed as (Ryzhkov and Zrnich 1996)

$$SD(K_{DP}) = \frac{\sqrt{3} SD(\Phi_{DP})}{N^{3/2} \Delta r} \quad (4)$$

where Δr is the range gate spacing, and N is the number of range samples in the least squares fit. It follows from (4) that if $SD(\Phi_{DP}) = 1 - 2^\circ$ and $\Delta r = 0.267$ km, then the standard error $SD(K_{DP})$ is $0.052 - 0.104$ ° km⁻¹ for “highly filtered” K_{DP} and $0.24 - 0.48$ ° km⁻¹ for “lightly filtered” K_{DP} .

The corresponding standard errors of rain rate estimates obtained from the standard $R(Z)$ algorithm

$$R(Z) = 1.70 \cdot 10^{-2} \cdot 10^{0.0714 Z} \quad (5)$$

and a simple one-parameter polarimetric $R(K_{DP})$ algorithm (see justification in section 4)

$$R(K_{DP}) = 45.3 |K_{DP}|^{0.786} \text{sign}(K_{DP}) \quad (6)$$

are shown in Table 3. Because the $R(Z)$ and $R(K_{DP})$ relations are nonlinear, the standard errors of rain rates depend on Z or R . In Table 3, the RMS errors of rain rates are given for individual range gates, i.e., for radial resolution of 0.267 km. The RMS errors of hourly rain totals, however, are represented for the estimates that are obtained after averaging over 5 gates and 2 radials as specified in the step 8 of the data processing

scheme. We also assume that hourly rain totals are computed from 10 radar scans updated every 6 minutes and rain is uniform in time and space. Because hourly rain total

Table 3. Standard errors of rain rates (R) and hourly accumulations (T) for the R(Z) and R(K_{DP}) algorithms. SD(R) are expressed in mm h⁻¹, SD(T) – in mm.

Standard error	Z = 35 dBZ R(Z) = 5.4 mm h ⁻¹	Z = 40 dBZ R(Z) = 12 mm h ⁻¹	Z = 45 dBZ R(Z) = 28 mm h ⁻¹	Z = 50 dBZ R(Z) = 63 mm h ⁻¹
SD(R(Z))	0.9 – 1.9	2.0 – 4.0	4.4 – 8.9	10.1 – 20.2
SD(R(K _{DP}))	3.3 – 6.6	2.6 – 5.3	9.8 – 19.5	7.8 – 15.6
SD(T(Z))	0.09 – 0.019	0.2 – 0.4	0.44 – 0.89	1.01 – 2.02
SD(T(K _{DP}))	0.74 – 1.40	1.72 – 3.44	2.19 – 4.36	1.74 – 3.48

from R(Z) is computed after averaging over 10 gates and 10 scans, SD(T(Z)) (mm) = SD(R(Z)) (mm h⁻¹) / (10 x 10)^{1/2}. Intrinsic radial resolution of the R(K_{DP}) estimates is much coarser than the one for the R(Z) estimate. Therefore, the estimates of R(K_{DP}) in 5 successive range gates are not independent. The corresponding estimates at two adjacent azimuths are independent, however. As a result, spatial averaging of the R(K_{DP}) estimates does not produce reduction of their statistical errors similar to R(Z). Consequently, SD(T(K_{DP})) (mm) = SD(R(K_{DP})) (mm h⁻¹) / (2 x 10)^{1/2}.

Although an assumption about uniform temporal and spatial distribution of rain is idealistic, the corresponding estimates in Table 3 give a general idea about the impact of radar measurement errors on the quality of rainfall estimates during the JPOLE campaign. It is obvious that at lower rain rates the standard errors of T(K_{DP}) are almost an order of magnitude larger than respective errors of T(Z). This is a leading argument to avoid using K_{DP}-based relations for estimation of light rain. The difference between SD(T(Z)) and SD(T(K_{DP})) is not as large for more intense rain. At the higher end, the advantages of the K_{DP} – based algorithms definitely outweigh their deficiencies (including relatively large statistical errors) and make them more attractive than the conventional R(Z) relation.

Here we examined only two simplest one-parameter algorithms: R(Z) and R(K_{DP}). As can be shown later, the polarimetric relations containing Z_{DR} in combination with Z or K_{DP} prove to be more efficient for radar rainfall measurements. The impact of measurement errors in Z_{DR} on the performance of such algorithms depends on the concrete form of these relations and will be examined in more details in section 4.

3. Polarimetric rainfall relations.

Two groups of polarimetric rainfall algorithms have been tested. One group includes most recent power law R(K_{DP}), R(Z, Z_{DR}), and R(K_{DP}, Z_{DR}) relations that we found in literature for S-band radars. Another group consists of similar algorithms that we derived using multi-year statistics of DSD measurements in central Oklahoma.

Four different assumptions about raindrop shape – size dependencies were made: (1) equilibrium shapes defined by Beard and Chuang (1987), (2) “oscillating raindrop” shapes from Bringi et al (2003), (3) shapes specified by Brandes et al. (2002), and (4)

linear dependence of the drop axis ratio on equivolume diameter. An average slope $\beta = 0.052 \text{ mm}^{-1}$ of a linear dependence was found by Ryzhkov and Schuur (2003) from polarimetric radar observations using the approach described by Gorgucci et al. (2000) (see more details in Appendix A). In all simulations, we assumed that the drops are canted with the mean canting angle equal to zero and the width of the canting angle distribution of 10° . 17470 one-minute DSDs measured with the NSSL's 2D-video disdrometer have been used for computation of radar variables and derivation of polarimetric relations for rainfall estimation. A list of algorithms is presented in Table 4.

Table 4. List of different polarimetric algorithms used for rainfall estimation.

$R(K_{DP}) = a K_{DP} ^b \text{sign}(K_{DP})$					
	a	b	<i>Assumptions</i>		<i>Source</i>
1	50.7	0.85	Simulated DSD, equilibrium shape		BC (2001)
2	54.3	0.806	Measured DSD (FL), Brandes' shape		BZV (2002)
3	51.6	0.71	Simulated DSD, Goddard's shape		IB (2002)
4	44.0	0.822	Measured DSD (OK), equilibrium shape		NSSL
5	50.3	0.812	Measured DSD (OK), Bringi's shape		NSSL
6	45.3	0.786	Measured DSD (OK), Brandes' shape		NSSL
7	52.2	0.875	Measured DSD (OK), linear ($\beta = 0.052$)		NSSL
$R(Z, Z_{DR}) = a Z^b Z_{DR}^c$					
	a	b	c	<i>Assumptions</i>	<i>Source</i>
8	$6.70 \cdot 10^{-3}$	0.927	-3.43	Simulated DSD, equilibrium shape	BC (2001)
9	$7.46 \cdot 10^{-3}$	0.945	-4.76	Measured DSD (FL), Brandes' shape	BZV (2002)
10	$7.11 \cdot 10^{-3}$	1.0	***	Simulated DSD, Goddard's shape	IB (2002)
11	$1.42 \cdot 10^{-2}$	0.770	-1.67	Measured DSD (OK), equilibrium shape	NSSL
12	$1.59 \cdot 10^{-2}$	0.737	-1.03	Measured DSD (OK), Bringi's shape	NSSL
13	$1.49 \cdot 10^{-2}$	0.752	-1.24	Measured DSD (OK), Brandes' shape	NSSL
14	$1.41 \cdot 10^{-2}$	0.802	-3.43	Measured DSD (OK), linear ($\beta = 0.052$)	NSSL
$R(K_{DP}, Z_{DR}) = a K_{DP} ^b Z_{DR}^c \text{sign}(K_{DP})$					
	a	b	c	<i>Assumptions</i>	<i>Source</i>
15	90.8	0.93	-1.69	Simulated DSD, equilibrium shape	BC (2001)
16	136	0.968	-2.86	Measured DSD (FL), Brandes' shape	BZV (2002)
17	52.9	0.852	-0.53	Measured DSD (OK), equilibrium shape	NSSL
18	63.3	0.851	-0.72	Measured DSD (OK), Bringi's shape	NSSL
19	68.6	0.915	-1.01	Measured DSD (OK), linear ($\beta = 0.052$)	NSSL

$$*** c = -8.14 + 1.385 Z_{DR} - 0.1039 Z_{DR}^2$$

In table 4, the notation Z_{dr} is used for differential reflectivity expressed in linear scale, whereas Z_{DR} is expressed in logarithmic units; BC (2001) means Bringi and Chandrasekar (2001), BZV (2002) - Brandes et al (2002), and IB (2002) – Illingworth and Blackman (2002). Equilibrium, Bringi's, and Brandes' shapes of raindrops are described in Appendix A, whereas the Goddard's axis ratio is given by formula (Goddard et al. 1995)

$$a/b = 1.075 - 0.065 D - 0.0036 D^2 + 0.0004 D^3 \quad (7)$$

where D is an equivolume diameter expressed in mm.

We compare one-hour rain totals obtained from the radar and gages belonging to both networks: the ARS Micronet and Oklahoma Mesonet. Point and areal estimates of the one-hour rain accumulation are examined. By point estimate we mean an hourly total averaged over small-size area ($1 \text{ km} \times 1^\circ$) centered on individual gage. Areal mean hourly total or areal mean rain rate is determined as a sum of hourly accumulations from all gages that recorded rain divided by the number of such gages. Areal rain totals were estimated only for the ARS Micronet.

To assess the quality of different polarimetric rain algorithms, we prefer to examine absolute differences between radar and gage estimates (expressed in mm) rather than standard fractional errors which are heavily weighted by small accumulations. Rainfall estimates are characterized by the bias $B = \langle \Delta \rangle$, standard deviation $SD = \langle |\Delta - B|^2 \rangle^{1/2}$, and the rms error $RMSE = \langle |\Delta|^2 \rangle^{1/2}$, where $\Delta = T_R - T_G$ is a difference between radar and gage hourly totals for any given radar – gage pair and brackets mean averaging over all such pairs.

4. Validation and optimization of polarimetric rainfall algorithms using the ARS Micronet gages.

4.1 Statistical properties of different rainfall estimates.

First we examined the performance of different polarimetric algorithms for the ARS Micronet area. The ARS gages are located at the distances between 50 and 88 km from the dual-polarization KOUN WSR-88D radar and 70 to 108 km from the conventional KTLX WSR-88D radar. In this range interval, the DSD variability and raindrop shape uncertainty are two leading factors affecting the accuracy of polarimetric radar rain retrievals. Ground clutter and bright band contamination are usually negligible at these distances from the radar. Regular ground clutter (without AP) contaminates rain measurements up to 20 – 25 km from the KOUN radar if the ground clutter canceller (eliminating radar echoes in the close proximity of the zero Doppler velocity) is not activated. We did not use ground clutter canceller in the KOUN observations during the JPOLE. As will be shown in Section 5 of this report, in Oklahoma, bright band contamination typically becomes a serious problem starting at about 120 km from the radar. Therefore, the comparison of radar rainfall estimates with the ARS rain gages can be used for optimization of polarimetric algorithms mainly with respect to the DSD variations. After optimal rainfall estimators are selected at relatively close distances, we will examine their performance at longer ranges using the Mesonet gages as a ground truth.

We started our testing from the simplest one-parameter algorithms $R(Z)$ and $R(K_{DP})$. The standard NEXRAD relation is used as the $R(Z)$ algorithm

$$R(Z) = 1.70 \cdot 10^{-2} Z^{0.714} \quad (8)$$

where Z is expressed in $\text{mm}^6 \text{m}^{-3}$, R – in mm h^{-1} . Values of Z were thresholded at the level of 53 dBZ in order to mitigate hail contamination. Biases, standard deviations, and RMS

errors of the point and areal radar rainfall estimates for the conventional and different polarimetric relations listed in Table 4 are summarized in Table 5.

There is an obvious overall improvement in rainfall estimation when we switch from $R(Z)$ to $R(K_{DP})$ regardless of a particular form of the $R(K_{DP})$ relation. Among seven $R(K_{DP})$ relations, algorithms 4 and 6 are characterized by smallest SD and RMSE. From

Table 5. Mean biases, standard deviations, and RMS errors of the radar estimates of one-hour rain totals (in mm) and areal mean rain rates (in mm h^{-1}) for different radar rainfall algorithms.

Algorithm	Point			Areal	
	Bias (mm)	SD (mm)	RMSE (mm)	SD(mm/h)	RMSE (mm/h)
$R(Z) = 1.70 \cdot 10^{-2} Z^{0.714}$					
	1.26	5.37	5.51	3.96	4.24
$R(K_{DP}) = a K_{DP} ^b \text{sign}(K_{DP})$					
1	0.07	4.37	4.37	2.80	2.80
2	0.76	4.75	4.81	3.16	3.27
3	1.01	4.36	4.48	2.76	2.97
4	-0.65	3.65	3.71	2.05	2.13
5	0.21	4.27	4.28	2.70	2.72
6	-0.31	3.74	3.75	2.15	2.16
7	0.14	4.59	4.60	3.01	3.02
$R(Z, Z_{DR}) = a Z^b Z_{dr}^c$					
8	1.13	4.52	4.66	2.51	2.80
9	0.22	4.00	4.01	1.67	1.69
10	0.79	4.71	4.77	2.28	2.44
11	-0.30	3.25	3.27	1.79	1.80
12	-0.24	3.45	3.46	2.06	2.06
13	-0.18	3.42	3.43	2.02	2.02
14	-1.69	3.53	3.91	1.99	2.58
$R(K_{DP}, Z_{DR}) = a K_{DP} ^b Z_{dr}^c \text{sign}(K_{DP})$					
15	-0.57	3.33	3.38	1.58	1.66
16	-0.69	3.44	3.51	1.35	1.51
17	-0.88	3.32	3.44	1.68	1.87
18	-0.25	3.58	3.59	1.99	2.00
19	-0.71	3.39	3.47	1.76	1.88

these two, we select the relation

$$R(K_{DP}) = 45.3 |K_{DP}|^{0.786} \text{sign}(K_{DP}) \quad (9)$$

that produces smaller bias and compare its performance with the performance of the conventional $R(Z)$ algorithm in more detail.

One-hour individual gage rain accumulations versus their estimates from the $R(Z)$ and $R(K_{DP})$ algorithms defined by Eq (8) and (9) are plotted for all 50 hours of

observations over the ARS Micronet in Fig. 4. The corresponding scatterplots for mean areal rain rates are shown in Fig. 5. Several conclusions can be drawn from these two figures. First, the $R(K_{DP})$ relation apparently outperforms the conventional $R(Z)$ algorithm for larger hourly accumulations (> 20 mm). Although, the $R(K_{DP})$ algorithm produces slight positive bias at higher rain rates and totals, it is much smaller than the one for the $R(Z)$ method. There is also significantly less scatter for the $R(K_{DP})$ estimates for large rain accumulations. This improvement is particularly obvious for areal accumulations, i.e., at larger spatial scale. On the contrary, both algorithms tend to underestimate small hourly totals ($< 3 - 4$ mm) with the $R(K_{DP})$ formula producing larger scatter due to larger statistical measurement errors of K_{DP} (see Table 3).

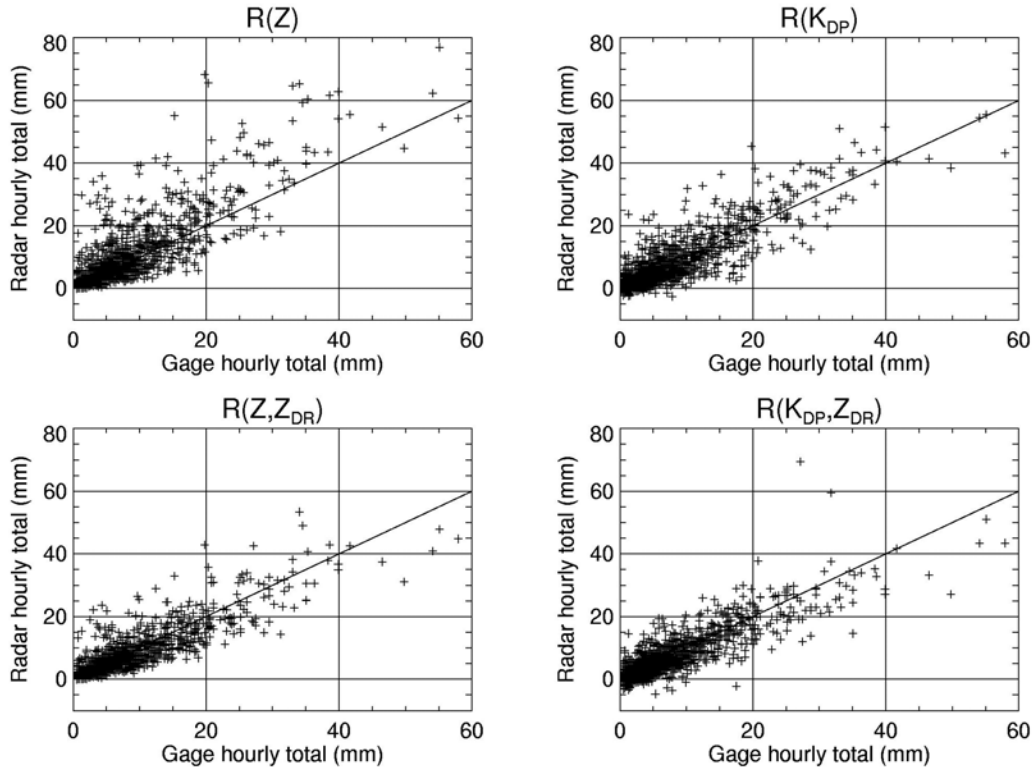


Fig. 4 One-hour individual gage rain accumulations versus their estimates from different radar rainfall algorithms (24 rain events, 50 hours of observations).

Notable are high correlation between these two rainfall estimates and their strong dependence on the net value of differential reflectivity $\langle Z_{DR} \rangle$ that is defined as a weighted average Z_{DR} for a particular hour over a whole gage network

$$\langle Z_{DR} \rangle = \frac{\sum_{i,j} R^{i,j}(Z) Z_{DR}^{i,j}}{\sum_{i,j} R^{i,j}(Z)}, \quad (10)$$

where superscript i characterizes scan number within the one-hour time interval and superscript j stands for gage number. Because differential reflectivities associated with

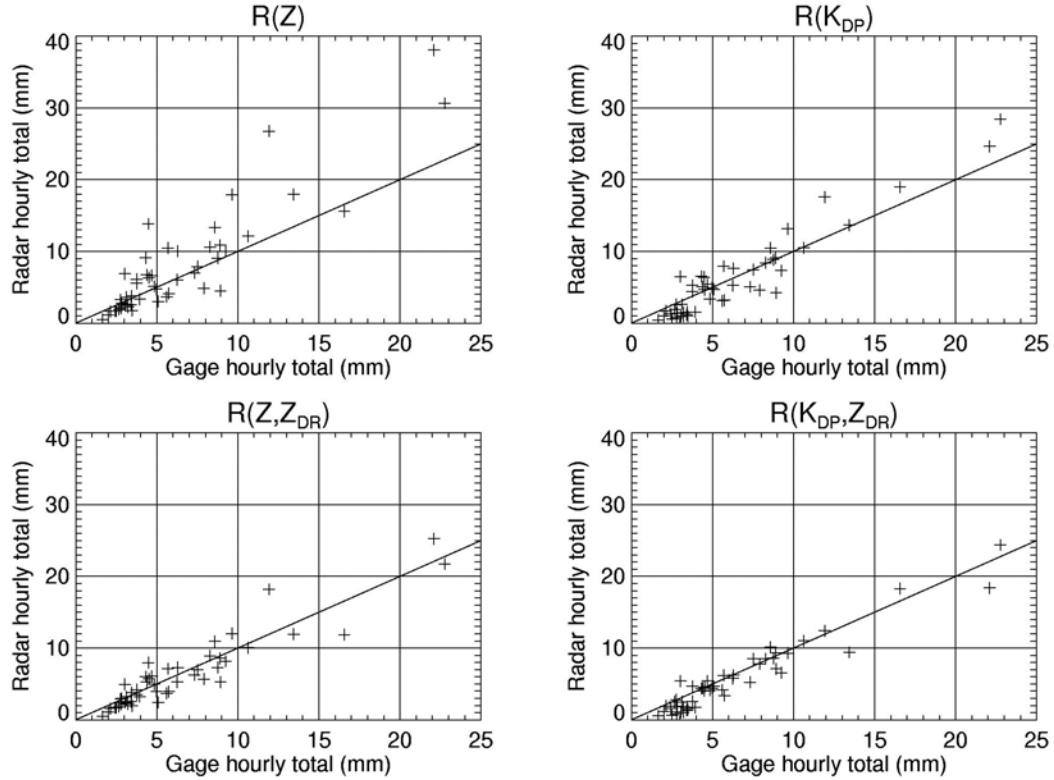


Fig. 5 Mean areal rain rates from gages versus their estimates from different radar rainfall algorithms (24 rain events, 50 hours of observations).

larger rain rates are more important to characterize rain regime and its impact on the total rain estimation than the ones associated with light rain, each Z_{DR} measurement is weighted proportionally to rain rate computed from the $R(Z)$ relation. Thus, the net Z_{DR} characterizes most intense part of rain for a given hour in the gage area. Fig. 6 shows the net Z_{DR} , as well as the ratios of hourly areal totals obtained from the radar and gages as functions of hour of observations ranked in a chronological order.

It is quite clear from Fig. 6 that both $R(Z)$ and $R(K_{DP})$ tend to underestimate rain in which DSD is dominated by smaller drops (low Z_{DR}) and overestimate it if rain is characterized with large raindrop median diameter (high Z_{DR}). For a cold season stratiform rain that is characterized by the net Z_{DR} values less than 0.8 dB, the K_{DP} -based algorithm produces larger negative bias than the conventional one. For a warm season convective rain with high Z_{DR} , the $R(K_{DP})$ estimate is much less sensitive to the median raindrop diameter than its conventional counterpart. In the case of heavy rain associated with large hail on 14 May 2003 ($x = 36$ in Fig. 6), $T_R(Z)/T_G = 3.1$, whereas $T_R(K_{DP})/T_G = 1.4$. The observed dependencies of $T_R(Z)/T_G$ and $T_R(K_{DP})/T_G$ on $\langle Z_{DR} \rangle$ have simple physical explanation. As was pointed out by Ryzhkov and Znic (1996), for larger drop sizes $K_{DP} \sim D^{4.24}$, whereas for smaller drop sizes $K_{DP} \sim D^{5.6}$ where D is an equivolume raindrop diameter. The rain rate is approximately proportional to the 3.67th moment of the DSD. Therefore, at those lower rain rates in which drops are mostly small, the $R(K_{DP})$ relation is more susceptible to the variations in the DSD than at higher rain rates. In fact, for light rain and small drops the $R(K_{DP})$ estimates are not less sensitive to the DSD

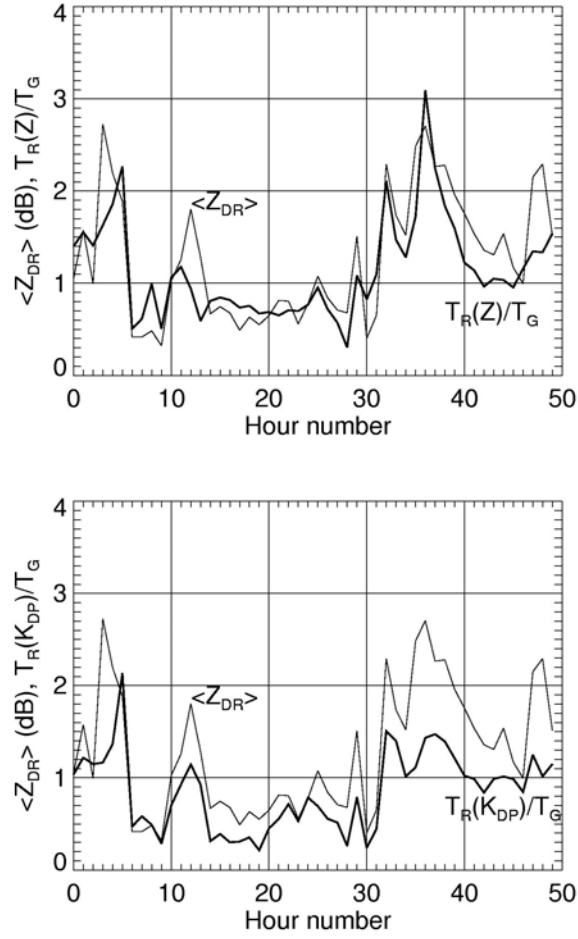


Fig. 6 Net Z_{DR} and ratios of mean areal rain rates from radar versus hour of observations.

variations than the $R(Z)$ estimates. Moreover, even very small changes in the shape of small drops produce large variations in rainfall estimates computed from K_{DP} . Well pronounced dependence of the performances of the $R(Z)$ and $R(K_{DP})$ algorithms on the net Z_{DR} leads to the conclusion that Z_{DR} should be involved in rain measurements in combination with Z or K_{DP} . As a next step, we tested various two-parameter algorithms $R(Z, Z_{DR})$ and $R(K_{DP}, Z_{DR})$ listed in Table 4. After examining the performance of those two-parameter polarimetric algorithms (see Table 5), we selected the best ones for each category (algorithms 11 and 16 in Table 2):

$$R(Z, Z_{DR}) = 1.42 \cdot 10^{-2} Z^{0.770} Z_{dr}^{-1.67} \quad (11)$$

and

$$R(K_{DP}, Z_{DR}) = 136 |K_{DP}|^{0.968} Z_{dr}^{-2.86} \text{sign}(K_{DP}), \quad (12)$$

where Z_{dr} is differential reflectivity expressed in linear units. Eq (11) was derived using a local DSD statistics with the assumption of equilibrium drop shapes, whereas Eq (12) was taken from Brandes et al. (2002). Note that among $R(Z, Z_{DR})$ relations the algorithm

9 also demonstrates good performance with smallest bias and lowest RMSE in areal estimates. This algorithm, however, is not as good as algorithm 11 (Eq 11) in terms of the RMSE for point rain measurements. In the category of the $R(K_{DP}, Z_{DR})$ algorithms, the algorithm 15 is almost on a par with the algorithm 16 given by Eq (12). The scatterplots characterizing the performance of the algorithms (11) and (12) for point and areal rain measurements are presented in Fig. 4 and 5.

Although both algorithms (11) and (12) produce slightly larger negative biases in rain measurements, they apparently outperform the one-parameter algorithms in terms of standard deviation and RMS errors (Table 5). The $R(K_{DP}, Z_{DR})$ algorithms perform better than the $R(Z, Z_{DR})$ relations for areal rain estimation and higher rain rates, whereas the $R(Z, Z_{DR})$ algorithm is a leading contender at low rain rates where the K_{DP} estimates are quite noisy. Since both Z and Z_{DR} are strongly affected by the presence of hail, one has to be very cautious using these variables for estimation of heavy rain which is likely contaminated with hail. Switching to the $R(K_{DP})$ relation for this type of rain is a reasonable solution.

Which pair of radar variables is preferable to use for moderate rain – Z - Z_{DR} or K_{DP} - Z_{DR} ? Justification for such choice can be drawn from Fig. 7 that shows the

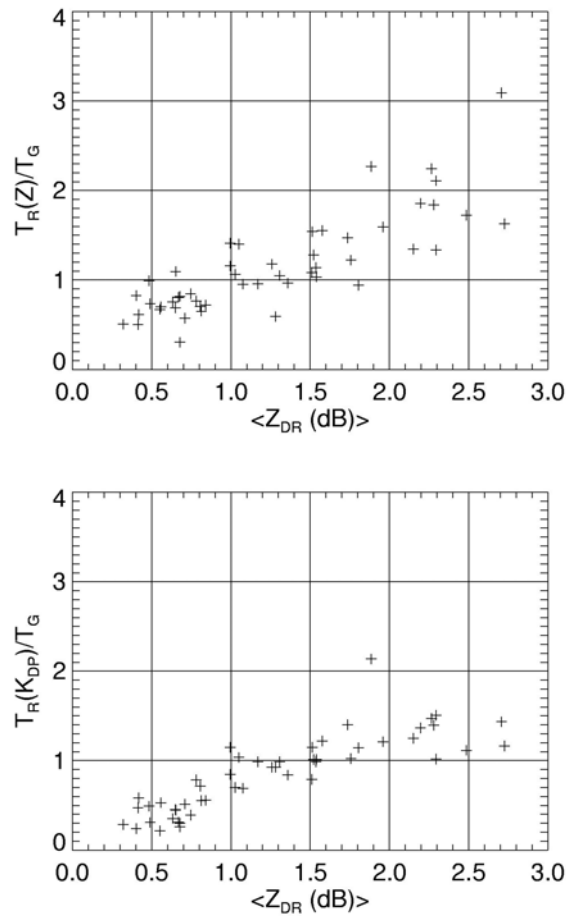


Fig.7. Scatterplots of the ratios of mean areal rain rates obtained from radar and gages versus net Z_{DR} .

scatterplots of $T_R(Z)/T_G$ and $T_R(K_{DP})/T_G$ versus $\langle Z_{DR} \rangle$. The ratio $T_R(K_{DP})/T_G$ exhibits noticeably tighter dependence (less scatter) on the net differential reflectivity than the ratio $T_R(Z)/T_G$. This means that we may achieve better success in eliminating a dependency of results for rain estimation on the median drop diameter (or DSD variations) if the K_{DP} - Z_{DR} pair is selected.

Using such reasoning and combining the merits of different algorithms for various rain intensities, we came up with the “synthetic” algorithm that suggests the use of different combinations of radar variables depending on rain rate estimated with the conventional $R(Z)$ relation. We denote the synthetic algorithm as a $R(Z, K_{DP}, Z_{DR})$ relation. The following is a description of the proposed algorithm.

If $R(Z) < 6 \text{ mm h}^{-1}$, then

$$R = R(Z)/(0.4+5.05 (Z_{dr} - 1)^{1.17}) ; \quad (13)$$

if $6 < R(Z) < 50 \text{ mm h}^{-1}$, then

$$R = R(K_{DP})/(0.4+3.48 (Z_{dr} - 1)^{1.72}) ; \quad (14)$$

If $R(Z) > 50 \text{ mm h}^{-1}$, then $R = R(K_{DP})$,

where $R(Z)$ and $R(K_{DP})$ are determined by Eq (4) and (5). The expressions (13) and (14) were obtained empirically by finding best fit to the dependences $T_R(Z)/T_G = f(\langle Z_{dr} \rangle)$ and $T_R(K_{DP})/T_G = f(\langle Z_{dr} \rangle)$ i.e., using the approach described by Fulton et al (1999). Only a portion of a whole data set was used for such matching. This subset consists of rain events observed in 2002 and accounts for about 49% of total rain in a whole data set.

The $R(Z, K_{DP}, Z_{DR})$ algorithm is structured in such a way that the combination of K_{DP} and Z_{DR} is used for estimation of about half of all rainfall in Oklahoma according to the DSD statistics. It is known from simulations that the $R(K_{DP}, Z_{DR})$ algorithm is least affected by DSD variations and uncertainties in raindrop shapes and canting compared to the $R(Z)$, $R(K_{DP})$, and $R(Z, Z_{DR})$ relations. At lower rain rates ($< 6 \text{ mm h}^{-1}$), the combination of K_{DP} and Z_{DR} is less efficient because K_{DP} becomes too noisy. Therefore, Z (instead of K_{DP}) should be used jointly with Z_{DR} . For very high rain rates ($> 50 \text{ mm h}^{-1}$), both Z_{DR} and Z are very likely contaminated with hail, and the synthetic algorithm relies exclusively on K_{DP} .

Another advantage of such approach is that reflectivity calibration is required only for light rain (with intensity less than 6 mm h^{-1}) that accounts for about 32% of annual rain in Oklahoma. Successful use of the synthetic polarimetric algorithm requires well calibrated differential reflectivity. According to (13) and (14), the Z_{DR} bias of 0.1 dB results in a fractional error of rain rate measurement $\Delta R/R$ of about 9 – 15% for light rain and 7 – 9% for moderate rain. This fractional error decreases with increasing rain rate. Note that the Z bias of 1 dB corresponds to $\Delta R/R = 16\%$ if the conventional $R(Z)$ relation is applied. Thus, it can be concluded the Z bias of 1 dB is roughly equivalent to the Z_{DR} bias of 0.2 dB. Our experience shows that since differential reflectivity is a relative parameter (a ratio), it is easier to keep the bias of Z_{DR} under 0.2 dB than to guarantee the accuracy of radar reflectivity measurements better than 1 dB (Melnikov et al. 2003).

It is not surprising that the $R(Z, K_{DP}, Z_{DR})$ algorithm outperforms all others according to all 5 statistical criteria: it has lowest bias, standard deviations, and RMS errors for point and areal rainfall estimates (Table 6). Fig. 8 shows scatterplots of hourly totals obtained from the $R(Z)$ and $R(Z, K_{DP}, Z_{DR})$ relations versus one-hour gage

Table 6. Mean biases, standard deviations, and RMS errors of the radar estimates of one-hour rain totals (in mm) and areal mean rain rates (in mm h^{-1}) for the best radar rainfall algorithms in each category defined by Eq 8,9,11,12,13 and 14.

<i>Algorithms</i>	<i>Point</i>			<i>Areal</i>	
	Bias (mm)	SD (mm)	RMSE (mm)	SD (mm/h)	RMSE (mm/h)
$R(Z)$	1.26	5.37	5.51	3.96	4.24
$R(K_{DP})$	-0.31	3.74	3.75	2.15	2.16
$R(Z, Z_{DR})$	-0.30	3.25	3.27	1.79	1.80
$R(K_{DP}, Z_{DR})$	-0.69	3.44	3.51	1.35	1.51
$R(Z, K_{DP}, Z_{DR})$	0.09	3.09	3.09	1.13	1.14

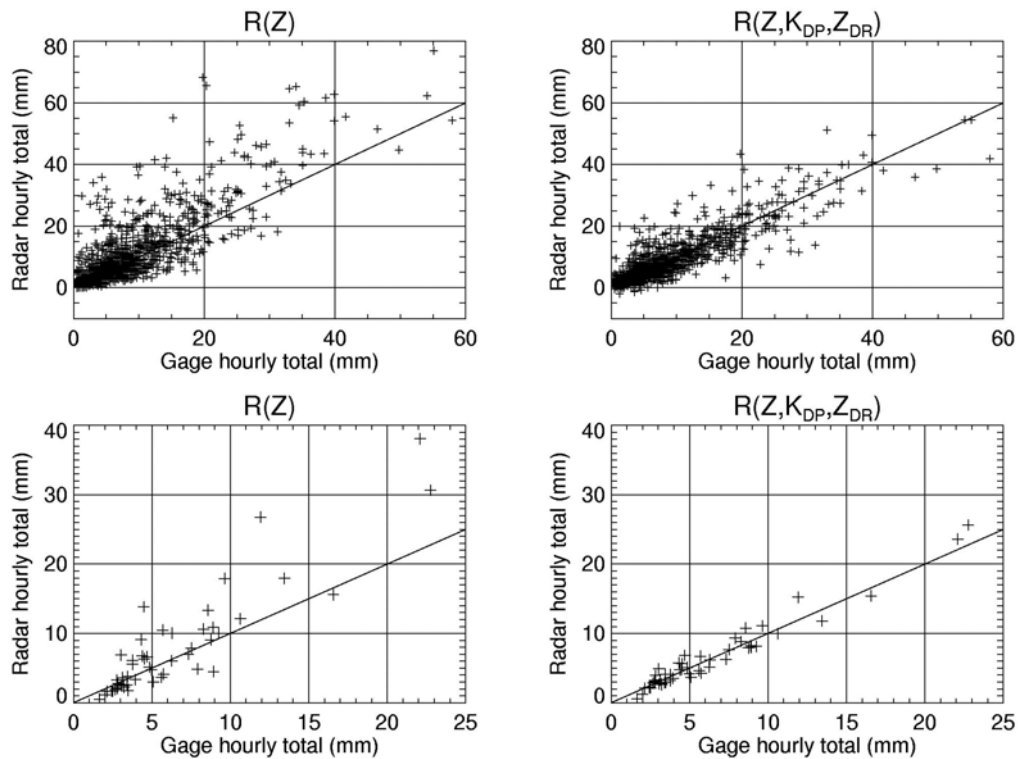


Fig. 8 One-hour individual gage accumulations and mean areal rain rates from gages versus their estimates from the $R(Z)$ and $R(Z, K_{DP}, Z_{DR})$ algorithms (24 rain events, 50 hours of observations).

accumulations for individual radar-gage comparisons and areal estimations. The optimal polarimetric algorithm has very small overall bias and demonstrates significant reduction of the RMS errors compared to the conventional rainfall estimator – 1.78 times for point measurements and 3.72 times for areal rainfall estimates.

Although the synthetic algorithm was initially “tuned up” for the 2002 part of the whole data set, it proves to be equally efficient for the second, 2003 portion of the JPOLE data set. Our subsequent comparisons with the mesonet gages also confirm superiority of the synthetic algorithm (see section 5). Fig. 9 shows the bias in areal rain rates estimated from radar using the $R(Z)$ and $R(Z, K_{DP}, Z_{DR})$ relations versus hour of observations

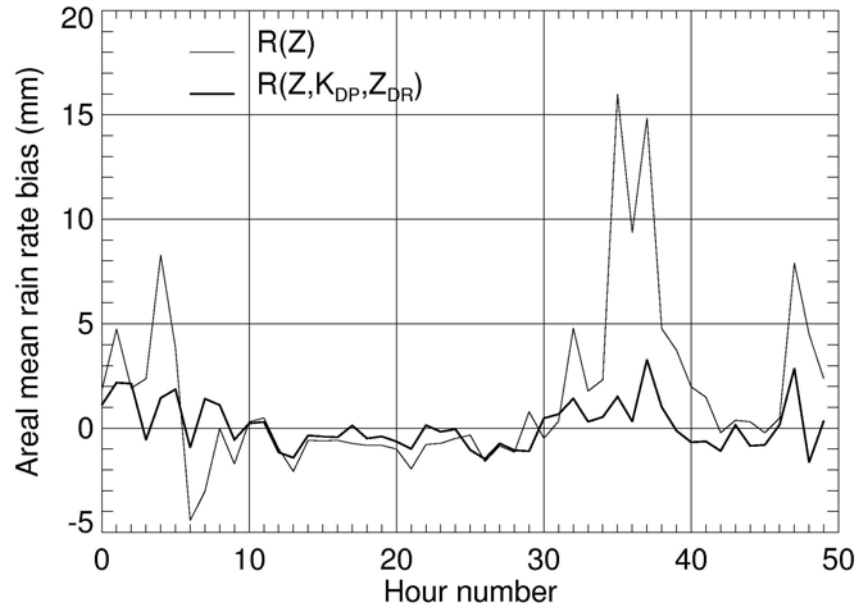


Fig. 9. The bias in areal rain rates estimated from radar using the $R(Z)$ and $R(Z, K_{DP}, Z_{DR})$ versus hour of observations ranked in chronological order.

ranked in chronological order. The two curves in Fig. 9 illustrate overall overestimation / underestimation of rain with both algorithms for different seasons and rain regimes. It is obvious that the conventional algorithm tends to significantly overestimate rainfall associated with intense convection and especially with hail. The suggested polarimetric method dramatically reduces such overestimation. Both methods slightly underestimate rain for cold season stratiform events with marginal improvement if the polarimetric algorithm is used (hours 10 to 30 – October / December 2002).

It is evident from Fig. 9 that the overall statistical properties of the two rainfall estimators are heavily weighted by convective precipitation during warm season, and the lion’s share of the improvement due to application of dual polarization is attributed to heavy convective precipitation. We do not exclude that in different geographical areas where rain originated from hail is less likely than in Oklahoma, the use of polarimetric rain measurements may not lead to such remarkable and indisputable improvement as in the US Great Plains that are notorious for severe weather. Notable is good performance of the NCAR’s polarimetric relations 9 and 16 from Table 4 that are among the best in the categories of $R(Z, Z_{DR})$ and $R(K_{DP}, Z_{DR})$. These relations have been matched with the measured DSDs in Florida where a dominant mechanism for rain formation is different than in Oklahoma. The fact that they perform well in Oklahoma points to more universal nature of the polarimetric rainfall algorithms. In other words, polarimetric relations

probably need much less “geographical or climatological tuning” compared to the conventional $R(Z)$ estimator.

Fig. 10 gives graphical representation of the relative performance of different types of rainfall estimators if the point and areal RMS errors are used as criteria. Biggest reduction in the RMS errors is achieved after switching from the $R(Z)$ algorithm to the $R(K_{DP})$ estimator. Further optimization of the dual-polarization algorithm (adding Z_{DR})

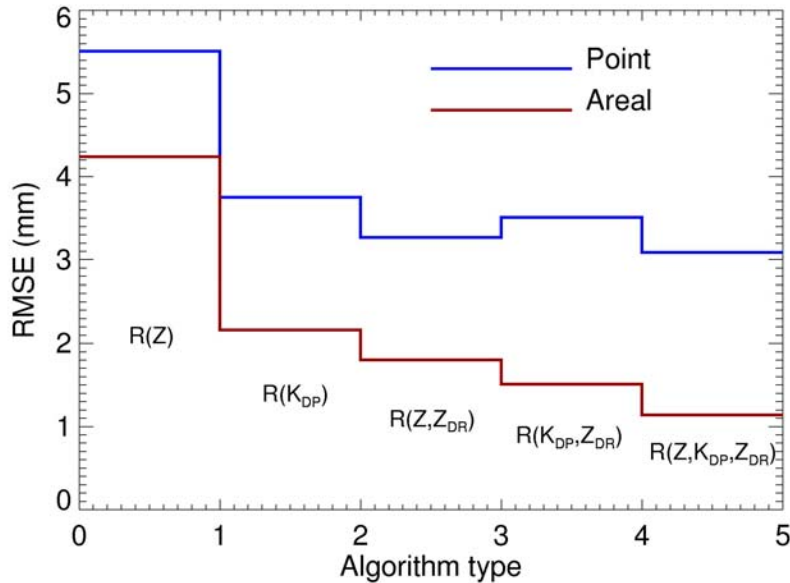


Fig. 10. RMS errors of point and areal estimates of rain for different radar rainfall algorithms.

results in additional improvement although not as dramatic as during the first step. Additional sophistication of the polarimetric algorithm yields better payoff in areal rainfall estimation for which the transition from the $R(K_{DP})$ algorithm to the optimal one doubles reduction of the RMS error. The corresponding improvement in point estimates is more modest. Note that the $R(Z, Z_{DR})$ algorithm outperforms the $R(K_{DP}, Z_{DR})$ estimator for point measurements, but the opposite is true for areal estimates. This is another confirmation of the fact the K_{DP} -based algorithms are better suited for bigger watershed areas.

4.2 Analysis of individual rain events and hours of observations.

We have examined in detail the performance of the conventional and polarimetric $R(Z, K_{DP}, Z_{DR})$ algorithms for each individual hour of observation (out of total 50). The summary of such assessment is presented in Appendix B. Each hour of rain measurements is characterized by a composite plot containing the scatterplots of hourly rain totals from gages versus their estimates from the $R(Z)$ and $R(Z, K_{DP}, Z_{DR})$ algorithms, $Z - Z_{DR}$ scattergrams, and a map of hourly radar totals with gage totals superposed on it. A table containing the biases, standard errors, and RMS errors in hourly rain totals

obtained from conventional and polarimetric algorithms for each particular hour is attached to each plot in Appendix B.

If the RMS error that combines both bias and spread of scattergram is chosen as a major criterion of the quality of rain measurements, then the polarimetric algorithm outperforms the conventional one for 21 rain events out of 24. In the remaining one convective (06/06/03) and two stratiform events (12/03/02 and 12/04/02) with very light rain, the polarimetric estimate is only slightly worse than the estimate from radar reflectivity factor. This means that the overall polarimetric improvement is not solely due to heavy precipitation with hail and is not at the expense of deterioration of lighter rainfall estimates.

a. Evidence of different rain regimes

The $Z - Z_{DR}$ scattergrams give insight into microphysical properties of rain and the type of drop size distributions. For a given Z , very large values of Z_{DR} generally indicate the DSDs skewed towards bigger drops, whereas very small values of Z_{DR} mean a dominance of small drops. A slope of the $Z - Z_{DR}$ scattergram and its spread are good predictors of rainfall overestimation / underestimation if the $R(Z)$ relation is used. Quite often two distinct clusters of the $Z - Z_{DR}$ pairs are evident in the scattergrams (see Figs. B1, B9, B10, B21, B27, B30 as best examples). This happens most frequently in stratiform rain with embedded relatively weak convection. Raindrops in the stratiform part of the storm usually originate from big snowflakes in the melting layer, whereas the weak convective cells are dominated with drops produced by smaller size graupel. Therefore, convective elements are characterized by smaller values of Z_{DR} for the same Z compared to their stratiform counterparts. There is no way for any $R(Z)$ relation to “match” both rain regimes in relatively small spatial / temporal domain. The polarimetric method, however, automatically accounts for these microphysical distinctions and, therefore, can estimate rain more accurately.

b. Tropical rain events

At least two consequent rain events on 8 and 9 September 2002 could be associated with tropical or extratropical air mass (Fig. B7 – 10). They are characterized by very “flat” $Z - Z_{DR}$ scattergrams and pronounced underestimation of rainfall if the conventional algorithm is used. It is interesting that the observed values of Z_{DR} do not exceed 1 dB even for reflectivities reaching 50 dBZ. Application of the polarimetric method results in significant improvement and there is no need to switch to a “tropical” $R(Z)$ relation to “match” this rain regime.

c. Rain contaminated with hail

It is well known that low values of Z_{DR} associated with high Z (usually exceeding 50 dBZ) likely signify hail mixed with rain. The $Z - Z_{DR}$ couplet is routinely used for polarimetric hail detection. Such signatures can be identified in Figs. B13,36,38,39,48, and 49. It is probably less known and realized that hail cores are typically surrounded by regions of very high Z_{DR} that can be attributed to melting hail or giant raindrops with ice

cores inside. The contribution of such areas to rain total usually is much larger than the one from “genuine hail-contaminated regions” as can be deduced from the corresponding $Z - Z_{DR}$ scatterplots. For example, in the case of rain mixed with hail on 14 May 2003 (Fig. B36) the number of points that might be qualified as rain / hail mixture ($Z > 50$ dBZ and $Z_{DR} < 1.5$ dB) comprises relatively small portion of total number of points in the $Z - Z_{DR}$ scattergram.

The $Z - Z_{DR}$ scattergrams for rain mixed with hail are extremely broad, i.e., very high values of Z_{DR} are observed in a wide range of reflectivities including very low ones. This explains why thresholding of Z at certain level (53 dBZ accepted for the WSR-88D radars) only partially mitigates the impact of hail on the quality of rain measurement using the $R(Z)$ algorithm. We still observe substantial overestimation of rain after the 53 dBZ threshold is applied to the radar reflectivity data. Lowering the threshold even more is problematic because (a) we undersample pure rain with high reflectivity and (b) there are still many radar pixels with anomalous DSD (high Z_{DR} combined with moderate or low Z) left after thresholding of Z is applied. The combined use of Z with Z_{DR} for light rain and K_{DP} with Z_{DR} for moderate-to-heavy rain allows to substantially alleviate the uncertainty due to DSD variations.

d. Flash flood rain event on 14 May 2003.

The storm on 14 May 2003 produced flash flood in the ARS Micronet area and hail with sizes exceeding 5'' outside of the gage network. Some of the Micronet gages recorded rain rates of about 200 mm h^{-1} and at least three gages registered hourly rain totals exceeding 2''. The performance of four radar rainfall algorithms is illustrated in Fig. 11 (see also Fig. B37). As expected, the $R(Z)$ algorithm produces large positive bias in rain estimate. Although we are not absolutely confident with reflectivity calibration, we do not believe that possible positive Z bias is to blame because combining Z and Z_{DR} in the $R(Z, Z_{DR})$ algorithm almost eliminates positive bias in rain measurement. It wouldn't be likely if Z were seriously miscalibrated. This again supports our claim that rainfall overestimation with the $R(Z)$ relation in hailstorms is primarily due to abundance of large drops originated from hail and big graupel rather than due to hail itself.

e. Sampling errors.

The scattergram in Fig. 8b shows about dozen of apparent outliers (out of total 1813 points) even for the best polarimetric algorithm. Note that practically all outliers belong to only one rain event on 20 May 2003 which was characterized by extremely localized strong convection. Detailed analysis of rain accumulation fields in Fig. B38 - 40 indicates that radar - gage mismatches occur in the areas of strong gradients of rain. Bearing in mind that all hourly rain totals in 2003 were calculated from only 9 - 10 successive scans, we attribute such a discrepancy to sampling problem rather than to deficiency of the algorithm. This point can be also confirmed by the fact that the same outliers appear both in the $R(Z)$ and $R(Z, K_{DP}, Z_{DR})$ scattergrams (Fig. B6, 21, 24, 41). The influence of radar sampling is substantially alleviated in areal rain estimates (Fig. 8).

The sampling problems have larger impact on the K_{DP} -based rainfall algorithms because of large measurement errors of K_{DP} (see Table 3). Although we do not observe

apparent deterioration in polarimetric rain estimation for the 2003 rain events with update time of 6 min as opposed to the 2002 events with 3 times faster update, nonetheless, cursory examination of isolated convection suggests that more frequent sampling might be needed for application of the synthetic polarimetric algorithm. The so-called “split cut” or duplication of the lowest radar sweep during each volume scan is a conceivable option.

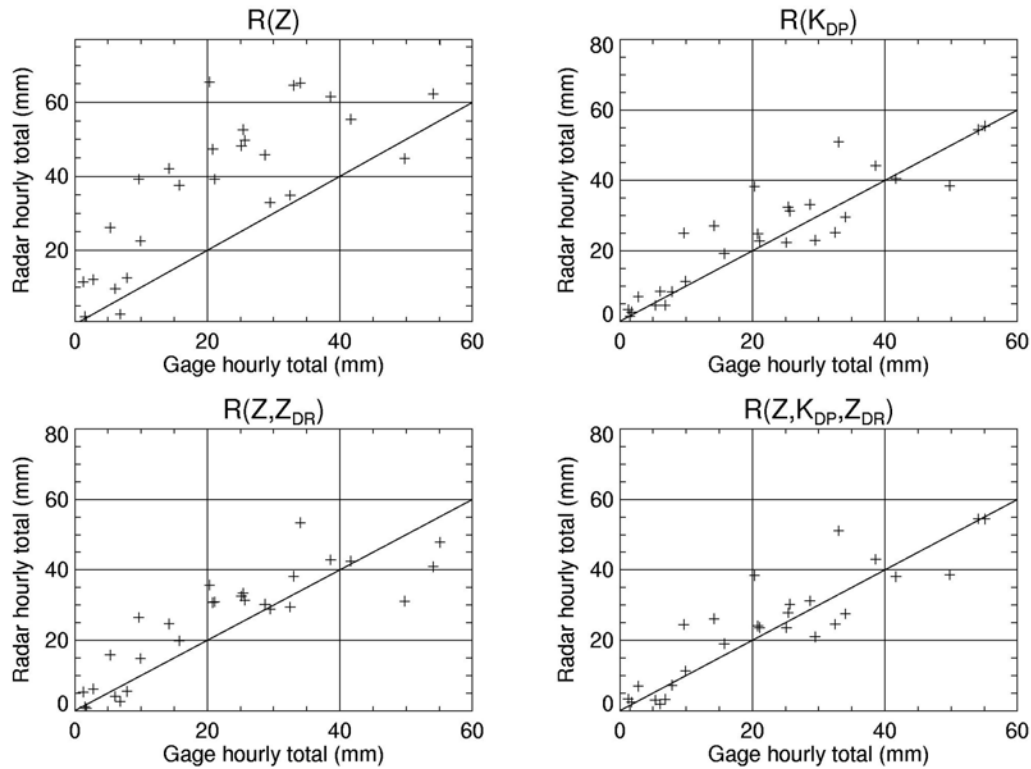


Fig. 11 One-hour individual gage rain accumulations versus their estimates from different radar algorithms for flash flood event on 14 May 2003.

5. The quality of rainfall estimation with the KOUN radar as a function of range.

The National Weather Service requires estimating rainfall at ranges up to 230 km from the radar. Rainfall estimates at large distance are especially important in regions with limited radar coverage. Having reliable rain estimates over large distances is also beneficial for validation of satellite observations since these are usually characterized by rather wide swaths.

Increased distance from the radar is often associated with a degradation of accuracy among conventional $R(Z)$ relations. Range-related errors may be significant, particularly during cold season events associated with low melting layers. Range dependence is also attributed to overshooting of precipitation, beam geometry such as beam broadening and filling, radar signal sensitivity losses, and drop size distribution (DSD) evolution in the vertical which can produce illuminated volume characteristics bearing little resemblance to the near-surface scatterers.

While some studies discuss the quality of conventional radar rain measurements at large distances (e.g., Smith et al. 1996, Seo et al. 2000), the performance of polarimetric methods at distances greater than 100 km is not well investigated. With few exceptions, the majority of the dual-polarization S-band radar - gauge comparisons were made for warm season precipitation and at distances less than 100 km. These validation studies and JPOLE observations have shown that at close distances from the radar (a) there is an improvement in rainfall estimation if a dual polarization radar is used and (b) polarimetric rainfall estimation techniques are more robust with respect to DSD variations than are conventional R(Z) relations. It is not clear if these advantages of dual polarization radar hold at larger distances from the radar.

We tested five different polarimetric algorithms that were discussed in the previous sections: R(Z), R(K_{DP}), R(Z,Z_{DR}), R(K_{DP},Z_{DR}), and R(Z,K_{DP},Z_{DR}) specified by Eq. 8-9, 11–14. As an initial step, we examine the performance of these five algorithms at close distances (<125km) from the radar to check the consistency with results obtained for the dense ARS micronetwork. Only Mesonet gauges located within 125 km from the radar were selected. The areal coverage discrepancy between these networks is substantial, therefore only point estimates for these networks are compared (Table 7).

Table 7. Mean biases, standard deviations, and RMS errors of the radar estimates of one-hour rain totals (in mm) for different radar rainfall algorithms. ARS values and Mesonet gauge values (<125 km) are listed.

Algorithm	Mesonet	Mesonet	Mesonet	ARS	ARS	ARS
	Bias	SD	RMSE	Bias	SD	RMSE
R(Z)	1.71	5.40	5.67	1.26	5.37	5.51
R(K _{DP})	-0.60	3.31	3.37	-0.31	3.74	3.75
R(Z,Z _{DR})	-0.04	3.60	3.6	-0.30	3.25	3.27
R(K _{DP} ,Z _{DR})	-1.46	3.14	3.46	-0.69	3.44	3.51
R(Z,K _{DP} ,Z _{DR})	-0.57	3.16	3.21	0.09	3.09	3.09

As can be seen in Table 7, the results obtained for the different gauge networks do not differ substantially. Similar to the results presented for the ARS network in the previous section, the R(Z,K_{DP},Z_{DR}) “synthetic” algorithm shows superior performance and outperforms the R(Z) relation by a factor of 1.77 in terms of RMSE (1.78 for the ARS Micronet). All polarimetric relations outperform the conventional R(Z) relation by at least a factor of 1.5 for SD and RMSE. Bias errors for the Mesonet and ARS are also quite similar. Note that the R(Z,Z_{DR}) algorithm gives a smallest bias followed by the “synthetic” polarimetric relation. Fig. 12 illustrates the improvement in point rain measurements if the R(Z,K_{DP},Z_{DR}) algorithm is used instead of the R(Z) relation. These results are consistent with the corresponding ARS scatterplots in Fig. 8a,b.

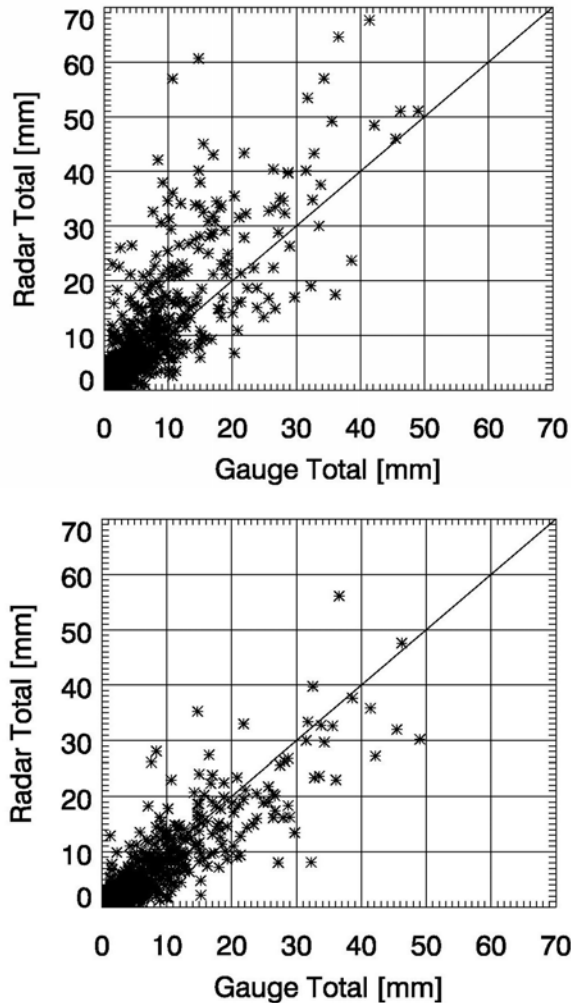


Fig. 12 One-hour rain accumulations from the Oklahoma Mesonet gages versus their radar estimates using (a) the $R(Z)$ and (b) $R(Z, K_{DP}, Z_{DR})$ algorithms. Mesonet gages are within 125 km distance from the KOUN radar.

Figure 13 shows mean bias and RMS errors of the different radar rainfall estimates in the range interval 50-225 km. Intervals of 50 km in range, centered at 25 km increments beginning with a range of 50 km, have been selected for this analysis. 83 hours of observation from all available gauges within 250 km are represented in these statistics. There are a total of 2088 hourly comparisons for the 25-250 km interval. Polarimetric algorithms outperform the conventional $R(Z)$ relation to approximately 125-150 km from the radar.

The polarimetric estimates exhibit mostly a negative bias (except the $R(Z, Z_{DR})$ relation), whereas the $R(Z)$ estimates are positively biased at all ranges. In a broad region between 125 and 200 km, all radar rainfall estimates experience steep increase of the RMS error. This is primarily attributed to bright band contamination during cold season. At the distances beyond 200 km, the performance of all algorithms rapidly deteriorates, likely due to overshooting and loss of sensitivity.

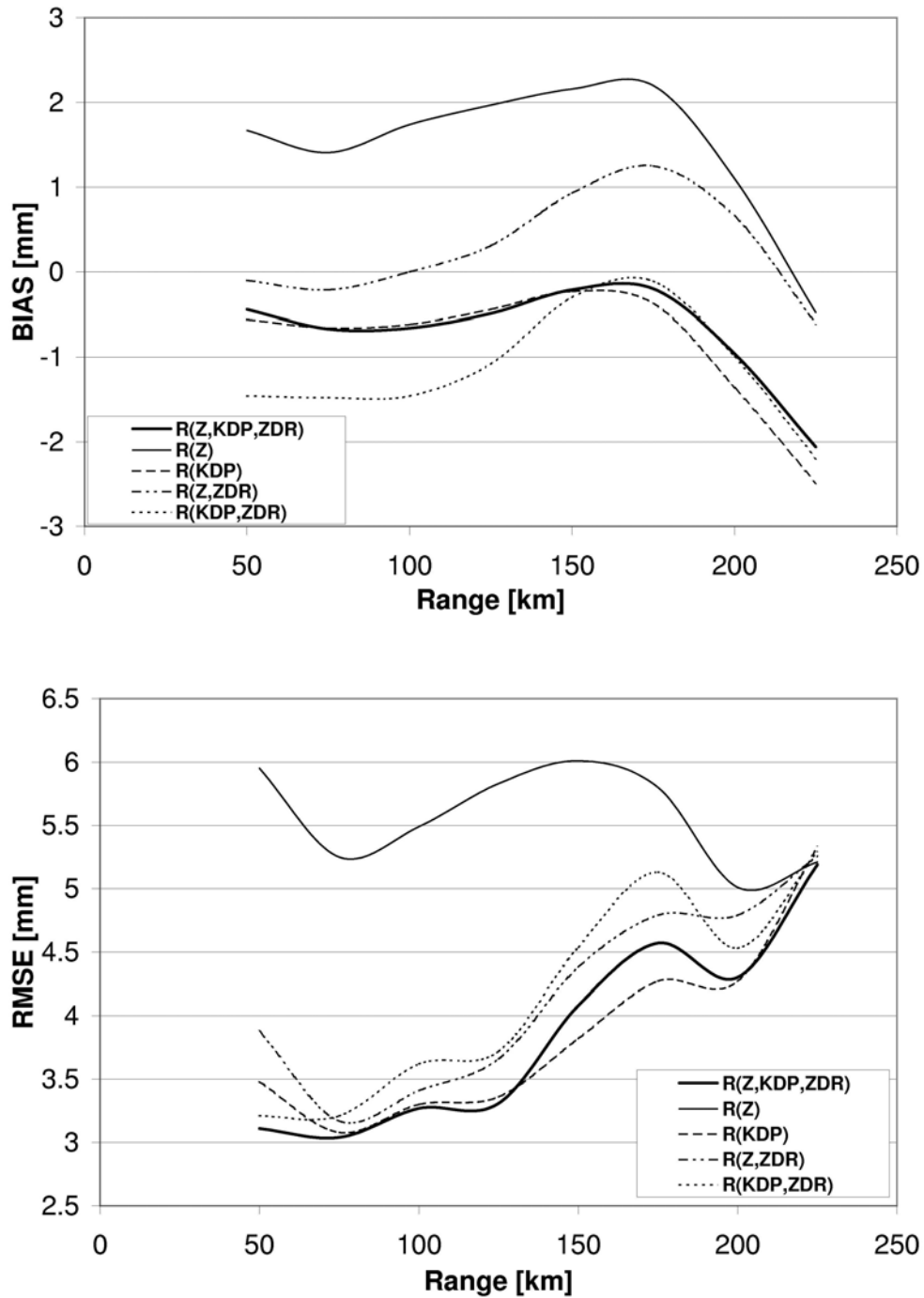


Fig. 13. Mean biases (a) and RMS errors (b) of the radar estimates as functions of range (22 rain events and 83 hours of observations).

We noticed that the performance of all radar algorithms at large distances is affected by the presence/absence of the low bright band. Separate statistics were obtained for the “cold season” events for which bright band played a significant role and the “warm season” events which were not substantially affected by the bright band. The

cold season subset contains 29 hours of observation from September through November 2002. Although these events may contain embedded convection, they are best classified as widespread stratiform precipitation and nocturnal MCS events.

Polarimetric relations outperform the $R(Z)$ relation in terms of the RMS errors at all ranges for cold season rain events (Fig. 14). The influence of the bright band contamination on rainfall estimates is very well pronounced at the distances from 130 to 200 km. It manifests itself as a positive shift in the bias and a maximum in the RMS error. The results for the $R(Z)$ relation agree with Smith et al. (1996) as it pertains to the conceptual performance of the relation for cold season events. Melting layer contamination is mitigated if the $R(K_{DP})$ relation is used. This estimate exhibits minimal bias between 125-200 km, and has the lowest RMSE and SD among other algorithms.

The “warm season” subset includes 54 hours of observation from late April to mid-August 2002-2003. These rain events are best classified as ordinary convective lines with occasional supercell convection. Some of these events have significant portions of stratiform rain. Substantial hail was reported for several warm season storms. As mentioned in the previous sections, the 2003 data for this subset were collected using 6-minute update times (rather than 2 min updates in 2002), which may impact the magnitudes of the RMS errors at long distances where spatial / temporal sampling errors become overwhelming. As expected, the bright band contamination is less pronounced than in the cold season and both the bias and RMSE exhibit more monotonic behavior with distance (Fig. 15). The Z-based algorithms tend to overestimate rain, whereas the K_{DP} -based relations progressively underestimate rainfall with distance.

At relatively close distances (less than 125 km from the radar) where bright band contamination is negligible, the quality of radar rainfall estimates is mostly determined by DSD variations and the possible presence of hail. As our analysis shows, these two problems are best addressed by the synthetic $R(Z, K_{DP}, Z_{DR})$ algorithm. It combines merits of the Z- Z_{DR} pair for light rain, the K_{DP} - Z_{DR} combination for moderate-to-heavy rain, and capitalizes on relative insensitivity of K_{DP} to the presence of hail. All polarimetric methods outperform the conventional $R(Z)$ algorithm in terms of RMS error. The $R(Z)$ relation also tends to overestimate rain during warm season (mainly due to hail contamination) even if we threshold radar reflectivity factor at the level of 53 dBZ.

In the range interval 130 – 200 km, the bright band becomes a leading factor affecting the performance of all algorithms during cold season, when rain is predominantly stratiform and the melting level is quite low. At these distances, the synthetic algorithm is no longer superior because Z and Z_{DR} are substantially affected by melting hydrometeors. Surprisingly, the $R(K_{DP})$ algorithm is more immune to the bright band contamination than the others. It performs best of all, both in terms of bias and RMS error. The situation is very different in the warm season when rain is mostly associated with strong localized convection, rain fields are very non-uniform, and bright band contamination is not a key factor. Although rain estimates based on K_{DP} are still the best in terms of the RMS error, the corresponding biases become increasingly negative. There are several possible reasons for such progressive negative bias.

First, there is possible aliasing of total differential phase Φ_{DP} at longer distances. The current RVP7 data processor enables unambiguous measurements of Φ_{DP} only up to 180° , and the dealiasing procedure does not work well all the time. Thus, we do not exclude that the overall statistics for the warm season might be affected by a few huge

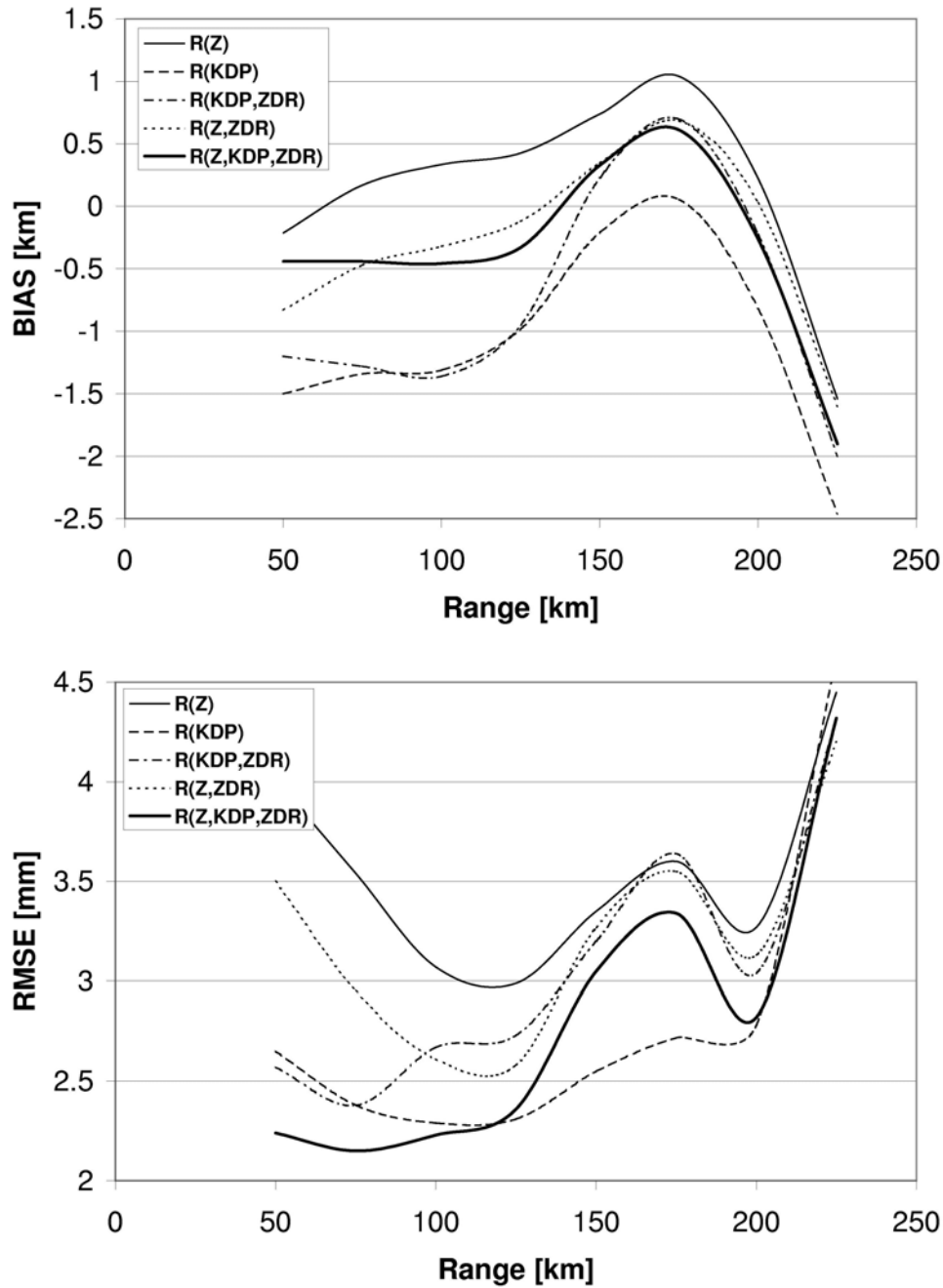


Fig. 14. Mean biases (a) and RMS errors (b) of the radar estimates as functions of range. Only cold season events are included in the statistics (29 hours of observations).

negative outliers in the K_{DP} estimates. This problem will be fixed once the existing processor is replaced by the newer one (RVP8).

Second, differential phase suffers more than any other radar variables from the non-uniform beam filling that is exacerbated at longer distances. Strong gradients of Z or Φ_{DP} within the radar resolution volume cause oscillations in the otherwise monotonic

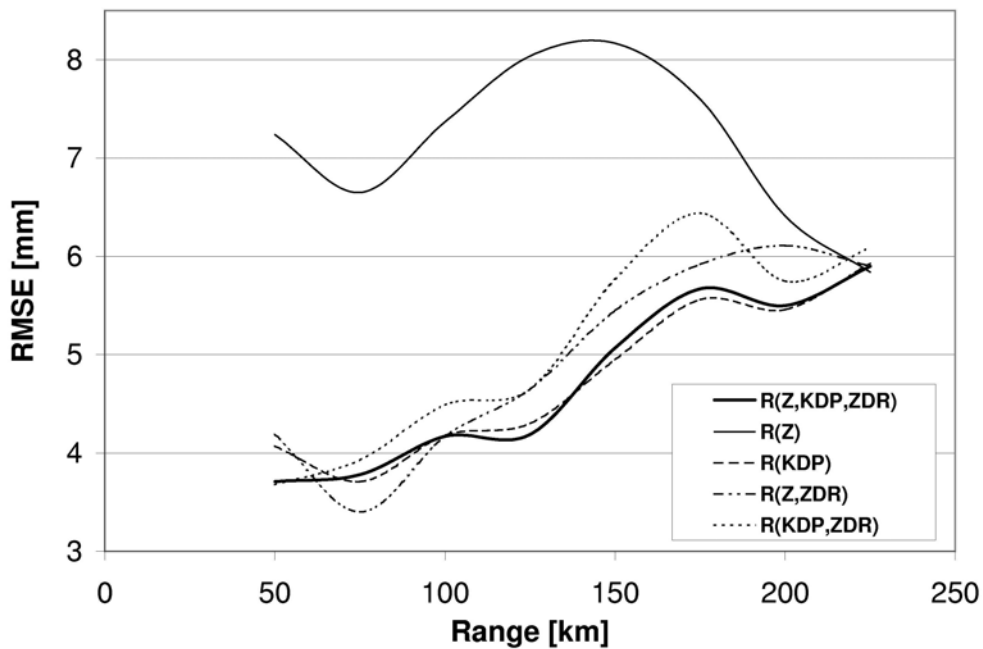
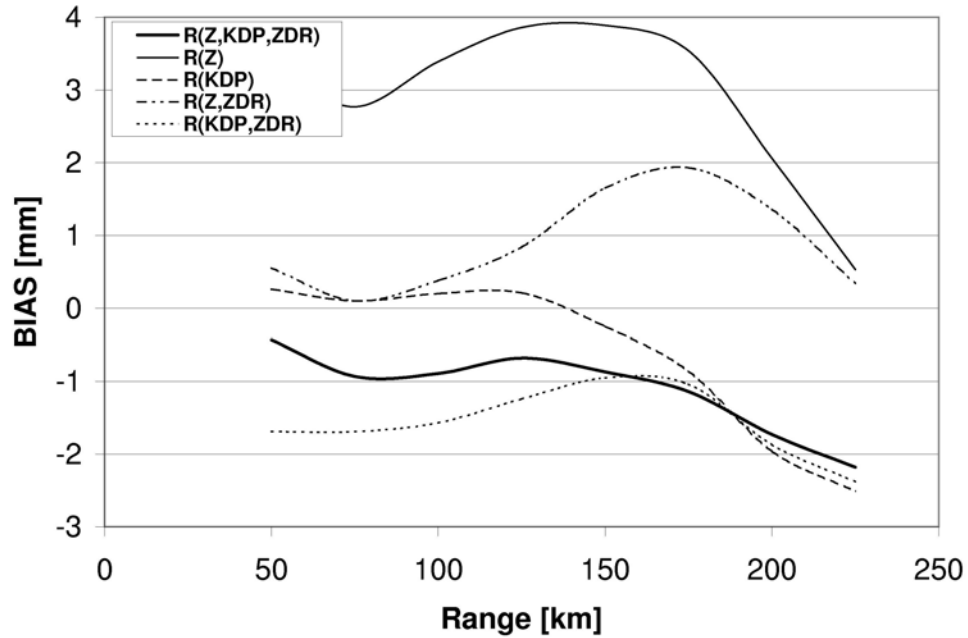


Fig. 15. Mean biases (a) and RMS errors (b) of the radar estimates as functions of range. Only warm season events are included in the statistics (54 hours of observations).

range dependencies of Φ_{DP} and spurious negative / positive K_{DP} as a result (Ryzhkov and Zrnich 1998). This is an unavoidable deficiency of K_{DP} .

Third, the radial resolution of K_{DP} estimates is worse than that of Z and Z_{DR} . When combined with poor azimuthal resolution at large distances, this might cause problems for point estimations of rainfall from the K_{DP} -based algorithms. More frequent update of the differential phase data would be advantageous.

At the ranges beyond 200 km, all radar algorithms for rainfall estimation perform equally poorly due to overshooting, beam broadening, and loss of sensitivity.

Summarizing, we can conclude that the synthetic polarimetric algorithm is a preferred choice for rainfall measurements at large distances (up to 200 km) if there is no apparent bright band contamination. We have to switch to the $R(K_{DP})$ relation at the distances where such contamination is pronounced. This is a common situation for cold season stratiform rain at the distances between 130 and 200 km from the radar. Therefore, it is necessary to detect bright band and delineate rain and snow prior to rain quantification. This can be done using our polarimetric classification algorithm.

An example of such classification for the winter storm on 4 December 2002 is shown in Fig. 16. This storm was associated with the passage of a cold front accompanied by the transition from rain to freezing rain and snow in the Oklahoma City metropolitan area. During this event, the melting layer was slowly subsiding with much lower height of the bright band in the cold air pool N – NW from the radar. This feature is manifested by the pronounced asymmetry of the “rain” area with respect to the radar location. Radar reflectivity, differential reflectivity, and cross-correlation coefficient give clear indication of the bright band in the northern sector. The bright band signature in the Z field is associated with increase of Z_{DR} and drop in ρ_{hv} in that direction. More precise determination of the bright band location was possible from the ρ_{hv} data at the elevation of 1.5°. At 0302 Z (12/04/02), rain was recognized up to the distances 50 – 60 km at the lowest elevation scan NW from the radar. At the same time, surface temperature fell below zero and freezing rain was reported on the ground. This freezing rain caused significant damage in the Oklahoma City metropolitan area.

If the conventional rainfall estimation algorithm is applied everywhere for the radar data at the lowest scan for this storm, the overestimation due to bright band contamination in the northern sector is inevitable. This is indeed the case as Fig. 17 demonstrates. The precipitation field obtained from the combination of data collected by several WSR-88D radars exhibit unrealistically high rain accumulations in the area of the bright band contamination for the KTLX radar. Another notable feature of the precipitation field in Fig. 18 relates to sharp discontinuities marking the boundaries of coverage areas for different radars. This is clear indication of radar calibration problems and it emphasizes the benefits of the polarimetric approach that is much less susceptible to miscalibration of radar reflectivity.

An example in Fig. 18 is a convincing proof that the use of the $R(K_{DP})$ algorithm in the regions of severe bright band contamination has indisputable advantage. Two-days rain accumulations computed from the $R(K_{DP})$ relation are in much better agreement with Mesonet gages in the SW sector of the KOUN radar coverage area than the estimates obtained from the conventional NEXRAD algorithm.

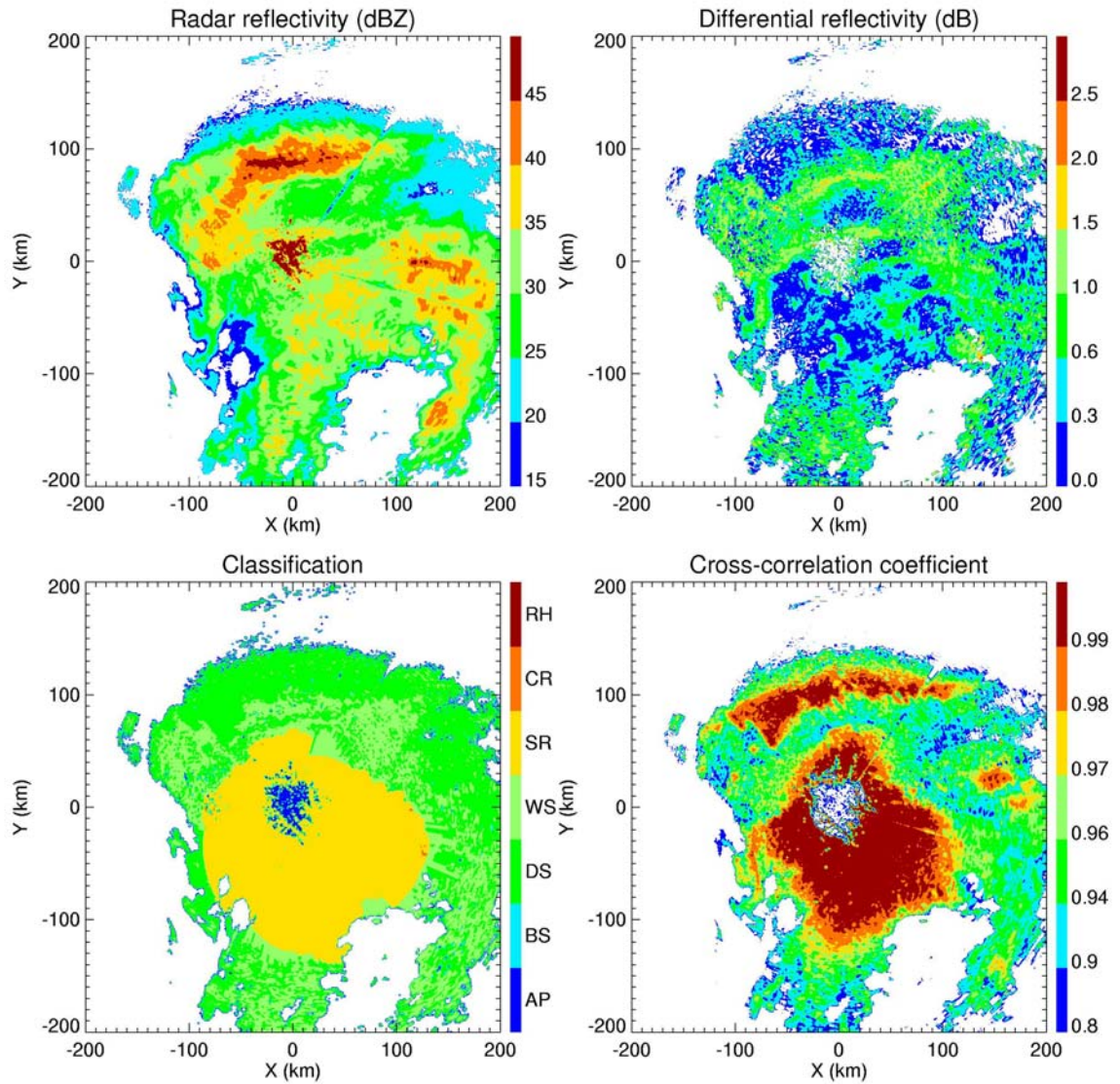


Fig. 16. Composite plot of Z , Z_{DR} , ρ_{hv} , and results of classification at $EI = 0.5^\circ$ for winter storm on 4 December 2002 (0302 Z). AP stands for ground clutter, BS – for biological scatterers, DS – for dry snow, WS – for wet snow, SR – for stratiform rain, CR – for convective rain, and RH – for rain / hail mixture.

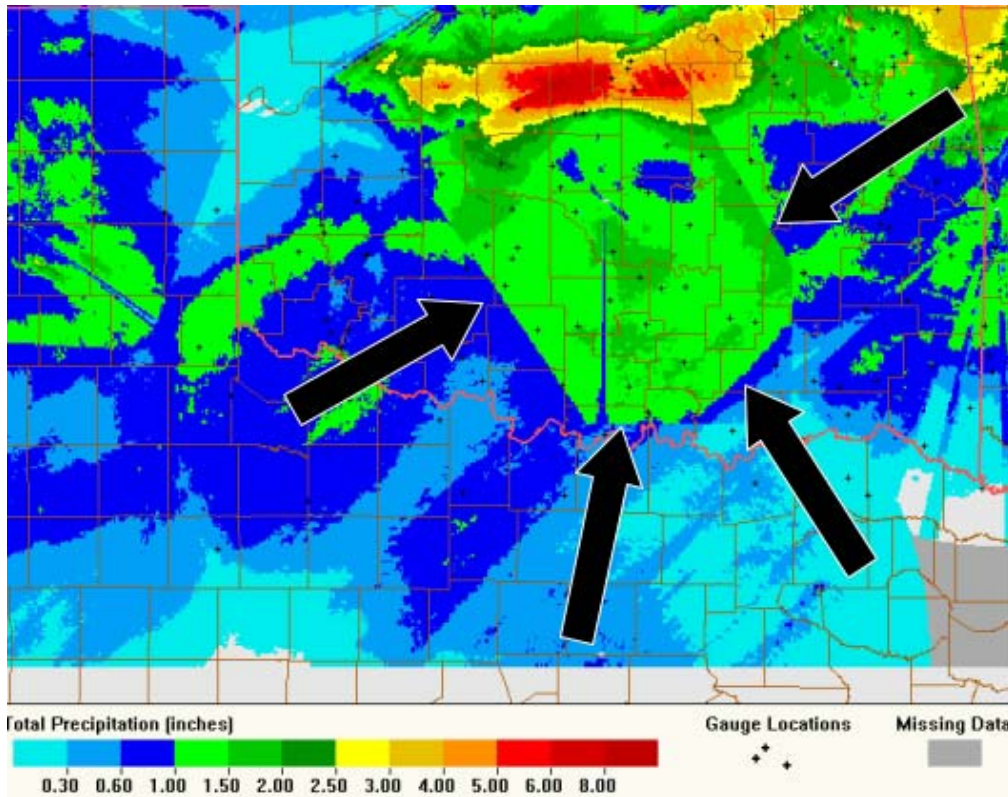


Fig. 17. Precipitation mosaic from different WSR-88D radars on 3 – 4 December 2002 (courtesy of J.J. Gourley).

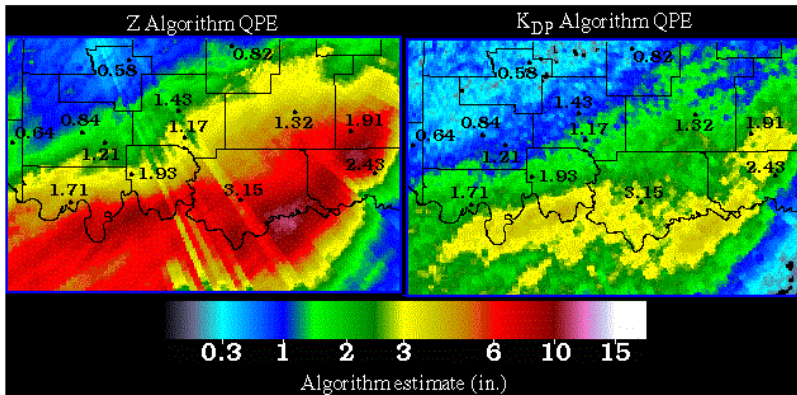
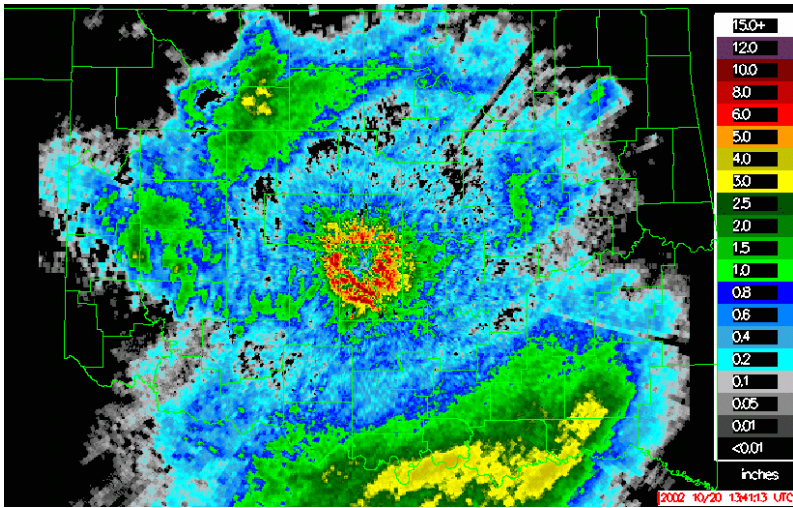
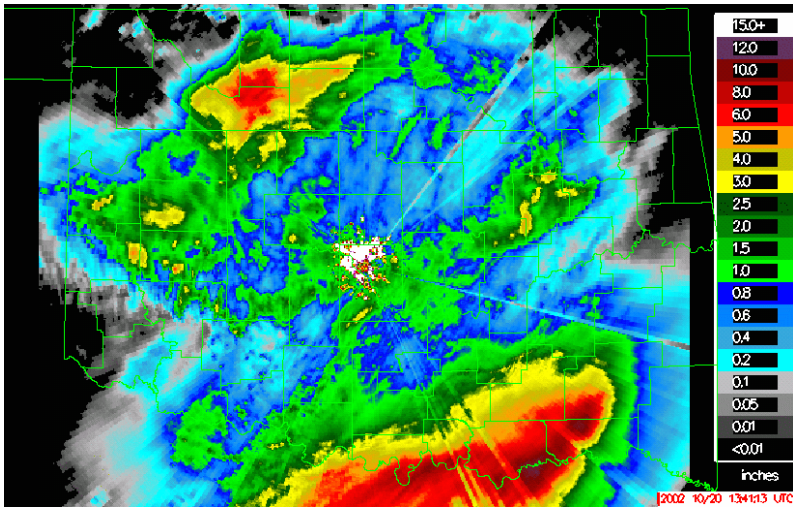


Fig.18. Two days (48 hr) rain total for the 18 – 20 October 2002 rain event from the (a) R(Z) and (b) R(K_{DP}) algorithm with (c) gage accumulations superimposed in the bright band accumulation area in SE sector.

6. Conclusions

- Rain measurement capability of the polarimetric prototype of the WSR-88D radar with simultaneous transmission and short dwell time has been tested using large dataset.
- At the distances less than 125 km from the radar, most polarimetric algorithms clearly outperform the conventional one, although the degree of improvement might be noticeably “weighted” by few spring heavy rain events.
- The “synthetic” polarimetric algorithm $R(Z, K_{DP}, Z_{DR})$ shows the best performance. This algorithm is most robust with respect to radar calibration errors, DSD variations, uncertainty of the raindrop shapes, and possible presence of hail.
- Most significant improvement is achieved in areal rainfall estimation and in measurements of heavy precipitation (often mixed with hail).
- These advantages have important practical implications for (a) river flash flooding forecast and management that require reliable measurement of areal rain accumulations regardless of rain intensity and (b) urban flash flooding forecast that requires accurate estimation of heavy rain with high spatial resolution.
- Polarimetric algorithms outperform the conventional relation $R(Z)$ up to the distances of 200 km from the radar (in terms of RMSE).
- For “cold” season cases dominated by stratiform rain with low bright band, the $R(K_{DP})$ algorithm is the best at ranges where bright band is intercepted by the beam at lowest elevation.
- For “warm” season cases dominated by convective rain, the $R(Z, K_{DP}, Z_{DR})$ algorithm is the best at all ranges (in terms of RMSE). However, all K_{DP} -based rain estimates tend to underestimate rain at long distances. This might be attributed to (a) possible Φ_{DP} aliasing and (b) negative K_{DP} caused by non-uniform beam filling.
- Delineation between rain and snow (bright band detection) is necessary to select an optimal algorithm
- Beyond 200 km, all algorithms perform poorly due to beam overshooting precipitation, beam broadening, and loss of sensitivity.

References

- Andsager, K., K.V. Beard, and N.F. Laird, 1999: Laboratory measurements of axis ratios for large drops. *J. Atmos. Sci.*, **56**, 2673 – 2683.
- Beard K.V, and Chuang C. 1987. A new model for the equilibrium shape of raindrops. *J. Atmos. Sci.*, **44**: 1509 – 1524.
- Brandes, E.A., A.V. Ryzhkov, D.S. Zrnic, 2001: An evaluation of radar rainfall estimates from specific differential phase. *J. Atmos. Oceanic Tech.*, **18**, 363 - 375.
- Brandes, E.A., G. Zhang, and J. Vivekanandan, 2002: Experiments in rainfall estimation with a polarimetric radar in a subtropical environment. *J. Appl. Meteor.* **41**, 674-685.
- Brandes, E.A., G. Zhang, and J. Vivekanandan, 2003a: An evaluation of a drop distribution based polarimetric radar rainfall estimator. *J. Appl. Meteor.* **42**, 652 - 660.
- Brandes, E.A., G. Zhang, and J. Vivekanandan, 2003b: Drop-size distribution retrieval with polarimetric radar: model and application. *J. Appl. Meteor.*, submitted.
- Brandes, E.A., G. Zhang, and J. Vivekanandan, 2003c: Comparison of polarimetric radar drop size distribution retrieval algorithms. *J. Atmos. Oceanic Technol*, submitted.
- Bringi, V.N., and V. Chandrasekar, 2001: *Polarimetric Doppler Weather Radar. Principles and Applications*, Cambridge University Press, 636 p.
- Bringi, V.N., G. Huang, V. Chandrasekar, and E. Gorgucci, 2002a: A methodology for estimating the parameters of a Gamma raindrop size distribution model from polarimetric radar data: application to a squall-line event from the TRMM/Brazil campaign. *J. Atmos. Oceanic Technol.* **19**, 633 – 645.
- Bringi, V.N, T. Tang, and V. Chandrasekar, 2002b: Evaluation of a new polarimetrically-tuned Z-R relation. *Proc. ERAD*, 217 – 221.
- Bringi, V.N., V. Chandrasekar, J. Hubbert, E. Gorgucci, W. Randeu, and M. Scoenhuber, 2003: Raindrop size distribution in different climate regimes from disdrometer and dual-polarized radar analysis. *J. Atmos. Sci.*, **60**, 354 – 365.
- Doviak, R.J., V. Bringi, A.V. Ryzhkov, A. Zahrai, D.S. Zrnic, 2000: Considerations for polarimetric upgrades to operational WSR-88D radars. *Journal of Atmospheric and Oceanic Technology*, **17**, 257 - 278.
- Fulton, R., A. Ryzhkov, and D. Zrnic, 1999: Areal rainfall estimation using conventional and polarimetric radar methods. Preprints, *29th International Conference on Radar Meteorology*, Montreal, Canada, Amer. Meteor. Soc., 293-296.
- Goddard, J., J. Tan, and M. Thurai, 1994: Technique for calibration of meteorological radars using differential phase. *Electronic Letters*, **30**, 166 – 167.
- Goddard, J., K. Morgan, A. Illingworth, and H. Sauvageot, 1995: Dual-wavelength polarization measurements in precipitation using the CAMRA and Rabelias radars. Preprints, *27th Conf. on Radar Meteorology*, Vail, CO, Amer. Met. Soc., 196 – 198.
- Godfrey, C., 2002: A comparison of rainfall rates measured by a 2D-video disdrometer and a vibrating wire rain gauge. M.S. thesis, University of Oklahoma.
- Gorgucci, E., G. Scarchilli, and V. Chandrasekar, 1999: A procedure to calibrate multiparameter weather radar using properties of the rain medium, *IEEE Trans. Geosci. Remote Sensing*, **37**, 269 – 276.

- Gorgucci, E., G. Scarchilli, V. Chandrasekar, and V. Bringi, 2000: Measurement of mean raindrop shape from polarimetric radar observations, *J. Atmos. Sci.*, **57**, 3406 – 3413.
- Gourley, J., B. Kaney, and R. Maddox, 2003: Evaluating the calibrations of radars: a software approach. Preprints, *31st International Conference on Radar Meteorology*, Seattle, 459 – 462.
- Illingworth, A., and T. Blackman, 2002: The need to represent raindrop size spectra as normalized Gamma distributions for the interpretation of polarization radar observations. *J. Appl. Meteorol.*, **41**, 286 - 297
- Matrosov, S.Y., K.A. Clark, B.E. Martner, A. Tokay, 2002: Measurements of rainfall with polarimetric X-band radar. *J. Appl. Meteor.*, **41**, 941 – 952.
- May, P., T.D. Keenan, D. Zrnica, L. Carey, and S. Rutledge, 1999: Polarimetric radar measurements of tropical rain at 5-cm wavelength. *J. Appl. Meteor.*, **38**, 750-765.
- Melnikov, V., D. Zrnica, R. Doviak, and J. Carter, 2003: Calibration and performance analysis of NSSL's polarimetric WSR-88D. NSSL's report, 15 May, 77 pp.
- Pruppacher, H., and K. Beard, 1970: A wind tunnel investigation of the internal circulation and shape of water drops falling at terminal velocity in air. *Quart. J. Roy. Meteor. Soc.*, **96**, 247 – 256.
- Ryzhkov, A., and D. Zrnica, 1995a: Precipitation and attenuation measurements at a 10 cm wavelength. *J. Appl. Meteor.*, **34**, 2121-2134.
- Ryzhkov, A., and D. Zrnica, 1995b: Comparison of dual-polarization radar estimators of rain. *Journal of the Atmospheric and Oceanic Technology*, **12**, 249-256.
- Ryzhkov, A., and D. Zrnica, 1996: Assessment of rainfall measurement that uses specific differential phase. *J. Appl. Meteor.*, **35**, 2080-2090.
- Ryzhkov, A., and D. Zrnica, 1998: Beamwidth effects on the differential phase measurements of rain. *J. Atmos. Oceanic Technol.*, **15**, 624-634.
- Ryzhkov, A.V., D.S. Zrnica, and R. Fulton, 2000: Areal rainfall estimates using differential phase. *Journal of Applied Meteorology*, **39**, 263 - 268.
- Ryzhkov, A.V., T.J. Schuur, and D.S. Zrnica, 2001: Radar rainfall estimation using different polarimetric algorithms. Preprints, *30th International Conference on Radar Meteorology*, Munich, Germany, 641 - 643.
- Ryzhkov, A.V., T.J. Schuur, D.S. Zrnica, 2002: Testing a polarimetric rainfall algorithm and comparison with a dense network of rain gauges. Submitted to the special issue of *Hydrological Resources* on Hydrological Applications of Weather Radar
- Ryzhkov, A.V., and T.J. Schuur, 2003: Effective shape of raindrops. Polarimetric radar perspective. *Proc. IGARSS-2003*, Toulouse, France, CDROM.
- Schuur, T.J., A.V. Ryzhkov, D.S. Zrnica, and M. Schoenhuber, 2001a: Drop size distributions measured by a 2D video disdrometer: comparison with dual-polarization data. *J. Appl. Meteor.*, **40**, 1019-1034.
- Schuur T.J., A.V. Ryzhkov, and D.S. Zrnica, 2001b: A statistical analysis of 2D-video-disdrometer data: impact on polarimetric rainfall estimation. Preprints, *30th International Conference on Radar Meteorology*, Munich, Germany, 646 – 648.
- Seo D.J, J. Breidenbach, R. Fulton, D. Miller, T. O'Bannon, 2000: Real-time adjustment of range-dependent biases in WSR-88D rainfall estimates due to nonuniform vertical profile of reflectivity. *J. Hydrometeorology*, **1**, 222 – 240.

- Smith, J.A., D.J. Seo, M.L. Baeck, and M.D. Hudlow, 1996: An intercomparison study of NEXRAD precipitation estimates. *Water Resour. Res.*, **32**, 2035 – 2045.
- Vivekanandan, J., G. Zhang, S. Ellis, D. Rajopadhyaya, and S. Avery, 2003: Radar reflectivity calibration using differential propagation phase measurements. *Radio Science* (accepted).
- Zrnich, D., and A. Ryzhkov, 1996: Advantages of rain measurements using specific differential phase. *J. Atmos. Oceanic Technol.*, **13**, 454-464.

APPENDIX A

Effective raindrop shape and its variability

Interpretation of polarimetric radar measurements in rain depends on the mean raindrop shape – size relation. The shapes of raindrops have been studied both theoretically and experimentally using laboratory measurements and 2D imaging probe data. In a steady air flow, raindrops have equilibrium shapes as described by Beard and Chuang (1987)

$$a/b = 1.0048 + 0.00057 D - 0.02628 D^2 + 0.003682 D^3 - 0.0001677 D^4 \quad (A1)$$

where a/b is the axis ratio of raindrop and D is its equivolume diameter expressed in mm. The actual shapes of raindrops in unsteady flow are expected to differ from the equilibrium shapes because of drop oscillations. Oscillating drops appear to be more spherical on average than the drops with equilibrium shapes as shown by Andsager et al. (1999) in laboratory studies. They found out that the shape of raindrops in the size range between 1.1 and 4.4 mm is better described by the following formula

$$a/b = 1.012 - 0.01445 D - 0.01028 D^2 \quad (A2)$$

Bringi et al (2003) suggested using Eq (A2) for drops with sizes smaller than 4.4 mm and Eq (A1) for larger sizes. Another shape – diameter relation that combines the observations of different authors was recently proposed by Brandes et al. (2002)

$$a/b = 0.9951 + 0.02510 D - 0.03644 D^2 + 0.005030 D^3 - 0.0002492 D^4 \quad (A3)$$

The dependencies of the raindrop axis ratio on its equivolume diameter for equilibrium shapes defined by (A1), “oscillating” raindrop shapes specified by Bringi et al.(2003), and the ones defined by (A3) are shown in Fig. A1.

Given the scarcity and uncertainty of the direct measurements of drop shapes, a polarimetric radar method for raindrop shape estimation suggested by Gorgucci et al. (2000) emerges as a very attractive alternative to direct in situ observations. The radar method, however, assumes linear dependence of a/b on D

$$a/b = (1.0 + 0.05\beta) - \beta D \quad (A4)$$

which is characterized by a slope β (mm^{-1}) (see Fig A1). According to Gorgucci et al. (2000), the parameter β can be estimated from the measurements of reflectivity factor Z , differential reflectivity Z_{DR} , and specific differential phase K_{DP} as

$$\beta = 2.08 \cdot 10^{-0.0365 Z + 0.0965 Z_{DR}} K_{DP}^{0.380} \quad (A5)$$

where Z is expressed in dBZ, Z_{DR} – in dB, and K_{DP} – in deg/km. Formula (A5) was derived using computations of Z , Z_{DR} , and K_{DP} from simulated drop size distributions for

different β ranging between $0.02 - 0.10 \text{ mm}^{-1}$. No drop canting was taken into account by Gorgucci et al. (2000).

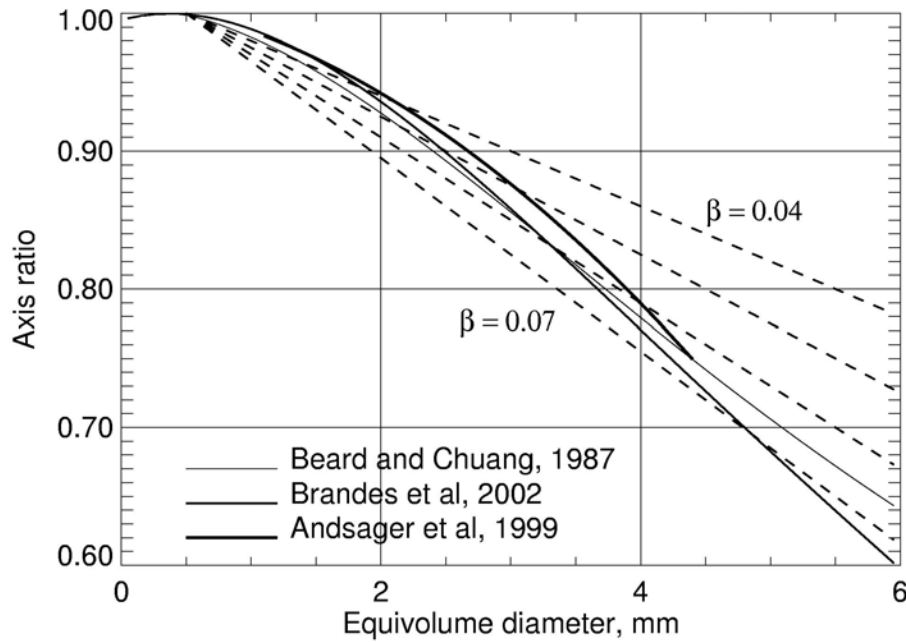


Fig. A1. Different dependencies of the raindrop axis ratio on the equivolume diameter.

Ryzhkov and Schuur (2003) suggested slightly different relation for estimating parameter β

$$\beta = 8.73 \cdot 10^{-0.0499 Z + 0.1366 Z_{DR}} K_{DP}^{0.519} \quad (\text{A6})$$

Eq (A6) was obtained using 17470 one-minute DSDs measured with the NSSL's 2D-video disdrometer (Schuur et al. 2001a). It was assumed also that the drops are canted with the mean canting angle equal to zero and the width σ of the canting angle distribution of 10° . It can be shown that canting of drops with $\sigma = 10^\circ$ is equivalent to average decrease in the "effective" slope β of about 10% if intrinsic β varies between 0.02 and 0.10 mm^{-1} .

We utilize (A6) for estimating prevailing slope β and its variability for several rain events using polarimetric radar observations during the JPOLE. The histograms of the parameter β have been examined from the radar data collected over the ARS Micronet. For every hour, data from 9 to 30 successive radar scans were examined within the ARS area. Individual $1 \times 1 \text{ km}$ pixels were counted in a histogram provided that a radar echo is strong enough to allow computation of β from (A6). In order to reduce statistical error in the β retrieval, we selected pixels for which $Z > 35 \text{ dBZ}$, $Z_{DR} > 0.2 \text{ dB}$, and $K_{DP} > 0.1 \text{ deg/km}$. This constraint eliminates data points with rain rates lower than $7 - 8 \text{ mm h}^{-1}$. We also applied a threshold 0.98 for the cross-correlation coefficient ρ_{hv} to avoid possible contamination of the β estimate by the presence of hail, because relations (A5) and (A6) are valid for rain only.

Three histograms for the cases of tropical, stratiform, and convective rain are plotted in Fig. A2. The “tropical” and “MCS” histograms represent the two hours of observations (out of 32 hours being analyzed) with extreme modal values of β . Modal β values for the remaining 30 hours are found between these extremes. Average modal β for 32 hours of observations is equal to 0.052 mm^{-1} with a standard deviation of 0.008 mm^{-1} . This average value is smaller than a commonly used slope of 0.062 mm^{-1} suggested by Pruppacher and Beard (1970) and slightly higher than the one (0.0475 mm^{-1}) that was reported by Bringi et al (2003) and obtained as a result of simulations based on direct DSD measurements for tropical rain.

For each individual rain event, the slope β apparently tends to decrease with increasing Z or rain rate, but doesn't exhibit any dependence on differential reflectivity Z_{DR} . It is interesting, however, that rain events with smaller net Z_{DR} are characterized by smaller slope β , i.e., more spherical shape of drops. For example, the three histograms in Fig. A2 are associated with the net Z_{DR} values of 0.3, 0.8, and 1.4 dB for tropical, stratiform, and MCS rain events respectively.

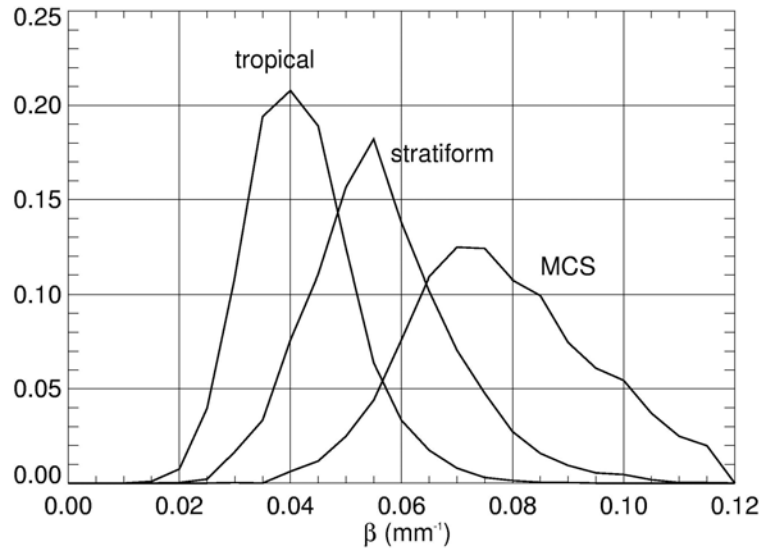


Fig. A2. Histograms of observed values of the estimate β for the cases of tropical rain (09/08/02, 19-20 UTC), stratiform rain (10/18/02, 18-19 UTC), and convective rain associated with MCS (09/19/02, 5 – 6 UTC).

More “spherical” shapes of drops are attributed to canting and oscillations induced by collisions and break-ups. This is consistent with lower β observed in the cores of heavy rain and especially in tropical type rain. In rain originated from hail aloft, ice cores inside raindrops likely suppress their oscillations but, at the same time, make effective drop shape different from the equilibrium one. This is consistent with significant variability of β observed in heavy rain contaminated with hail. Part of this variability is associated with possible biases of Z and Z_{DR} in rain mixed with hail.

Two important practical conclusions can be drawn from the analysis of raindrop shapes retrieved from the JPOLE dual-polarization data. First, raindrops appear to be more spherical than is predicted by equilibrium theory of Beard and Chuang (1997) likely

due to oscillations that are very common in the middle of rain cores. Second, the raindrop axis ratio can vary quite noticeably for a given raindrop equivolume diameter. Variations of mean raindrop shape have impact on a radar calibration methodology based on the consistency between the three polarimetric variables (Z , Z_{DR} , and K_{DP}), polarimetric DSD retrieval, and rainfall measurements. Polarimetric rainfall algorithms based on the combined use of K_{DP} and Z_{DR} might be preferable because they are more immune to drop shape uncertainty (Ryzhkov and Zrnic 1995b, Schuur et al. 2001b).

Next we examine possible impact of drop shape variations on the accuracy of radar reflectivity calibration based on the consistency between Z , Z_{DR} , and K_{DP} . According to the consistency principle, radar reflectivity factor can be roughly estimated from Z_{DR} and K_{DP} using the following relation

$$Z = a + b \log(K_{DP}) + c Z_{DR} \quad , \quad (A9)$$

where Z is expressed in dBZ, Z_{DR} – in dB, and K_{DP} – in deg/km. The coefficients a , b , and c in (1) depend on a radar wavelength, the assumption about raindrop shape, and are relatively insensitive to the DSD variations. We have examined different consistency relations available in literature and derived our own ones based on the existing statistics of DSD measurements in central Oklahoma. Detailed description of the 2D video disdrometer data set can be found at <http://cimms.ou.edu/~schuur/disdrom/2DVD.html>. The coefficients a , b , and c for different consistency relations valid at S band are summarized in Table A1.

Table A1. Coefficients a , b , and c for different consistency relations at S band.

	a	b	c	<i>Assumptions</i>	<i>Source</i>
1	46.3	11.0	1.78	Measured DSD, equilibrium shape	NSSL
2	46.8	10.7	1.48	Measured DSD, Brandes' shape	NSSL
3	48.5	11.4	0.94	Measured DSD, Bringi's shape	NSSL
4	44.0	10.9	3.78	Measured DSD, linear ($\beta = 0.052$)	NSSL
5	41.9	10.4	2.70	Simulated DSD, equilibrium shape	Gorgucci et al (2000)
6	45.5	10.0	0.95	Simulated DSD, equilibrium shape	Vivekanandan (2003)
7	42.2	10.0	2.76	Constrained Gamma DSD, eq. shape	Vivekanandan (2003)
8	44.8	10.0	2.05	Constarined Gamma DSD, Brandes'	Vivekanandan (2003)

In Table A1, constrained Gamma DSD means simulated DSD of the Gamma form (1) with parameters Λ and μ related as (Brandes et al. 2003a)

$$\Lambda = 1.935 + 0.735 \mu + 0.0365 \mu^2 \quad (A10)$$

In order to assess limitations on the accuracy of Z calibration due to raindrop shape uncertainty and the use of different consistency relations, we performed the following test based on 17470 DSDs measured with the 2D-video disdrometer in Norman. We computed Z , Z_{DR} , K_{DP} from measured DSD with four different assumptions about the dependence of raindrop shape on equivolume diameter: equilibrium, Brandes', Bringi's, and linear with the slope $\beta = 0.052 \text{ mm}^{-1}$. Then values of “estimated”

reflectivities Z_{est} were calculated from Z_{DR} and K_{DP} using all 8 consistency relations with the coefficients listed in Table A1. Average values of $Z_{\text{est}} - Z$ in the 20 – 50 dBZ range are represented in Table A2 for 8 algorithms and 3 most realistic assumptions about raindrop shape.

Table A2. Average errors in Z retrieval from different consistency relations and different assumptions about raindrop shape. The errors are expressed in dB.

	Equilibrium	Brandes'	Bringi's
1	0.14	-0.86	-0.96
2	0.88	-0.08	-0.17
3	1.11	0.12	0.07
4	-0.54	-1.64	-1.87
5	-2.67	-3.67	-3.83
6	0.26	-0.61	-0.66
7	-1.71	-2.68	-2.84
8	0.37	-0.56	-0.68

As can be seen from Table A2, depending on raindrop shape, the results of Z calibration for any given consistency relation may vary approximately within 1 dB. The difference between Z estimates from different consistency formulas can be as high as almost 4 dB for any particular dependencies of the raindrop axis ratio on equivolume diameter. Relations 5 (Gorgucci et al. 2000) and 7 (Vivekanandan et al. 2003) are obvious outliers, at least for Oklahoma. Thus, one has to exercise caution utilizing the consistency relation for calibration of Z measured by a polarimetric radar. The choice of an optimal relation is quite subjective. We selected the relation 3 for calibration of radar reflectivity measured by the KOUN radar because (1) this relation is well matched with the statistics of measured DSD in central Oklahoma and (2) it yields smallest errors for raindrop shapes typical for “oscillating “ drops as defined by Brandes and Bringi. It follows from our estimates of the parameter β that raindrops in Oklahoma’s storms have shapes more consistent with “oscillating” model than with equilibrium model.

APPENDIX B.

Summary of individual hours of rainfall estimation.

Number	Date	Beginning time	Z bias	Zdr bias	Number of scans
1	06/13/02	16	-3.0	0.1	29
2	06/16/02	2	-2.0	0.1	29
3	-	3	-2.0	0.1	30
4	08/14/02	1	-1.2	0.0	29
5	-	2	-1.2	0.0	29
6	-	3	-1.2	0.0	29
7	09/08/02	18	-2.1	-0.2	29
8	-	19	-2.1	-0.2	29
9	-	20	-2.1	-0.2	29
10	09/09/02	16	-0.8	-0.2	29
11	09/14/02	7	-2.2	-0.2	29
12	-	8	-2.2	-0.2	29
13	09/19/02	4	-3.0	-0.1	28
14	-	5	-3.0	-0.1	22
15	10/08/02	17	2.7	-0.1	29
16	-	18	2.7	-0.1	29
17	-	19	2.7	-0.1	29
18	-	22	2.7	-0.1	29
19	10/09/02	1	3.1	-0.1	29
20	-	2	3.1	-0.1	29
21	-	13	3.1	-0.1	29
22	10/19/02	19	4.1	-0.1	20
23	-	21	4.1	-0.1	20
24	10/23/02	16	4.1	-0.1	19
25	10/24/02	15	3.45	0.1	29
26	-	16	3.45	0.1	28
27	-	19	3.45	0.1	29
28	-	20	3.45	0.1	29
29	10/27/02	13	3.24	-0.1	29
30	10/28/02	19	3.24	-0.1	27
31	12/03/02	22	-0.7	-0.1	29
32	12/04/02	1	-0.7	-0.1	29
33	04/19/03	11	-1.0	0.1	9
34	-	12	-1.0	0.1	9
35	04/23/03	22	-1.0	0.1	9
36	05/14/03	7	-1.0	0.2	9
37	-	8	-1.0	0.2	9
38	05/20/03	2	-1.0	0.2	10
39	-	3	-1.0	0.2	9
40	-	4	-1.0	0.2	9

41	06/05/03	10	1.0	0.2	9
42	-	11	1.0	0.2	10
43	-	12	1.0	0.2	9
44	-	14	1.0	0.2	9
45	06/06/03	3	2.2	0.2	10
46	-	4	2.2	0.2	10
47	-	5	2.2	0.2	9
48	06/12/03	2	3.0	0.2	9
49	06/13/03	11	3.0	0.2	9
50	-	12	3.0	0.2	10

Convective and stratiform precipitation associated with a squall line passing through central Oklahoma.

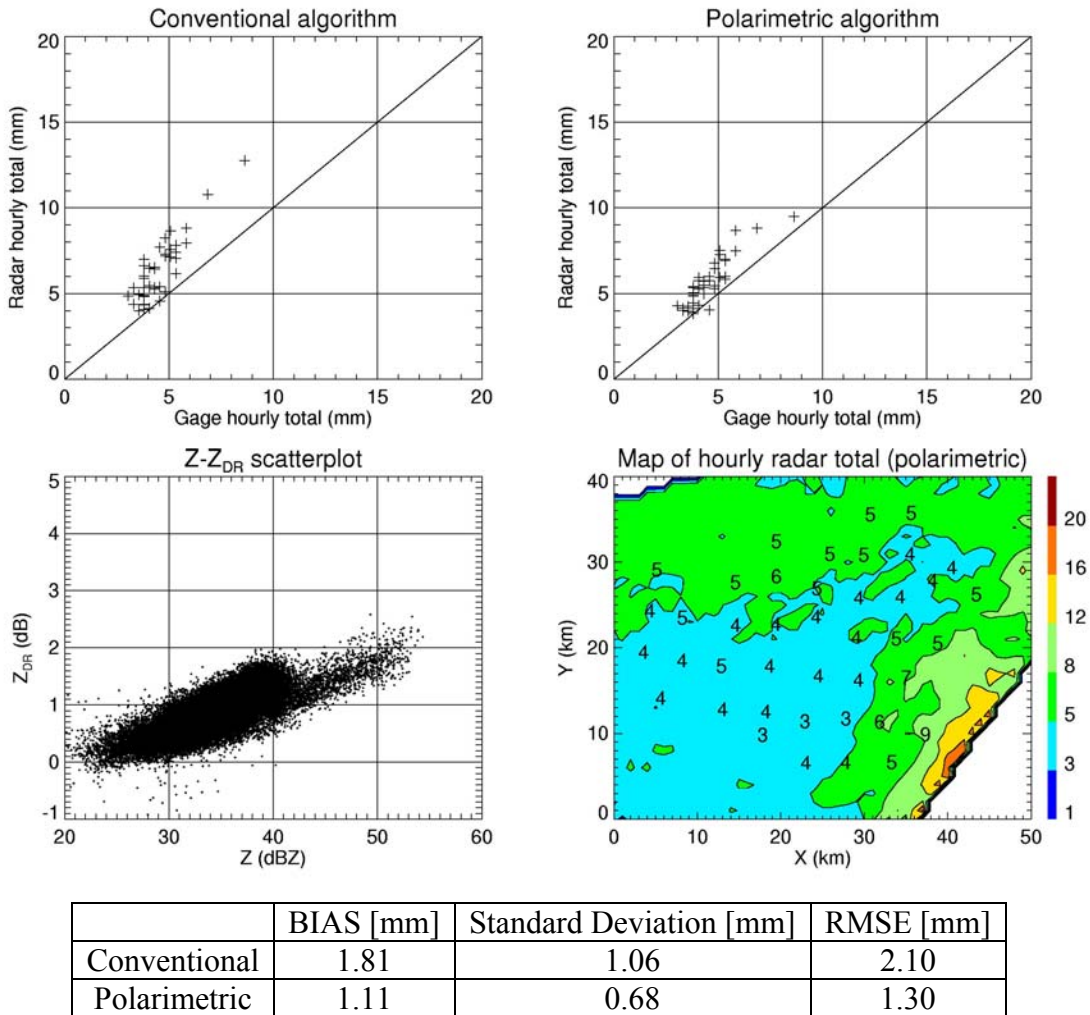
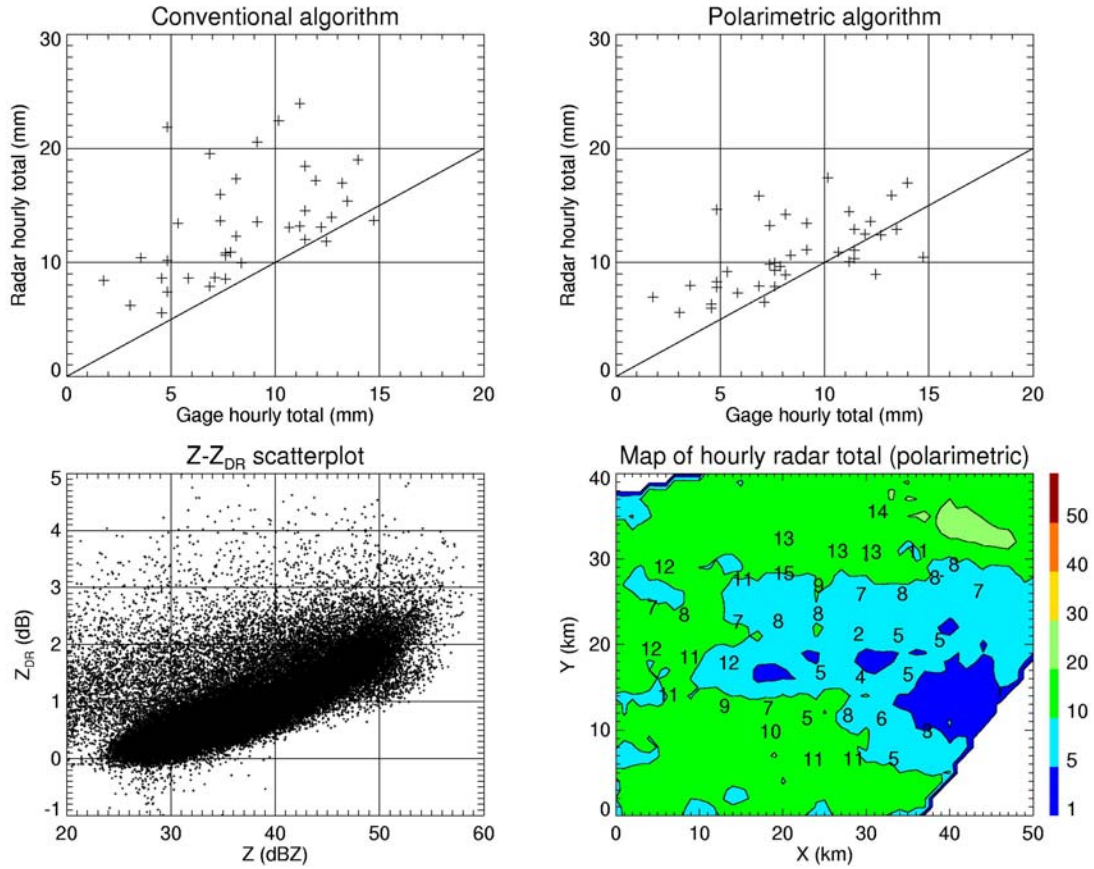


Fig. B1 – Hourly ARS gage totals versus estimates from the R(Z) and R(Z, K_{DP}, Z_{DR}) algorithm (top panels), a Z-Z_{DR} scattergram, and a map of the hourly radar rainfall totals with superimposed gage accumulations (bottom panels) for 13 June 2002 (16-17Z).

Squall line with several large convective cells exhibiting hail signatures.



	BIAS [mm]	Standard Deviation [mm]	RMSE [mm]
Conventional	4.75	4.10	6.27
Polarimetric	2.18	2.88	3.61

Fig. B2 – Hourly ARS gage totals versus estimates from the R(Z) and R(Z, K_{DP} , Z_{DR}) algorithm (top panels), a Z- Z_{DR} scattergram, and a map of the hourly radar rainfall totals with superimposed gage accumulations (bottom panels) for 16 June 2002 (2-3Z).

Trailing stratiform precipitation associated with the rear edge of a squall line passing through central Oklahoma.

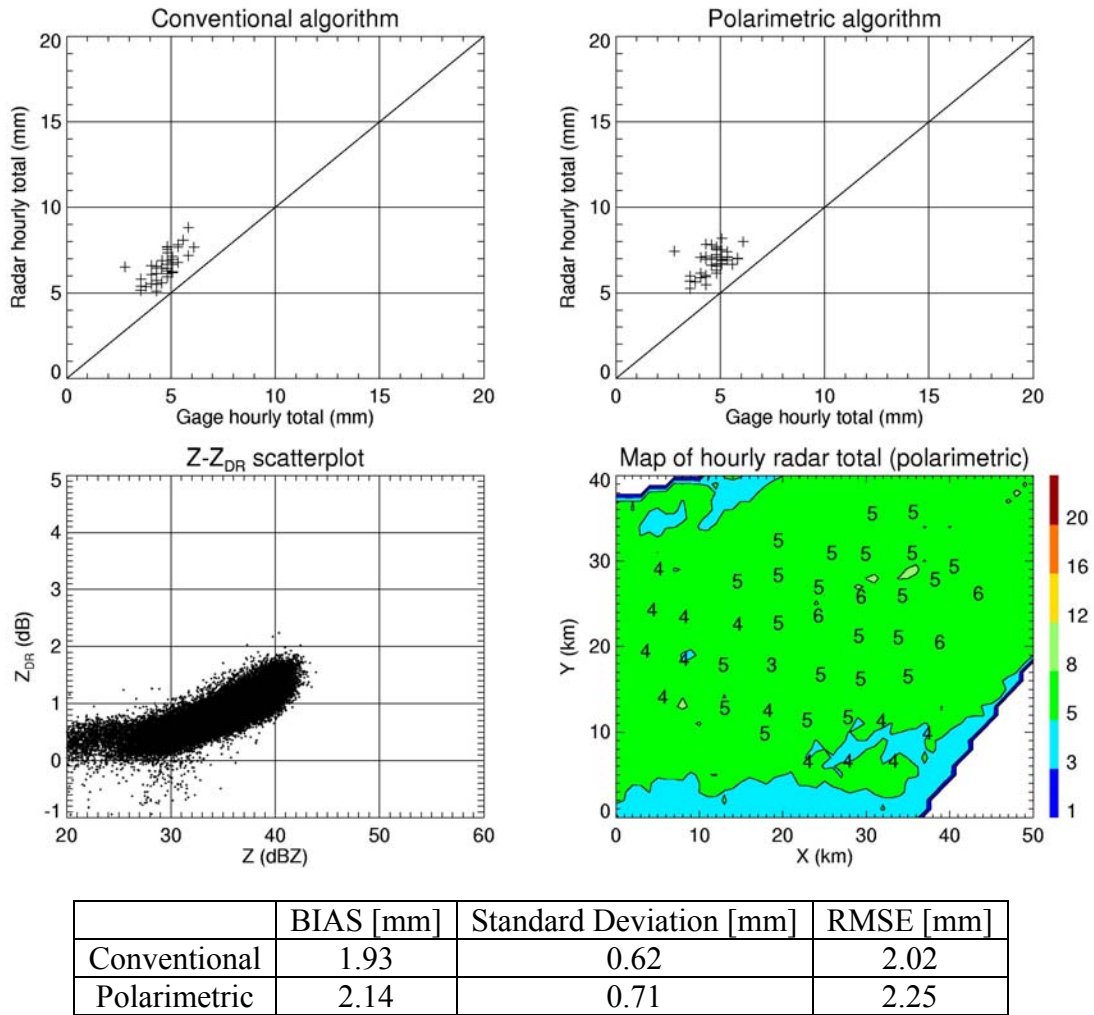


Fig. B3 – Hourly ARS gage totals versus estimates from the $R(Z)$ and $R(Z, K_{DP}, Z_{DR})$ algorithm (top panels), a $Z-Z_{DR}$ scattergram, and a map of the hourly radar rainfall totals with superimposed gage accumulations (bottom panels) for 16 June 2002 (3-4Z).

Scattered convective cells over central Oklahoma with signatures of embedded hail.

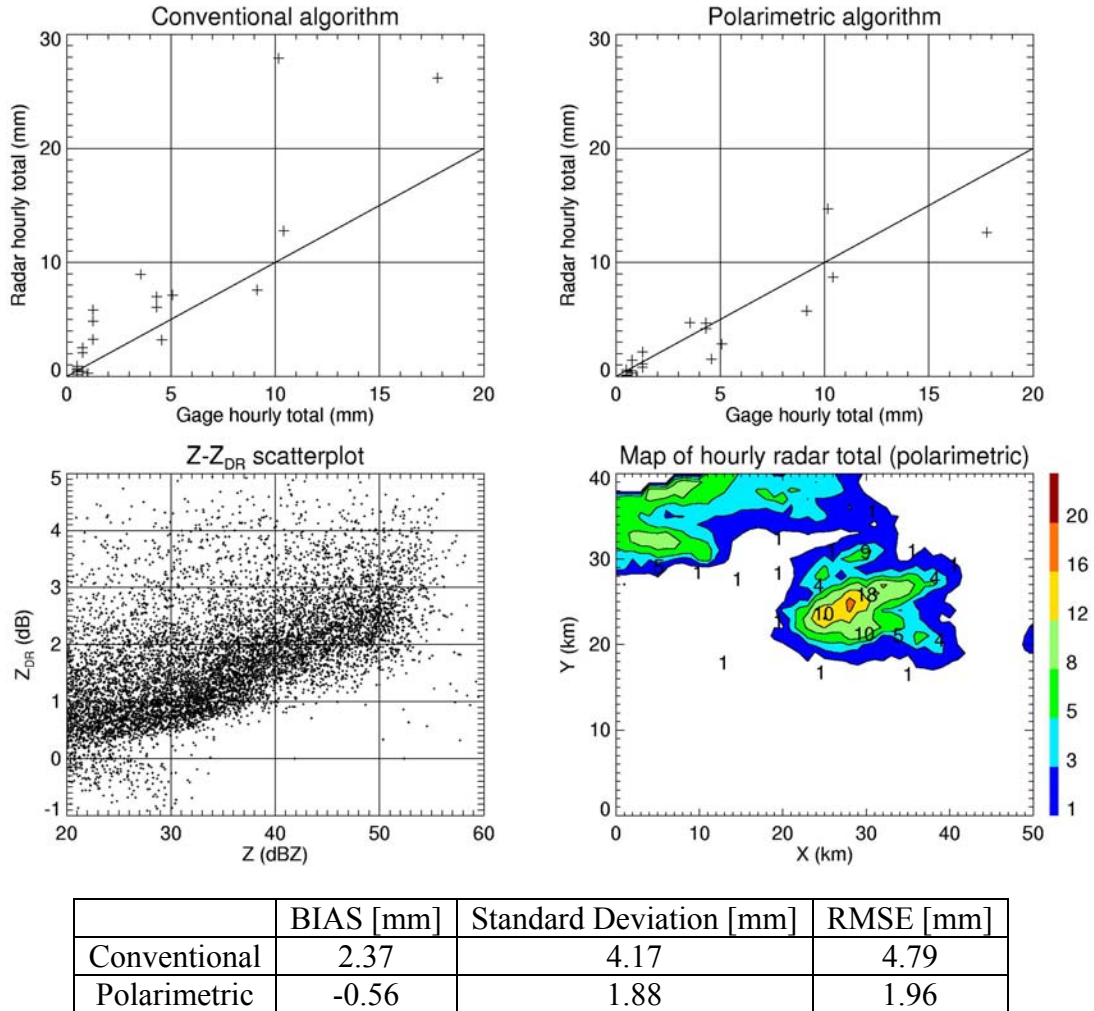


Fig. B4 – Hourly ARS gage totals versus estimates from the R(Z) and R(Z, K_{DP} , Z_{DR}) algorithm (top panels), a Z- Z_{DR} scattergram, and a map of the hourly radar rainfall totals with superimposed gage accumulations (bottom panels) for 14 August 2002 (1-2Z).

Scattered convective cells over central Oklahoma with signatures of embedded hail.

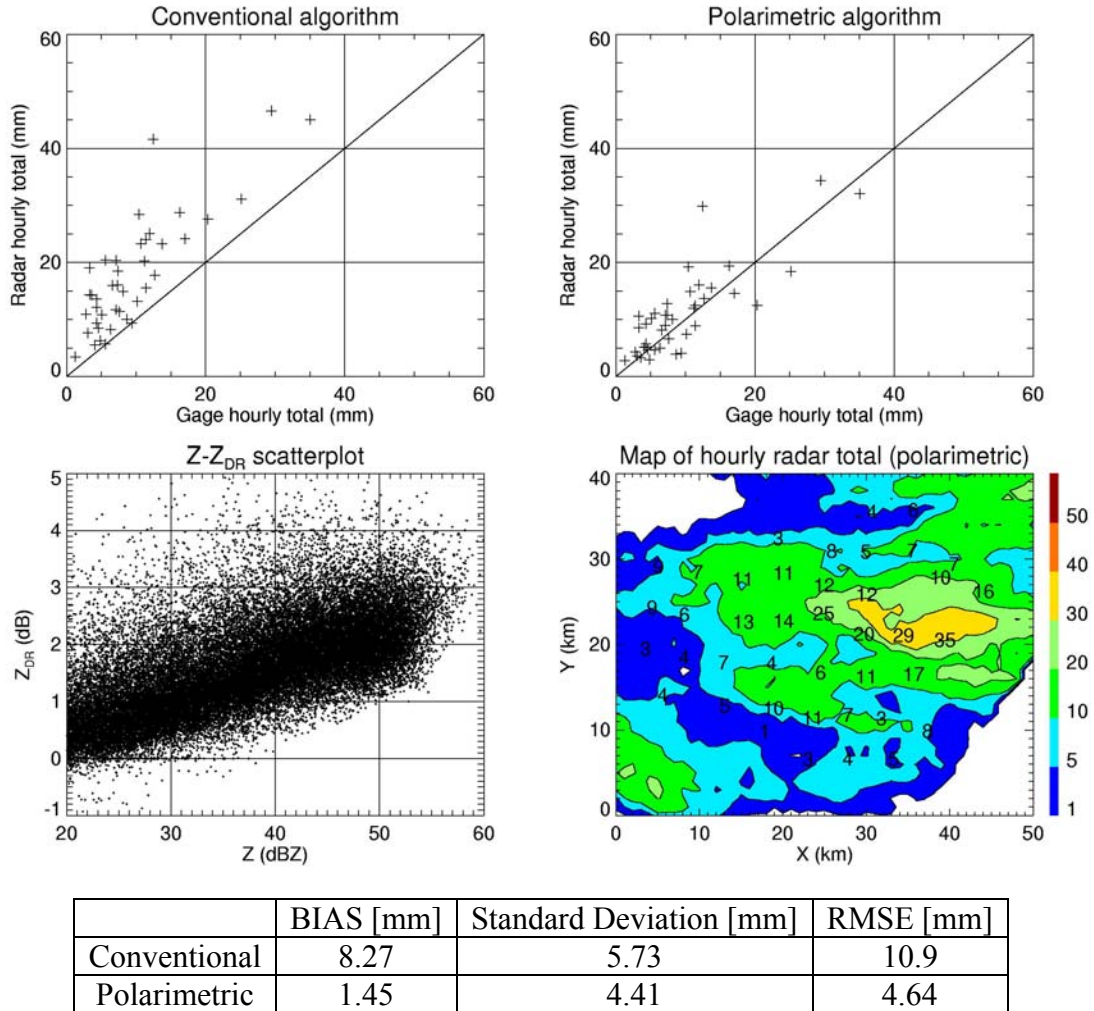


Fig. B5 – Hourly ARS gage totals versus estimates from the $R(Z)$ and $R(Z, K_{DP}, Z_{DR})$ algorithm (top panels), a $Z-Z_{DR}$ scattergram, and a map of the hourly radar rainfall totals with superimposed gage accumulations (bottom panels) for 14 August 2002 (2-3Z).

Scattered convective cells over central Oklahoma with signatures of embedded hail.

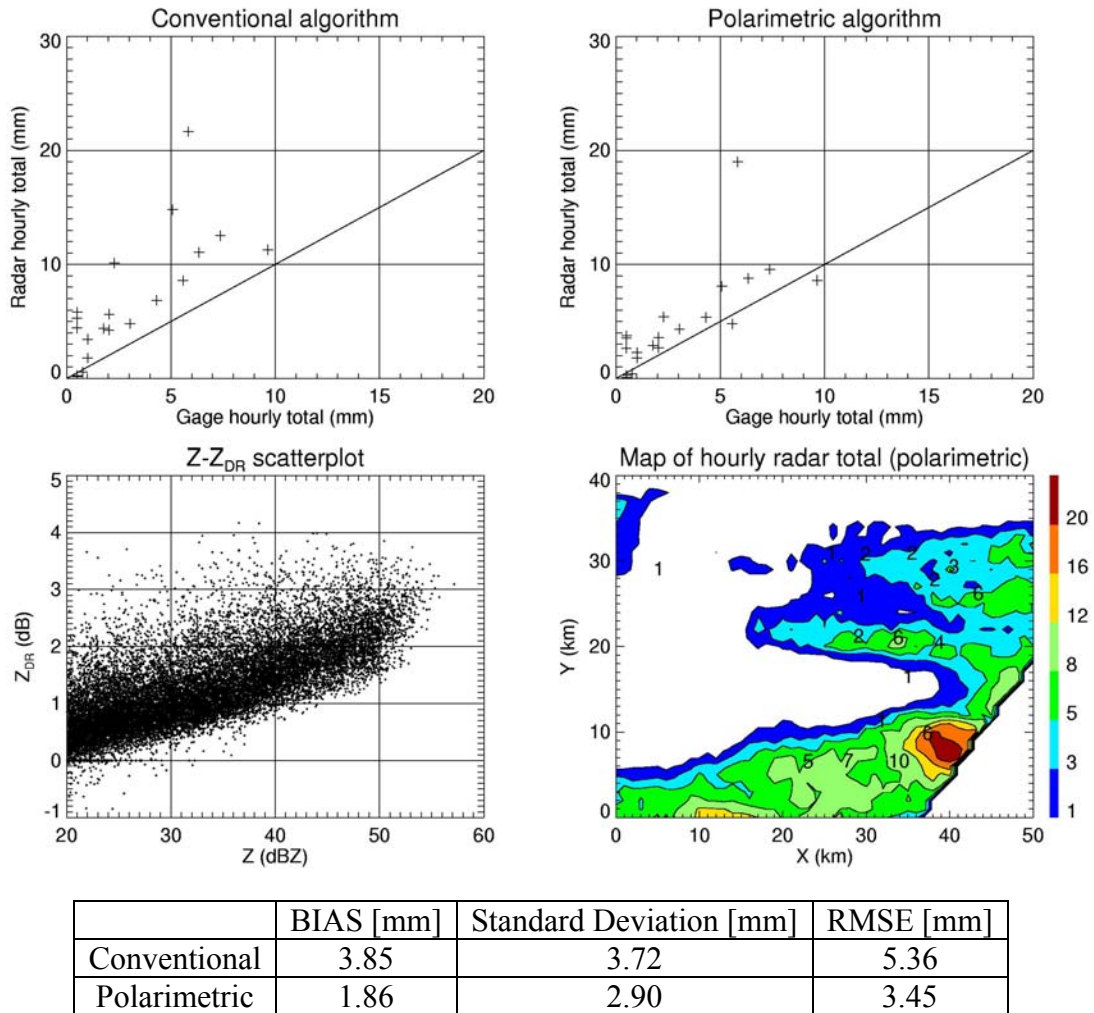


Fig. B6 – Hourly ARS gage totals versus estimates from the R(Z) and R(Z, K_{DP} , Z_{DR}) algorithm (top panels), a Z- Z_{DR} scattergram, and a map of the hourly radar rainfall totals with superimposed gage accumulations (bottom panels) for 14 August 2002 (3-4Z).

Stratiform precipitation in central Oklahoma associated with a cyclone centered over SE Texas/Gulf of Mexico.

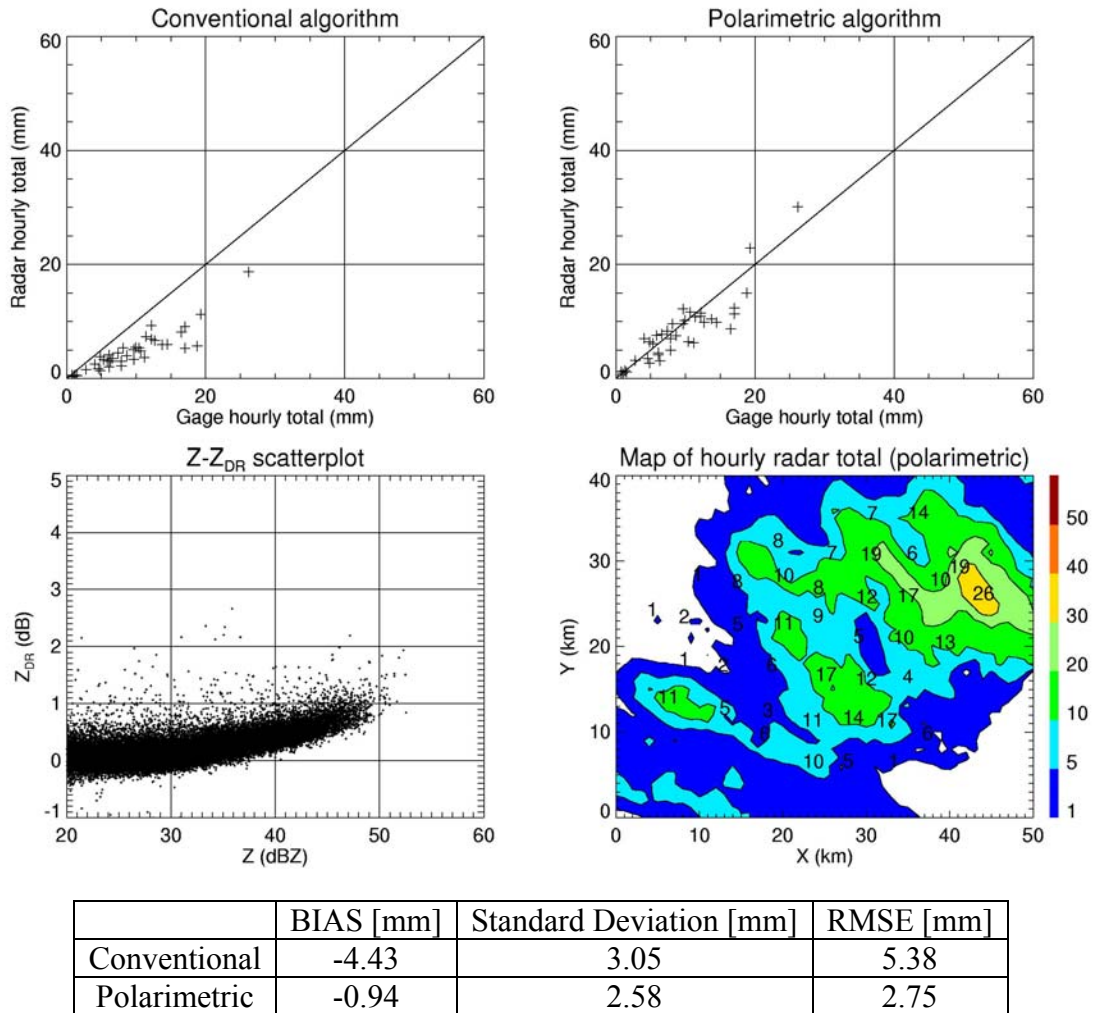


Fig. B7 – Hourly ARS gage totals versus estimates from the R(Z) and R(Z, K_{DP} , Z_{DR}) algorithm (top panels), a Z- Z_{DR} scattergram, and a map of the hourly radar rainfall totals with superimposed gage accumulations (bottom panels) for 8 September 2002 (18-19Z).

Stratiform precipitation in central Oklahoma associated with a cyclone centered over SE Texas/Gulf of Mexico.

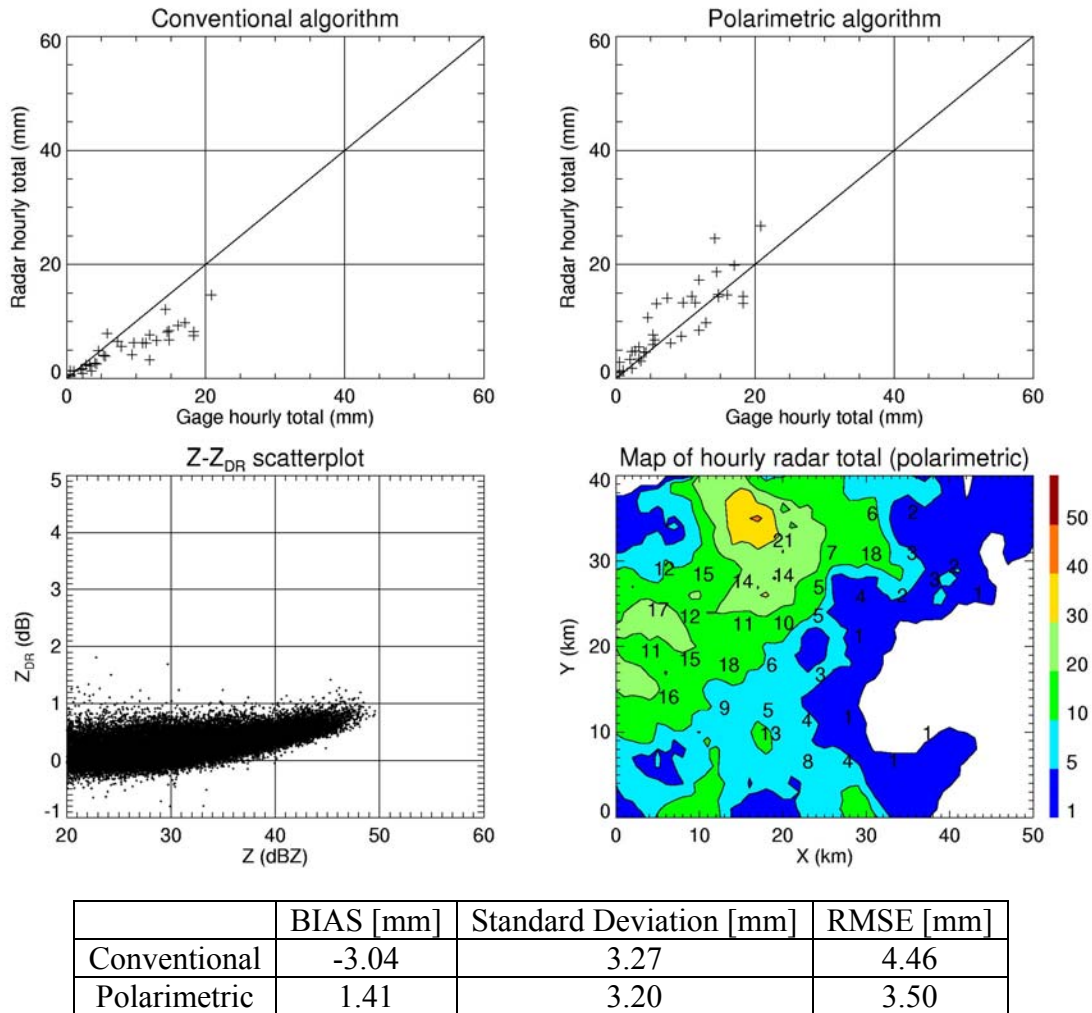


Fig. B8 – Hourly ARS gage totals versus estimates from the R(Z) and R(Z, K_{DP} , Z_{DR}) algorithm (top panels), a Z- Z_{DR} scattergram, and a map of the hourly radar rainfall totals with superimposed gage accumulations (bottom panels) for 8 September 2002 (19-20Z).

Stratiform precipitation in central Oklahoma associated with a cyclone centered over SE Texas/Gulf of Mexico.

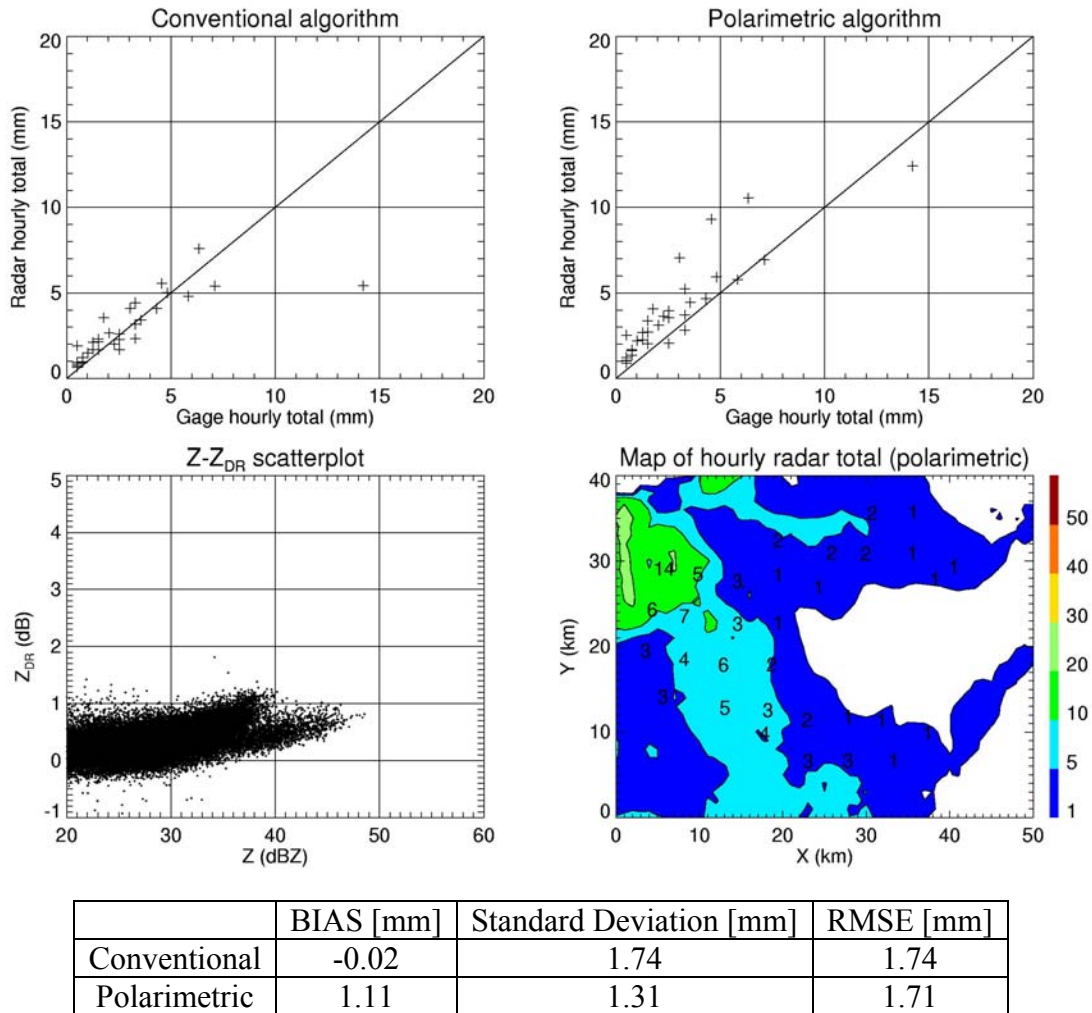


Fig. B9 – Hourly ARS gage totals versus estimates from the $R(Z)$ and $R(Z, K_{DP}, Z_{DR})$ algorithm (top panels), a $Z-Z_{DR}$ scattergram, and a map of the hourly radar rainfall totals with superimposed gage accumulations (bottom panels) for 8 September 2002 (20-21Z).

Stratiform precipitation in central Oklahoma associated with a cyclone centered over Southern Texas.

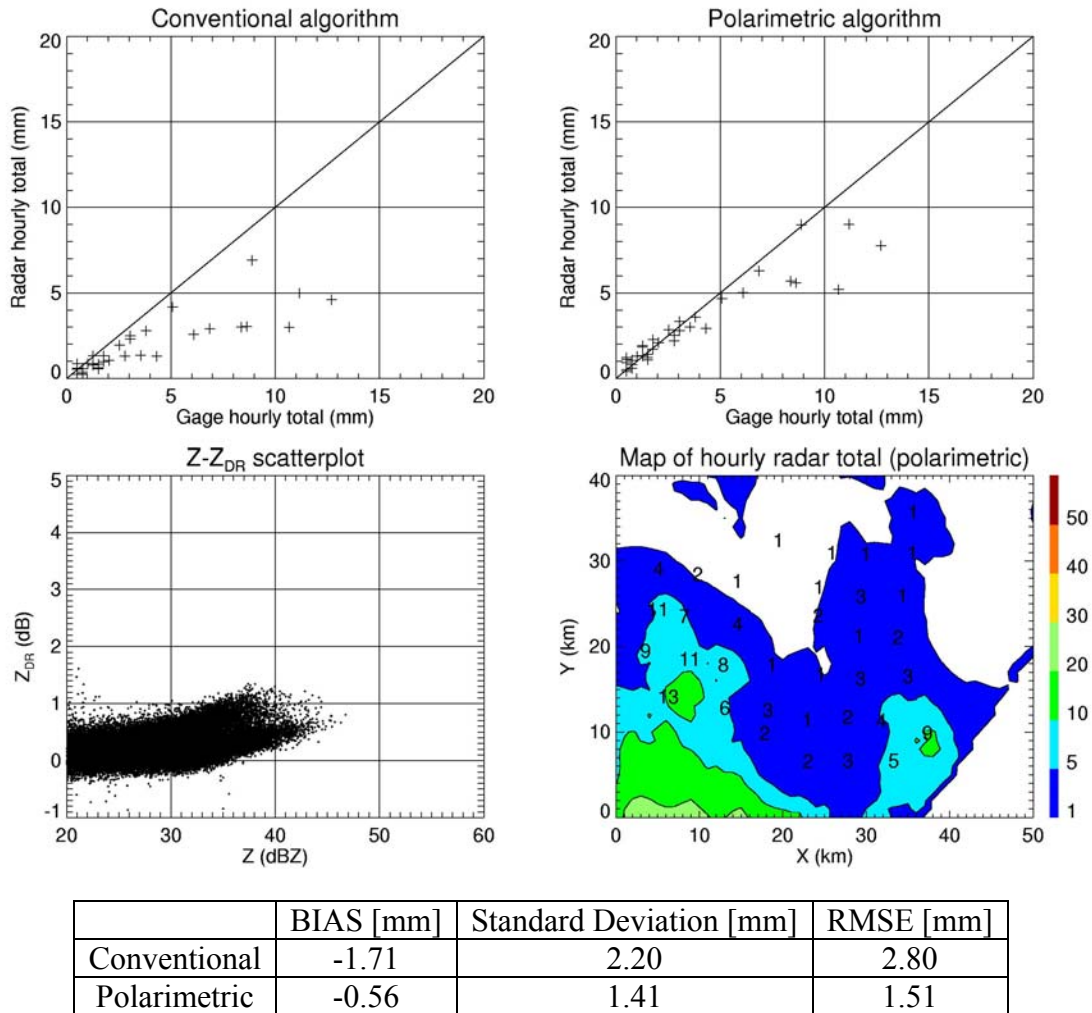
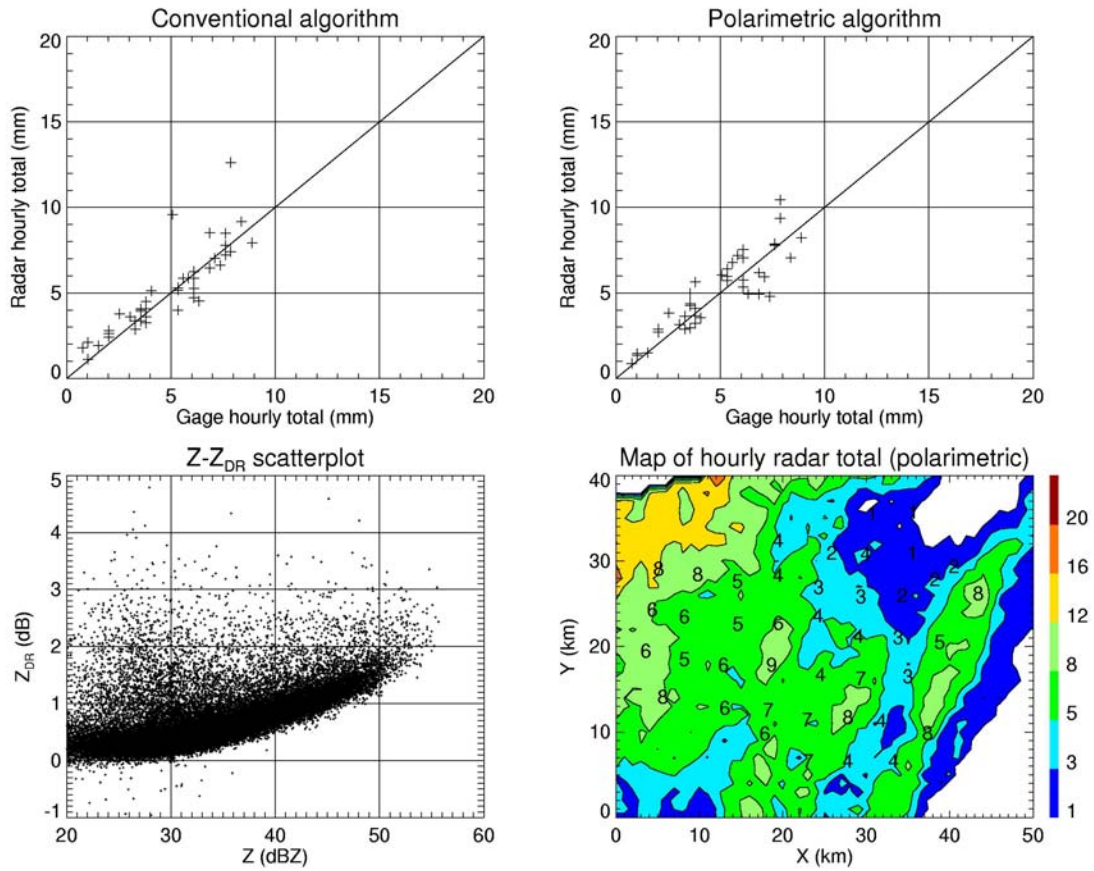


Fig. B10 – Hourly ARS gage totals versus estimates from the $R(Z)$ and $R(Z, K_{DP}, Z_{DR})$ algorithm (top panels), a $Z-Z_{DR}$ scattergram, and a map of the hourly radar rainfall totals with superimposed gage accumulations (bottom panels) for 9 September 2002 (16-17Z).

Squall line with trailing stratiform precipitation and embedded hail.



	BIAS [mm]	Standard Deviation [mm]	RMSE [mm]
Conventional	0.30	1.21	1.25
Polarimetric	0.23	1.03	1.05

Fig. B11 – Hourly ARS gage totals versus estimates from the R(Z) and R(Z, K_{DP}, Z_{DR}) algorithm (top panels), a Z-Z_{DR} scattergram, and a map of the hourly radar rainfall totals with superimposed gage accumulations (bottom panels) for 14 September 2002 (7-8Z).

Squall line with trailing stratiform precipitation and embedded hail.

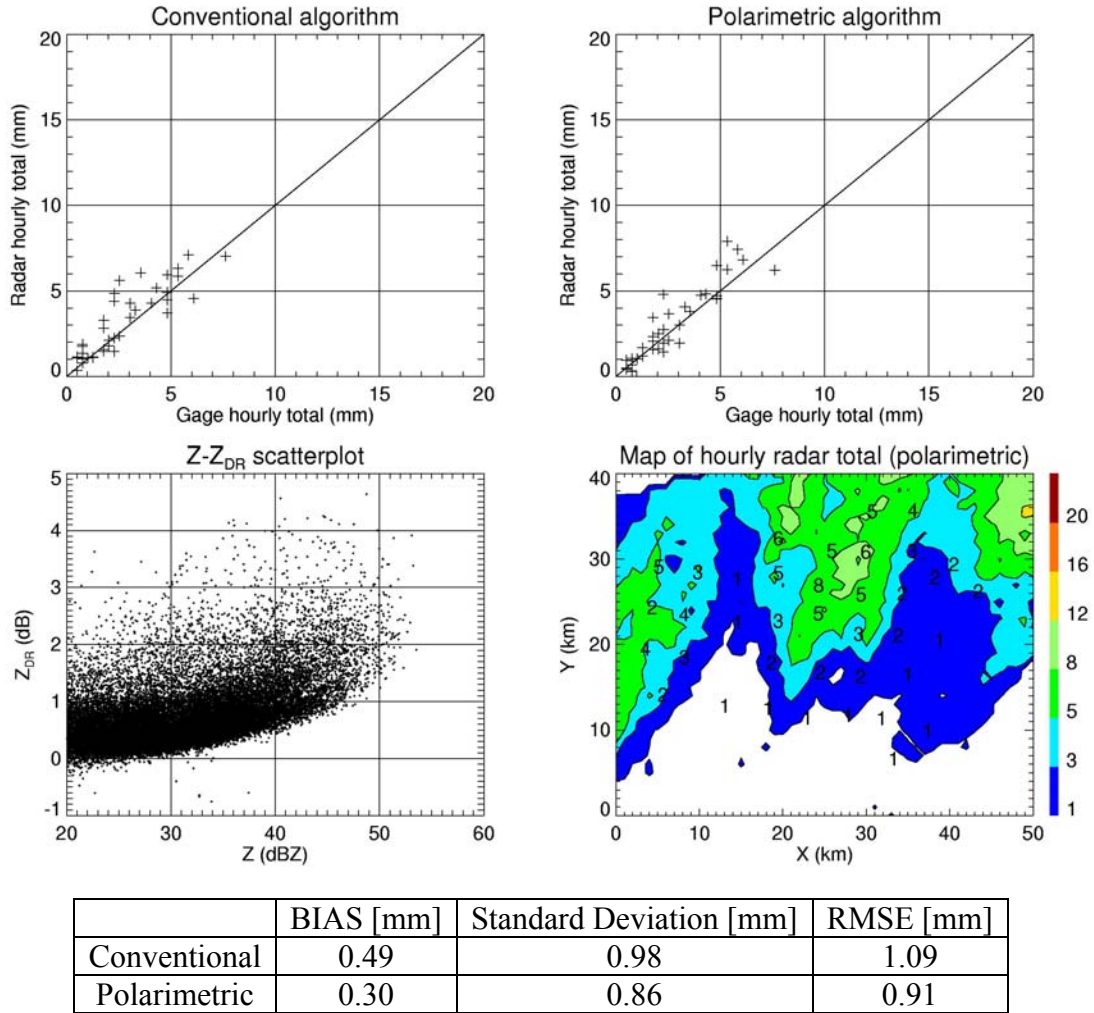
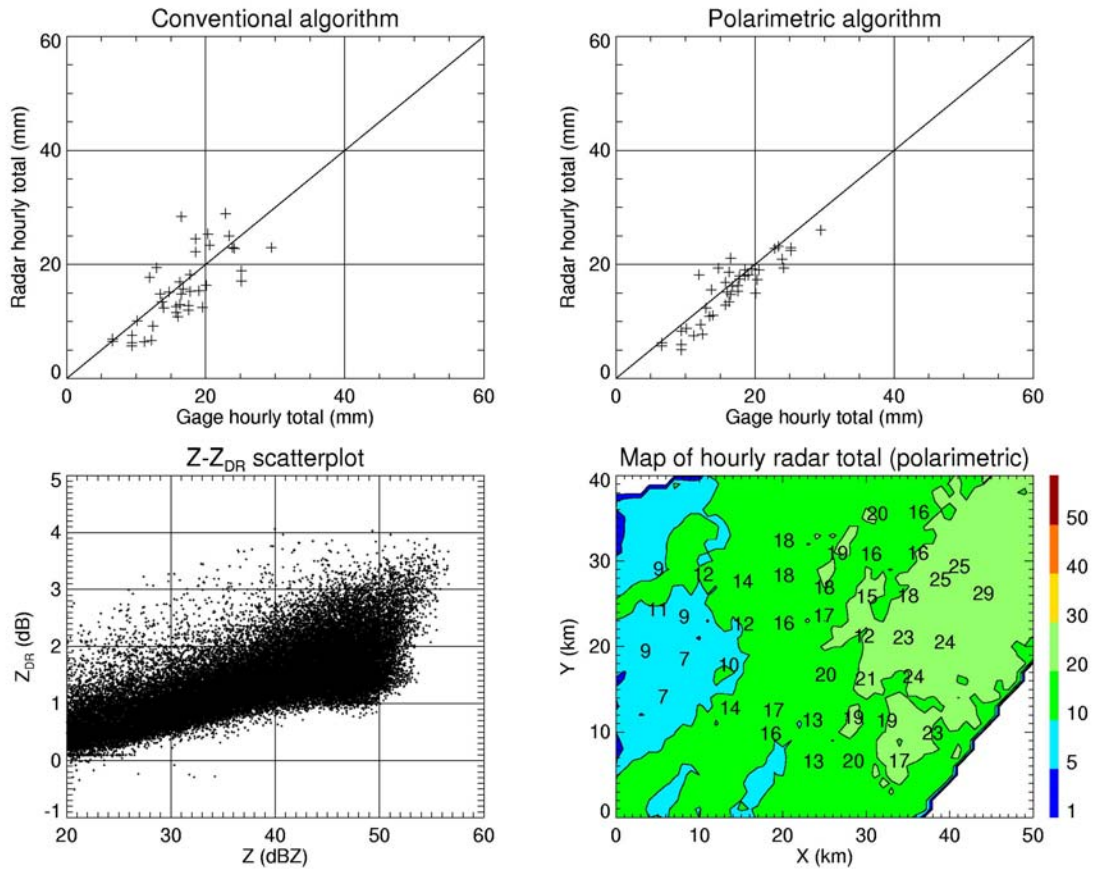


Fig. B12 – Hourly ARS gage totals versus estimates from the R(Z) and R(Z, K_{DP} , Z_{DR}) algorithm (top panels), a Z- Z_{DR} scattergram, and a map of the hourly radar rainfall totals with superimposed gage accumulations (bottom panels) for 14 September 2002 (8-9Z).

Leading edge of an intense squall line passing through central Oklahoma.



	BIAS [mm]	Standard Deviation [mm]	RMSE [mm]
Conventional	-0.99	4.27	4.39
Polarimetric	-1.16	2.47	2.73

Fig. B13 – Hourly ARS gage totals versus estimates from the R(Z) and R(Z, K_{DP}, Z_{DR}) algorithm (top panels), a Z-Z_{DR} scattergram, and a map of the hourly radar rainfall totals with superimposed gage accumulations (bottom panels) for 19 September 2002 (4-5Z).

Precipitation associated with the rear edge of a squall line passing through central Oklahoma.

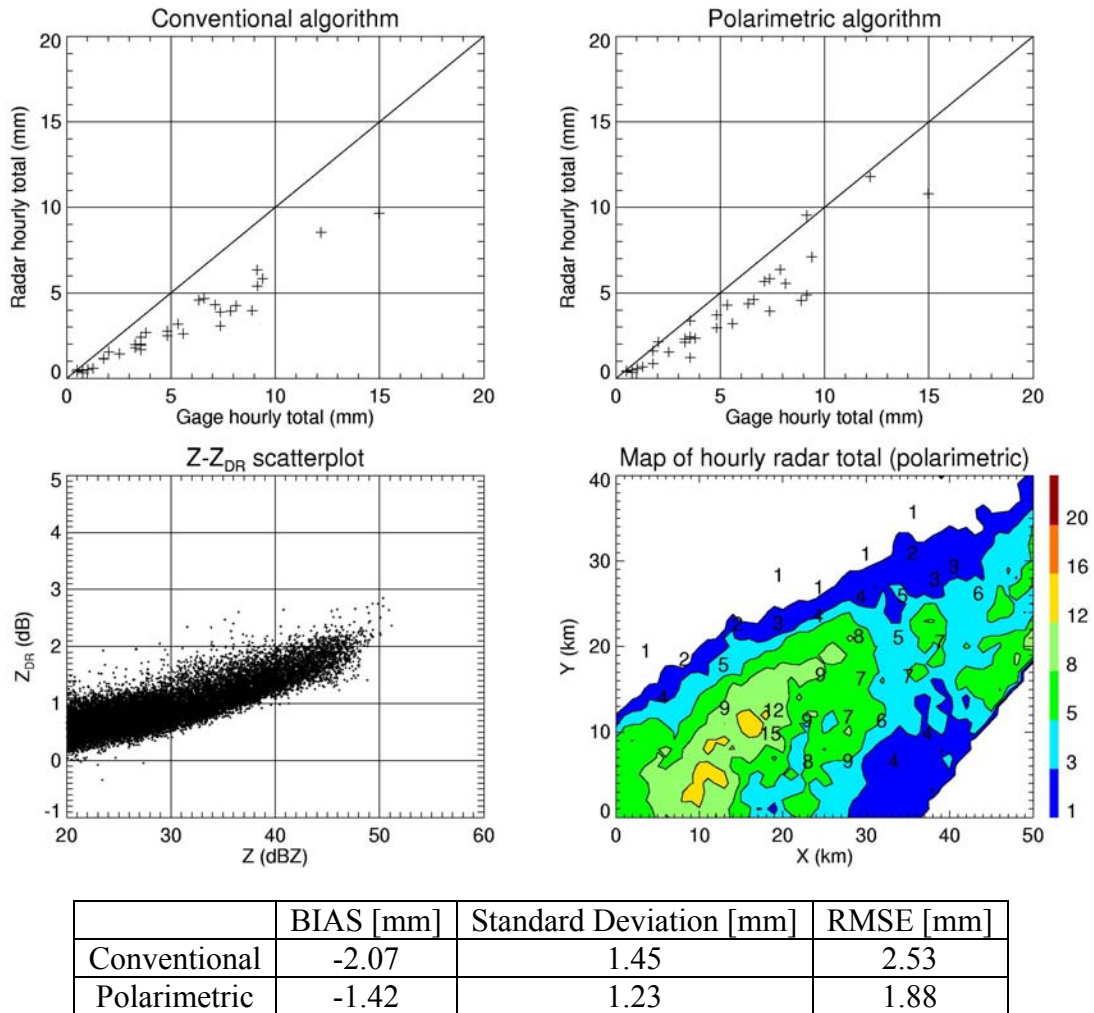


Fig. B14 – Hourly ARS gage totals versus estimates from the R(Z) and R(Z, K_{DP} , Z_{DR}) algorithm (top panels), a Z- Z_{DR} scattergram, and a map of the hourly radar rainfall totals with superimposed gage accumulations (bottom panels) for 19 September 2002 (5-6Z).

Widespread stratiform precipitation over central Oklahoma.

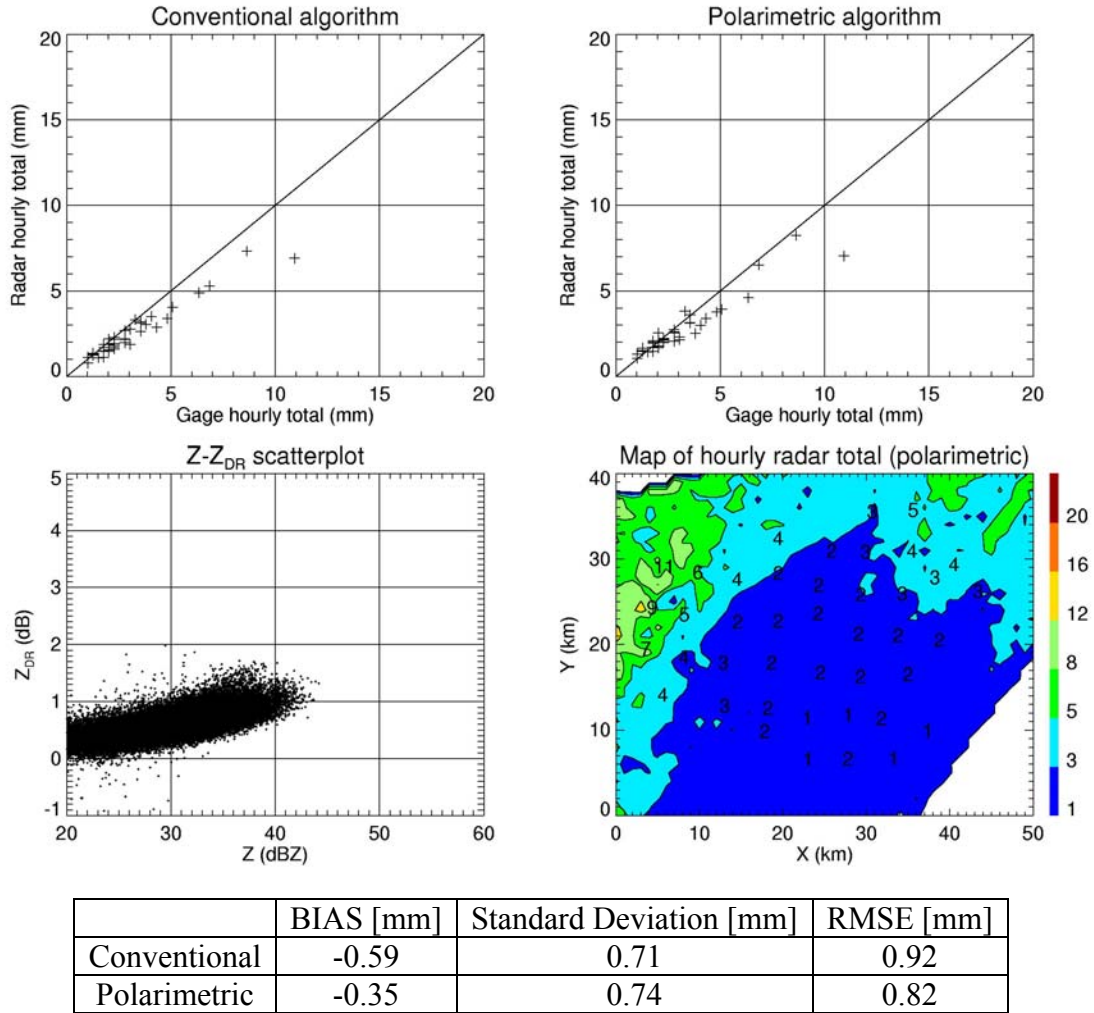


Fig. B15 – Hourly ARS gage totals versus estimates from the $R(Z)$ and $R(Z, K_{DP}, Z_{DR})$ algorithm (top panels), a $Z-Z_{DR}$ scattergram, and a map of the hourly radar rainfall totals with superimposed gage accumulations (bottom panels) for 8 October 2002 (17-18Z).

Widespread stratiform precipitation over central Oklahoma.

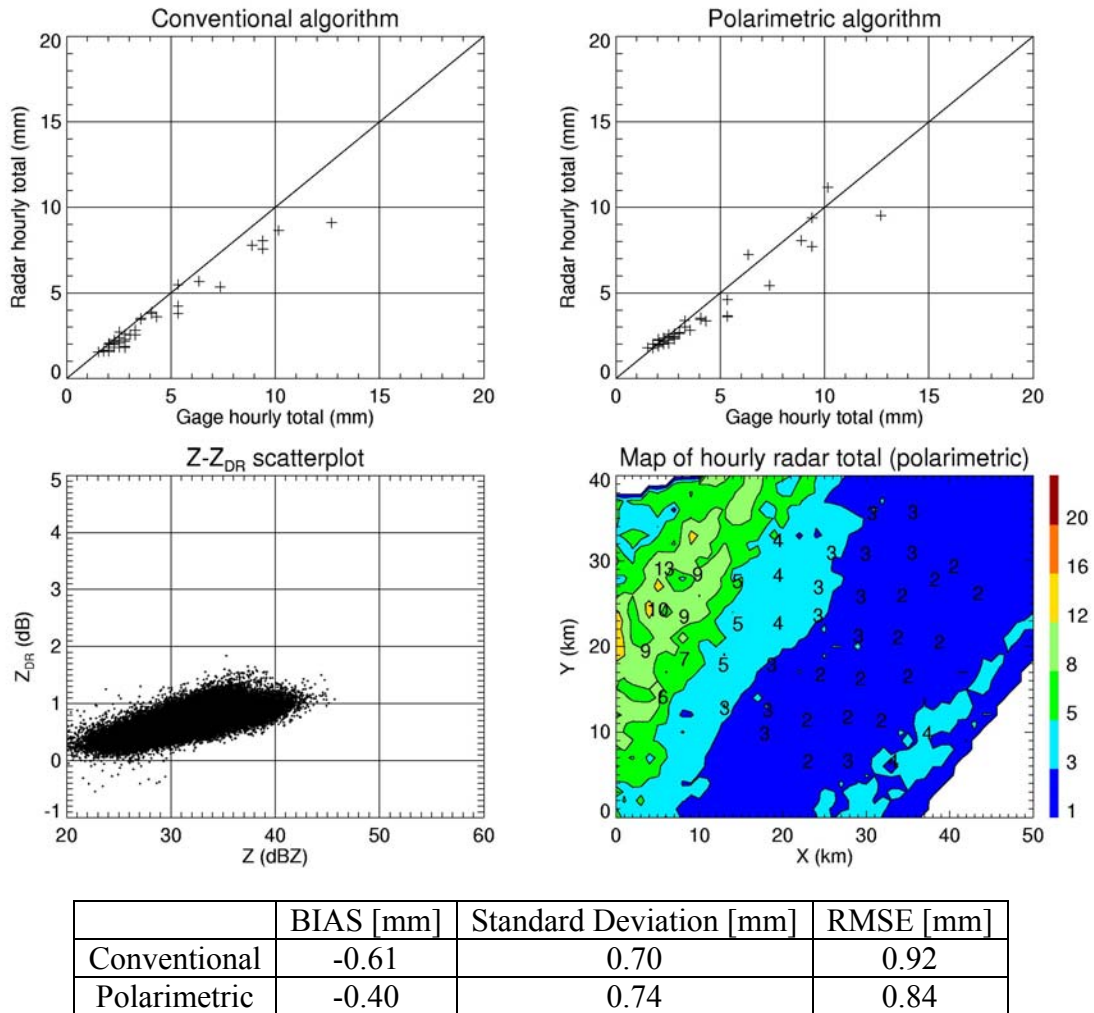


Fig. B16 – Hourly ARS gage totals versus estimates from the R(Z) and R(Z, K_{DP}, Z_{DR}) algorithm (top panels), a Z-Z_{DR} scattergram, and a map of the hourly radar rainfall totals with superimposed gage accumulations (bottom panels) for 8 October 2002 (18-19Z).

Widespread stratiform precipitation over central Oklahoma.

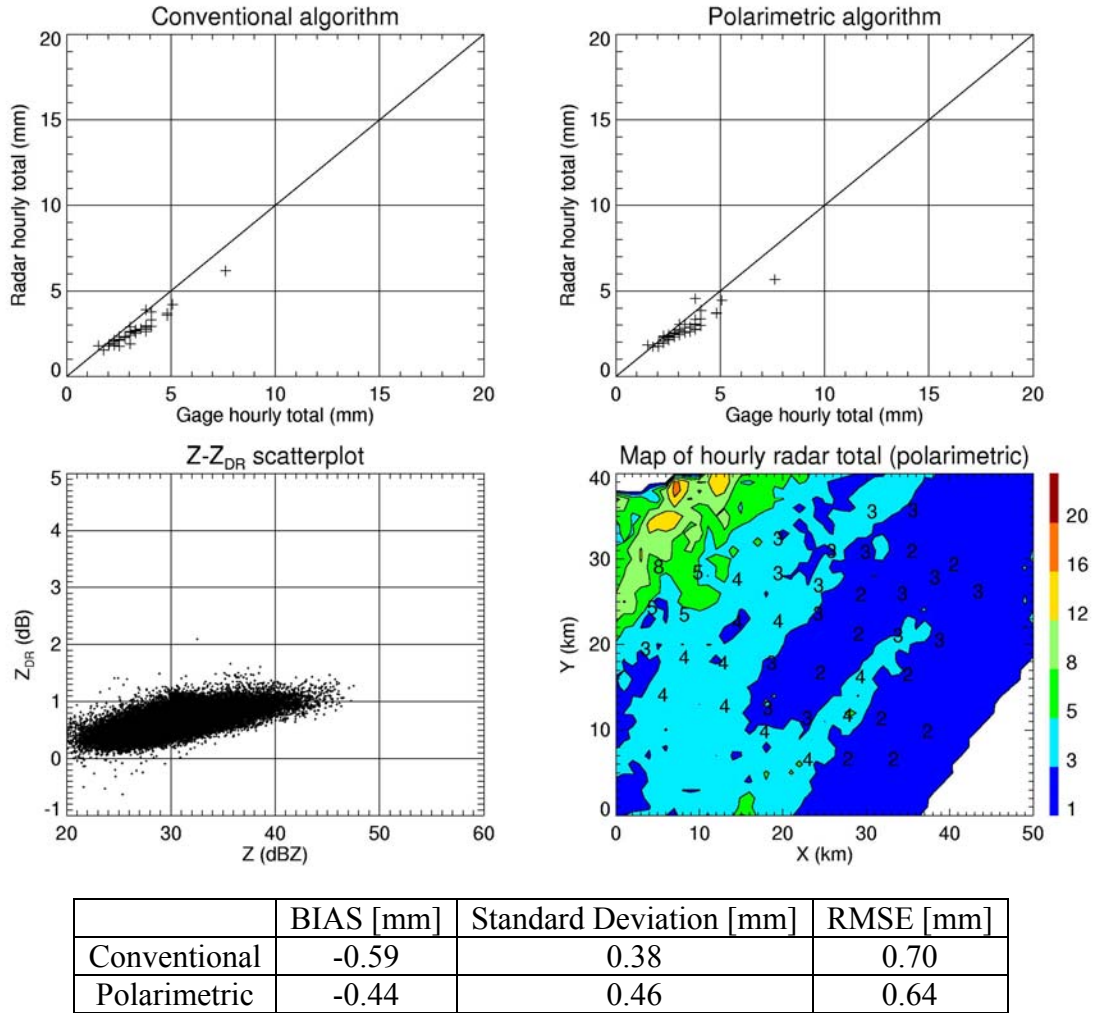


Fig. B17 – Hourly ARS gage totals versus estimates from the R(Z) and R(Z, K_{DP}, Z_{DR}) algorithm (top panels), a Z-Z_{DR} scattergram, and a map of the hourly radar rainfall totals with superimposed gage accumulations (bottom panels) for 8 October 2002 (19-20Z).

Widespread stratiform precipitation over central Oklahoma.

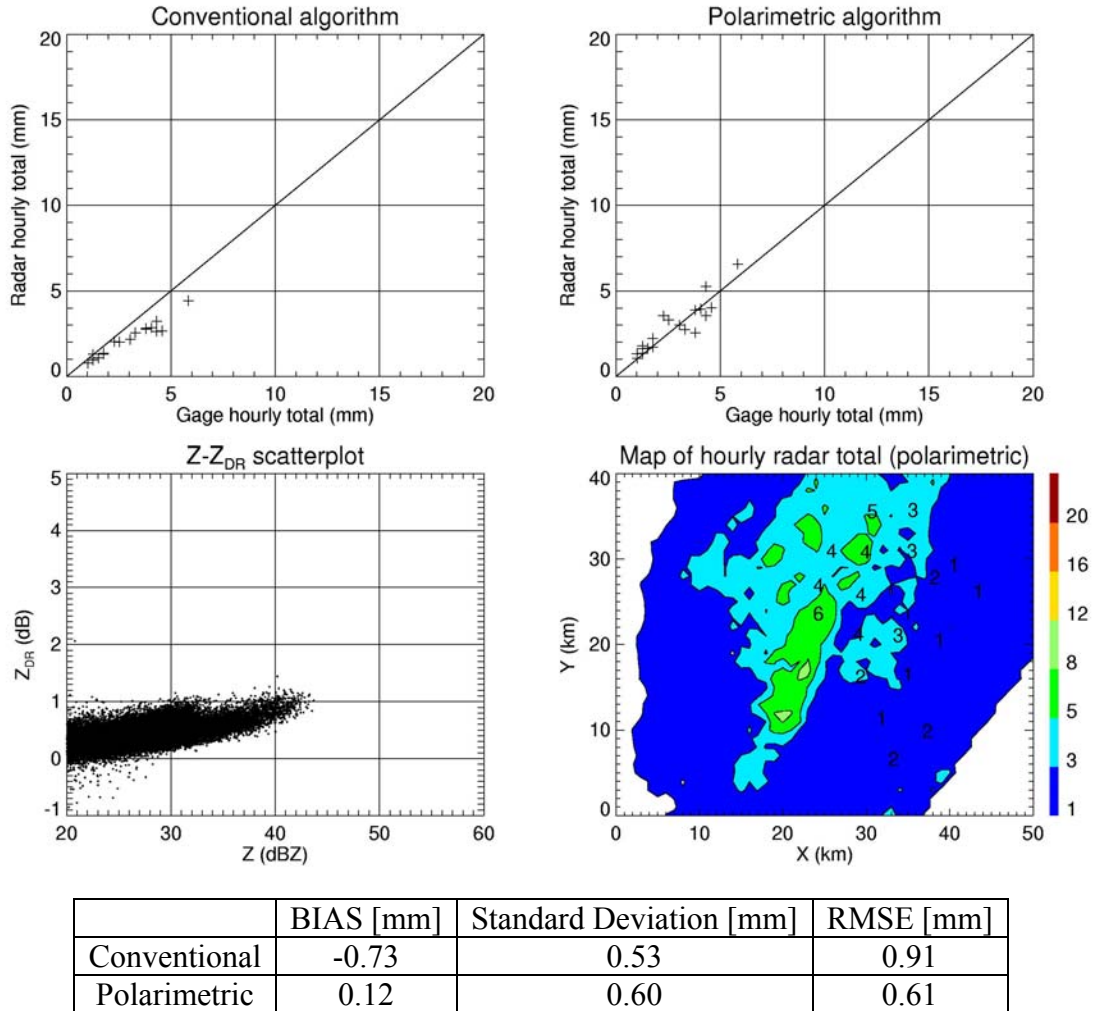


Fig. B18 – Hourly ARS gage totals versus estimates from the R(Z) and R(Z, K_{DP}, Z_{DR}) algorithm (top panels), a Z-Z_{DR} scattergram, and a map of the hourly radar rainfall totals with superimposed gage accumulations (bottom panels) for 8 October 2002 (22-23Z).

Widespread stratiform precipitation over central Oklahoma.

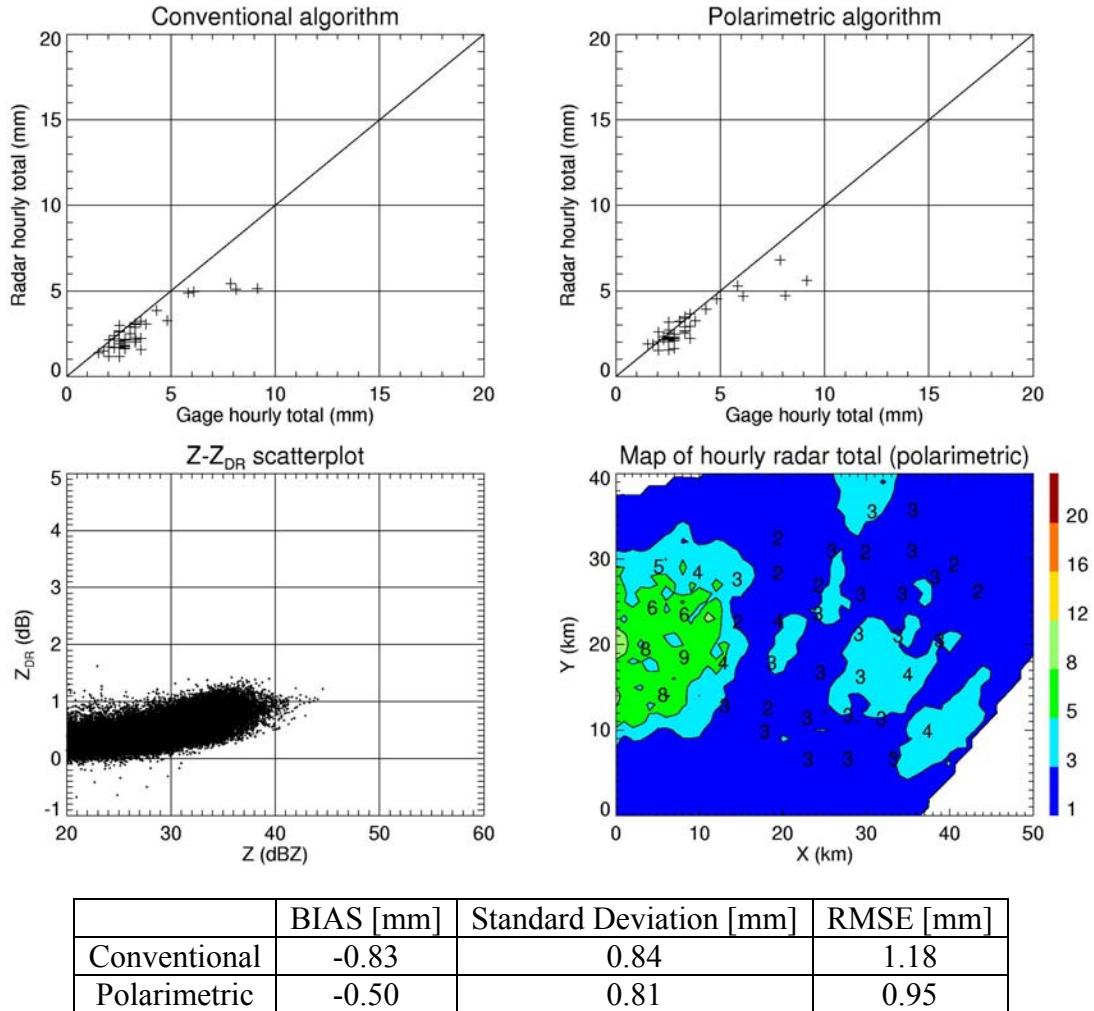


Fig. B19 – Hourly ARS gage totals versus estimates from the R(Z) and R(Z, K_{DP}, Z_{DR}) algorithm (top panels), a Z-Z_{DR} scattergram, and a map of the hourly radar rainfall totals with superimposed gage accumulations (bottom panels) for 9 October 2002 (1-2Z).

Widespread stratiform precipitation over central Oklahoma.

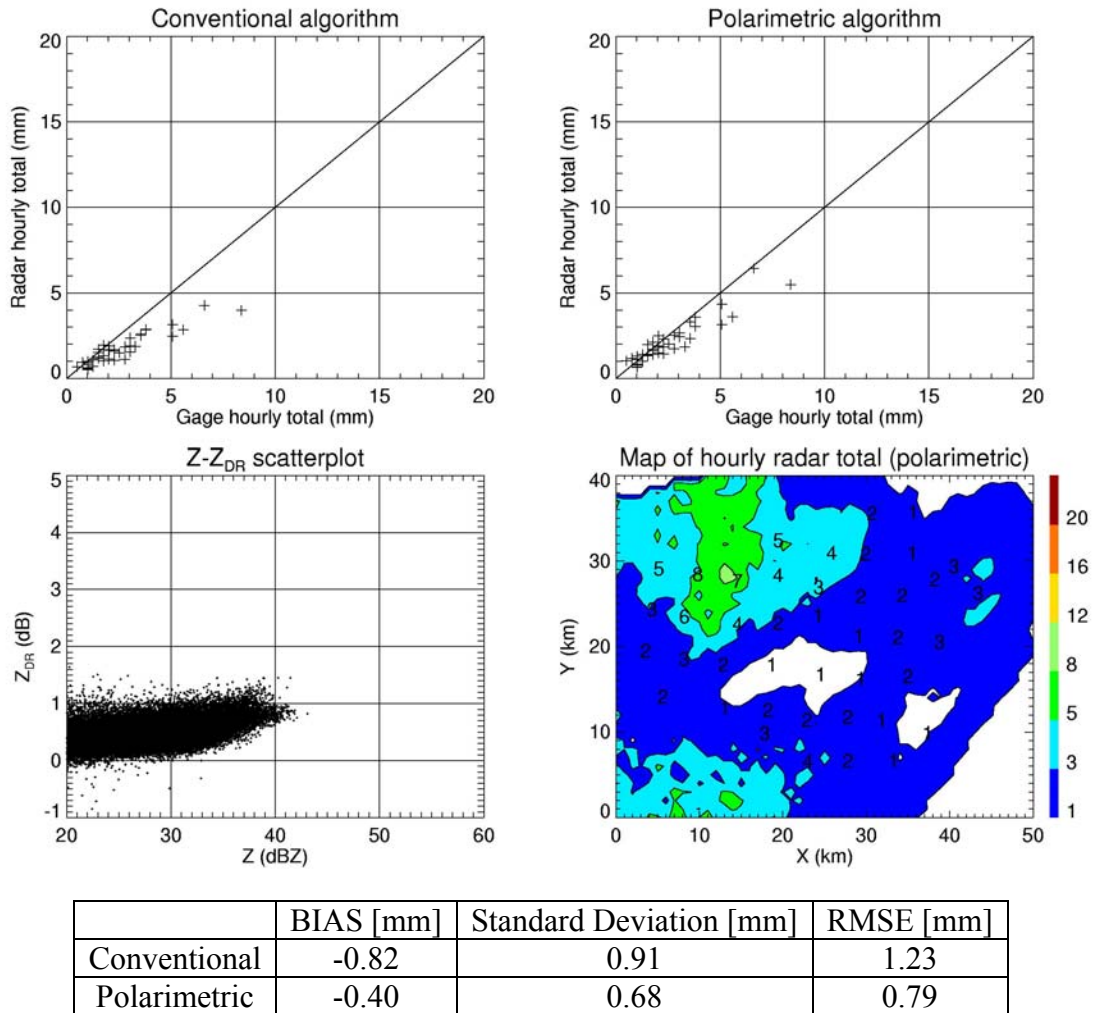


Fig. B20 – Hourly ARS gage totals versus estimates from the $R(Z)$ and $R(Z, K_{DP}, Z_{DR})$ algorithm (top panels), a $Z-Z_{DR}$ scattergram, and a map of the hourly radar rainfall totals with superimposed gage accumulations (bottom panels) for 9 October 2002 (2-3Z).

Scattered stratiform precipitation over central Oklahoma with developing convective cells.

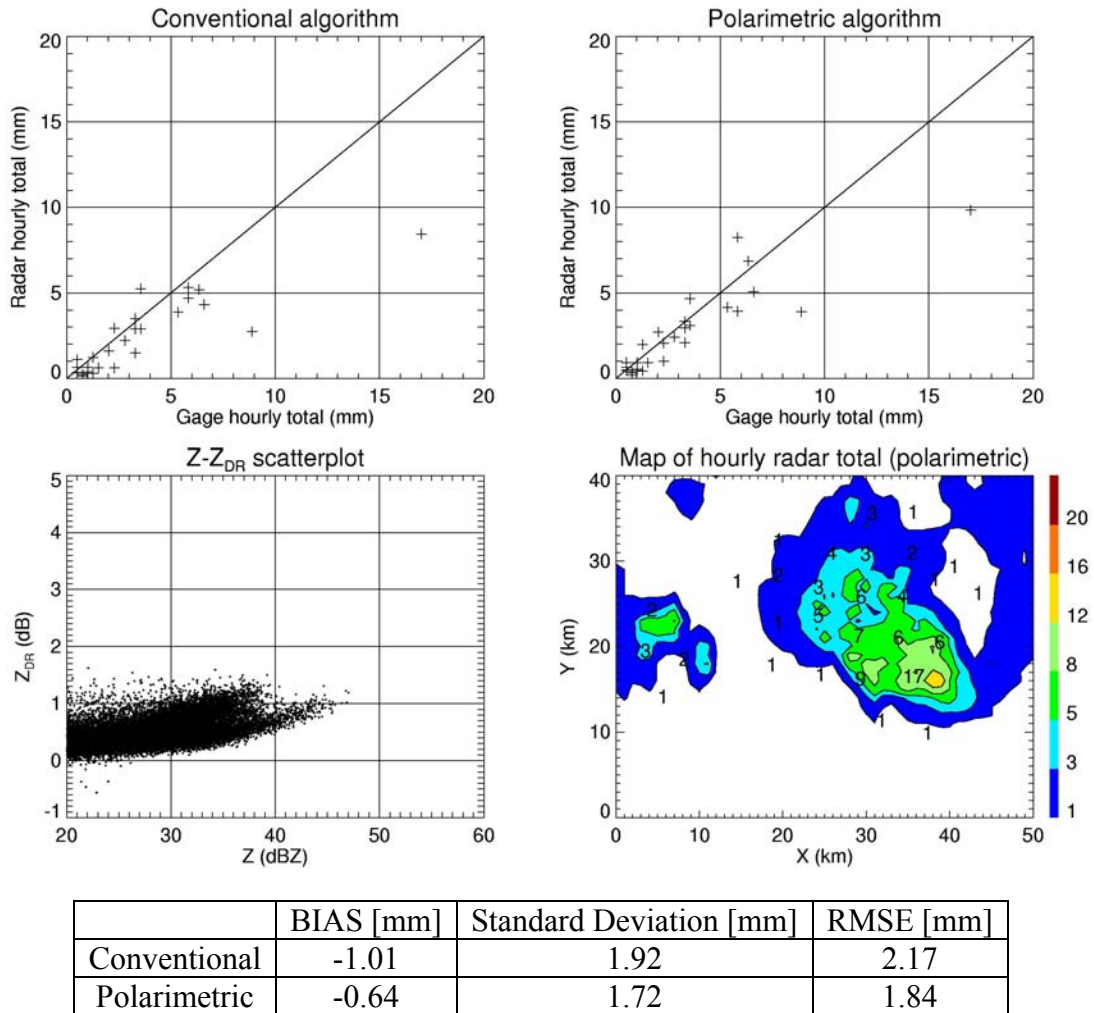


Fig. B21 – Hourly ARS gage totals versus estimates from the R(Z) and R(Z, K_{DP}, Z_{DR}) algorithm (top panels), a Z-Z_{DR} scattergram, and a map of the hourly radar rainfall totals with superimposed gage accumulations (bottom panels) for 9 October 2002 (13-14Z).

Stratiform precipitation with embedded weak convective cells.

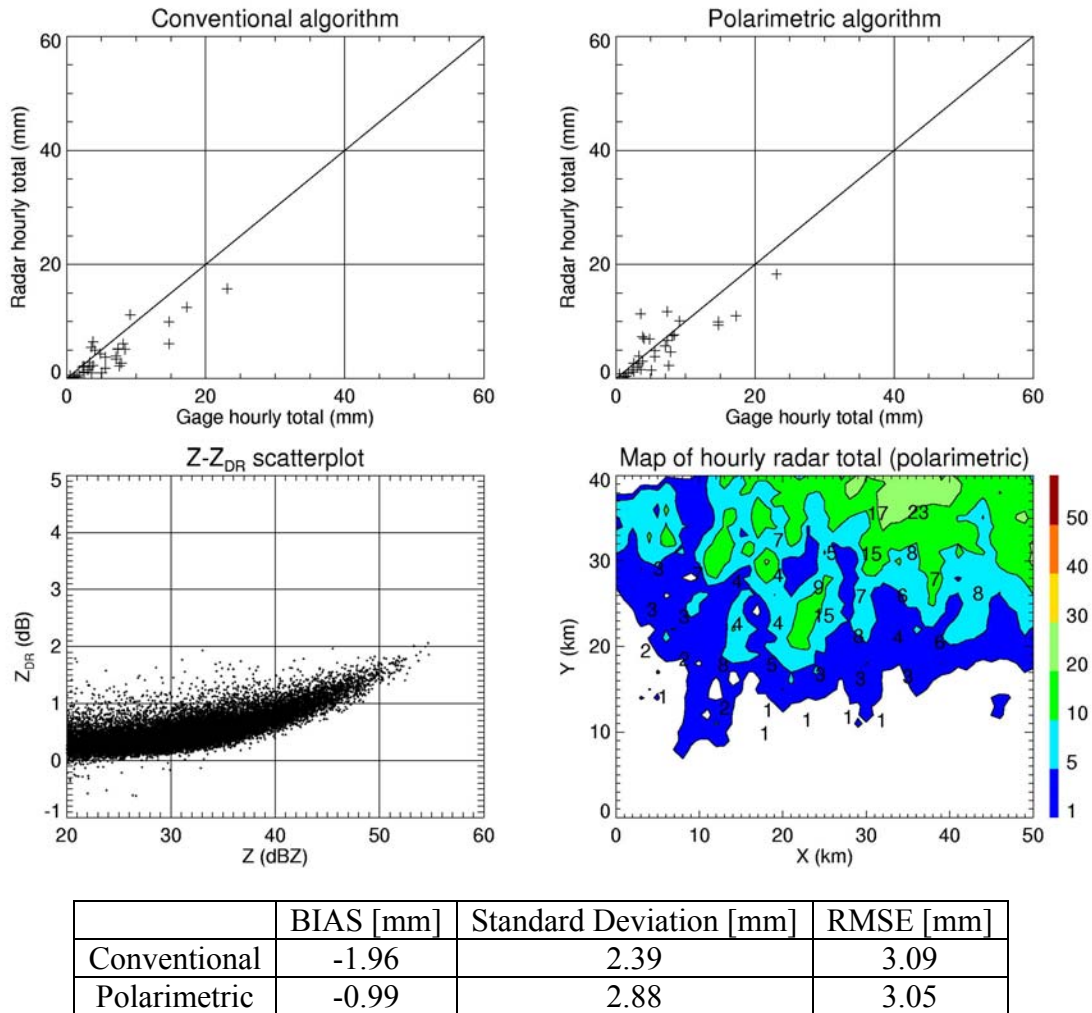


Fig. B22 – Hourly ARS gage totals versus estimates from the R(Z) and R(Z, K_{DP}, Z_{DR}) algorithm (top panels), a Z-Z_{DR} scattergram, and a map of the hourly radar rainfall totals with superimposed gage accumulations (bottom panels) for 19 October 2002 (19-20Z).

Stratiform precipitation with embedded weak convective cells.

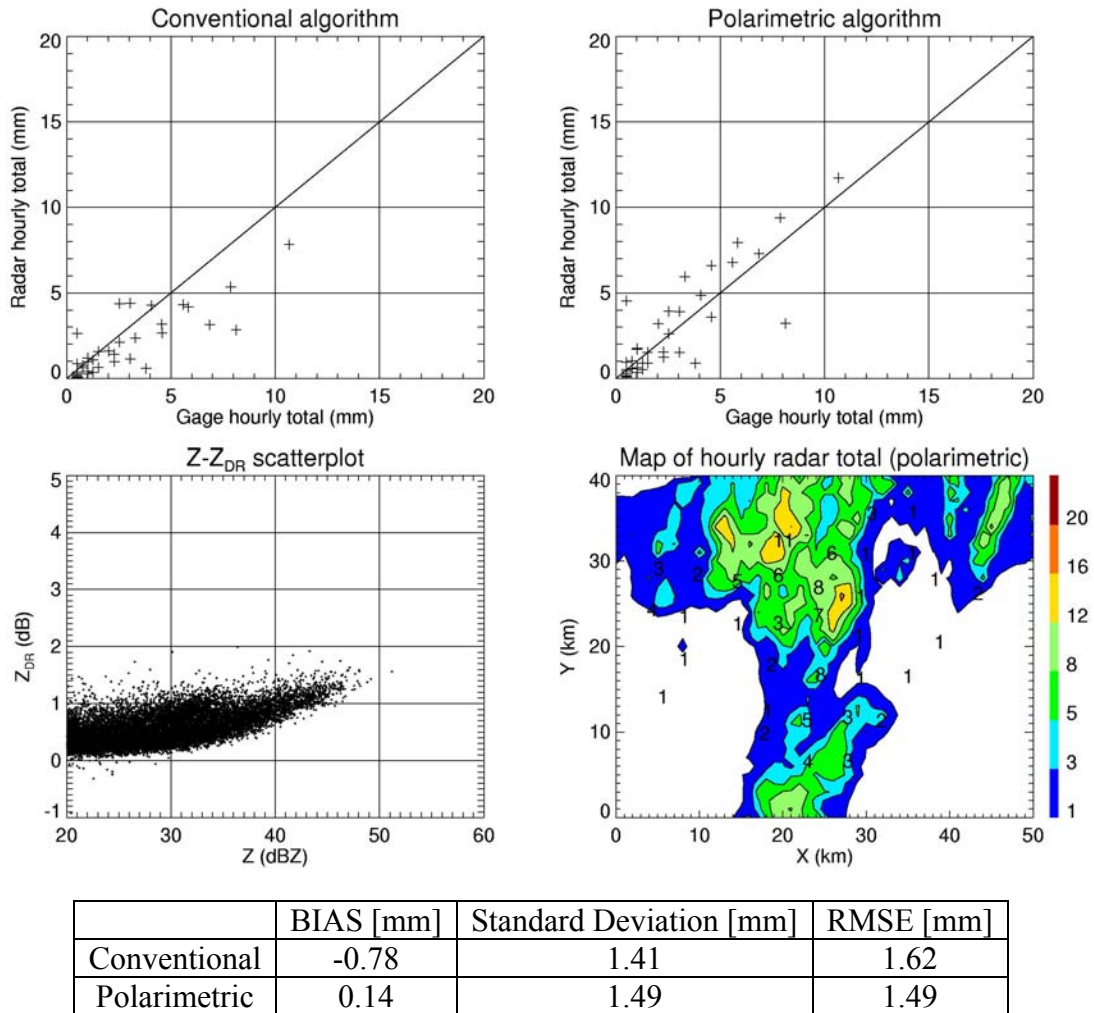


Fig. B23 – Hourly ARS gage totals versus estimates from the R(Z) and R(Z, K_{DP} , Z_{DR}) algorithm (top panels), a Z- Z_{DR} scattergram, and a map of the hourly radar rainfall totals with superimposed gage accumulations (bottom panels) for 19 October 2002 (21-22Z).

Stratiform precipitation over central Oklahoma.

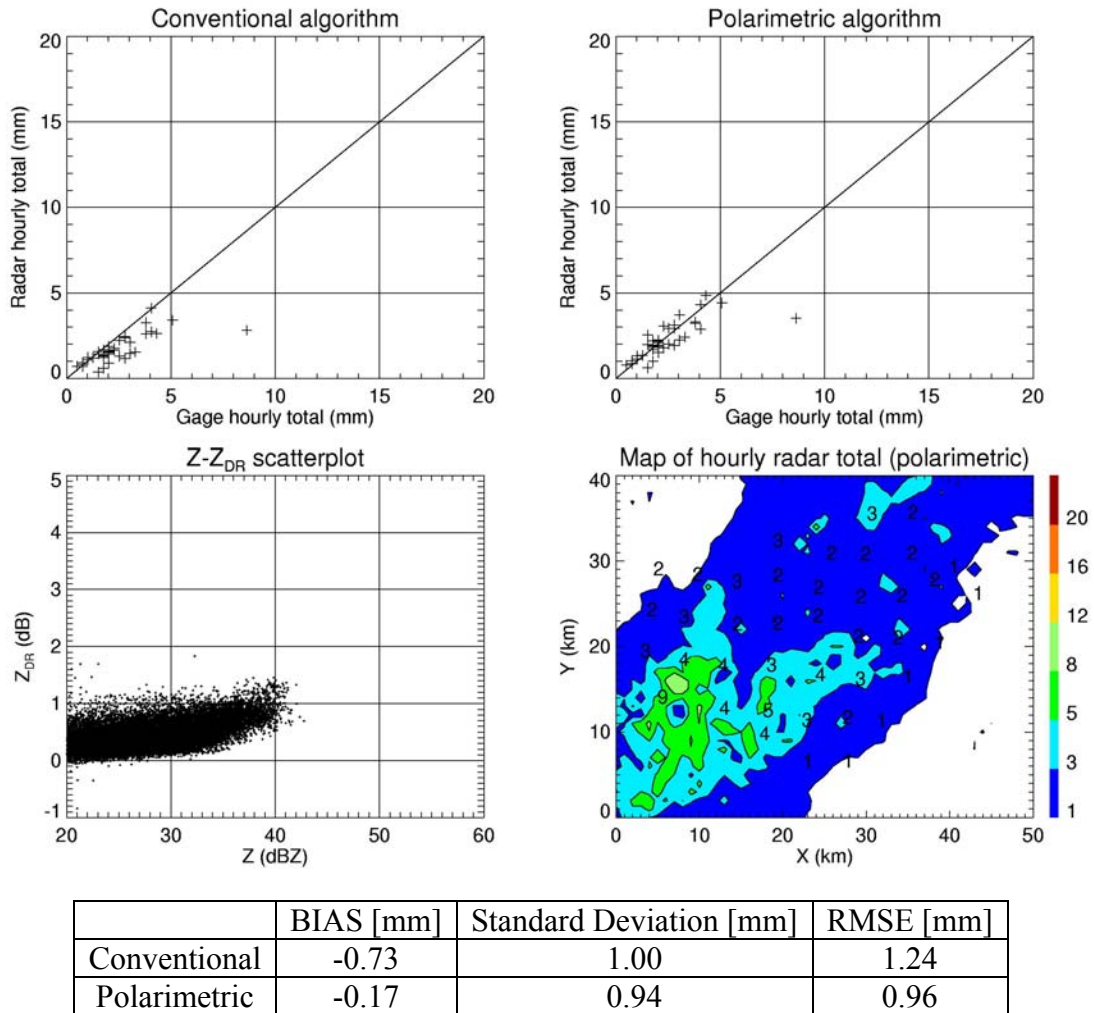
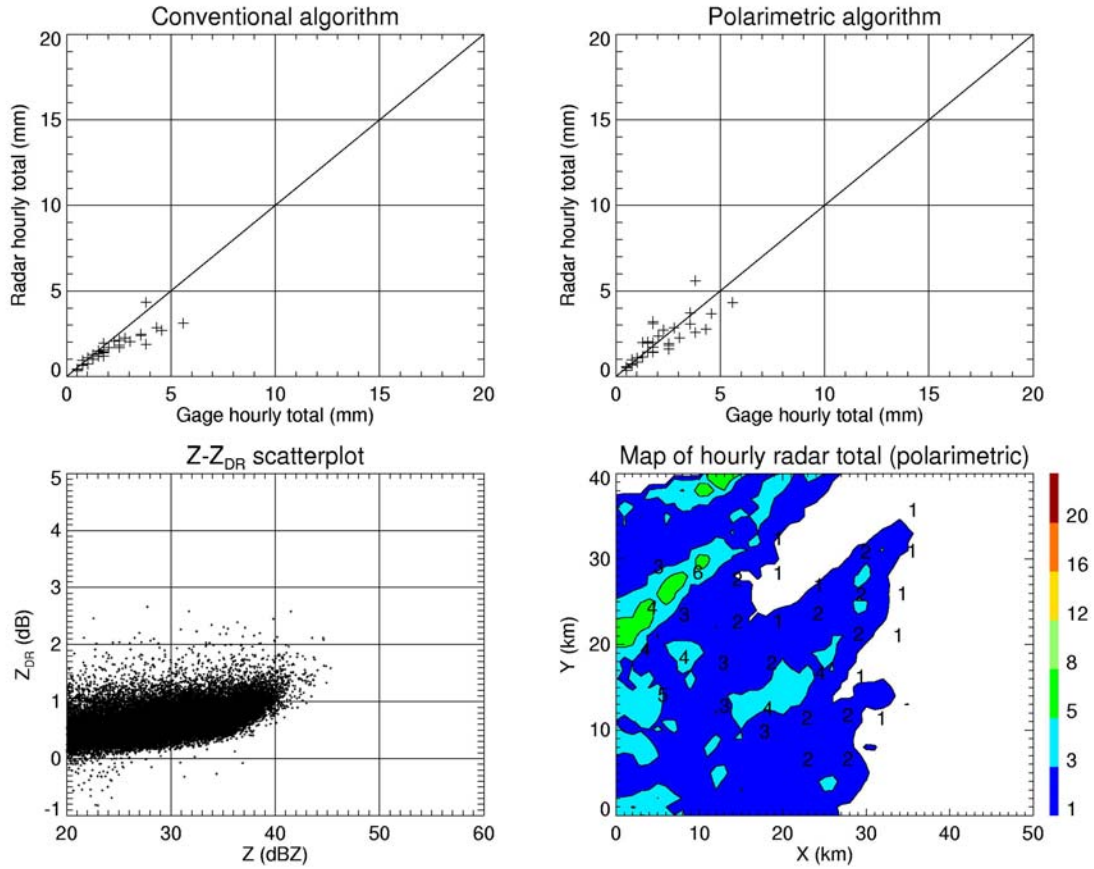


Fig. B24 – Hourly ARS gage totals versus estimates from the R(Z) and R(Z, K_{DP}, Z_{DR}) algorithm (top panels), a Z-Z_{DR} scattergram, and a map of the hourly radar rainfall totals with superimposed gage accumulations (bottom panels) for 23 October 2002 (16-17Z).

Moderate stratiform precipitation over central Oklahoma.



	BIAS [mm]	Standard Deviation [mm]	RMSE [mm]
Conventional	-0.51	0.65	0.83
Polarimetric	-0.07	0.73	0.73

Fig. B25 – Hourly ARS gage totals versus estimates from the R(Z) and R(Z, K_{DP}, Z_{DR}) algorithm (top panels), a Z-Z_{DR} scattergram, and a map of the hourly radar rainfall totals with superimposed gage accumulations (bottom panels) for 24 October 2002 (15-16Z).

Moderate stratiform precipitation over central Oklahoma.

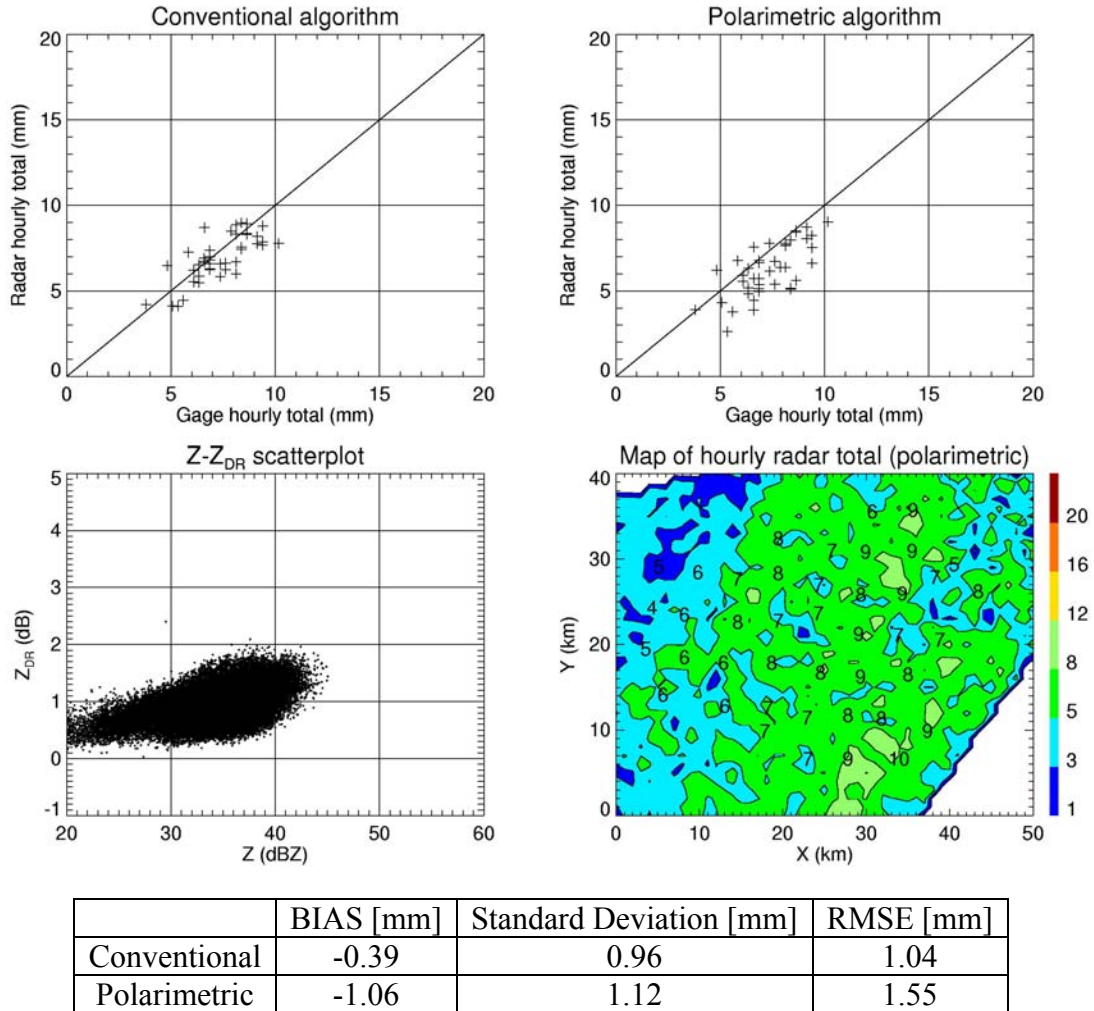


Fig. B26 – Hourly ARS gage totals versus estimates from the R(Z) and R(Z, K_{DP}, Z_{DR}) algorithm (top panels), a Z-Z_{DR} scattergram, and a map of the hourly radar rainfall totals with superimposed gage accumulations (bottom panels) for 24 October 2002 (16-17Z).

Moderate stratiform precipitation over central Oklahoma.

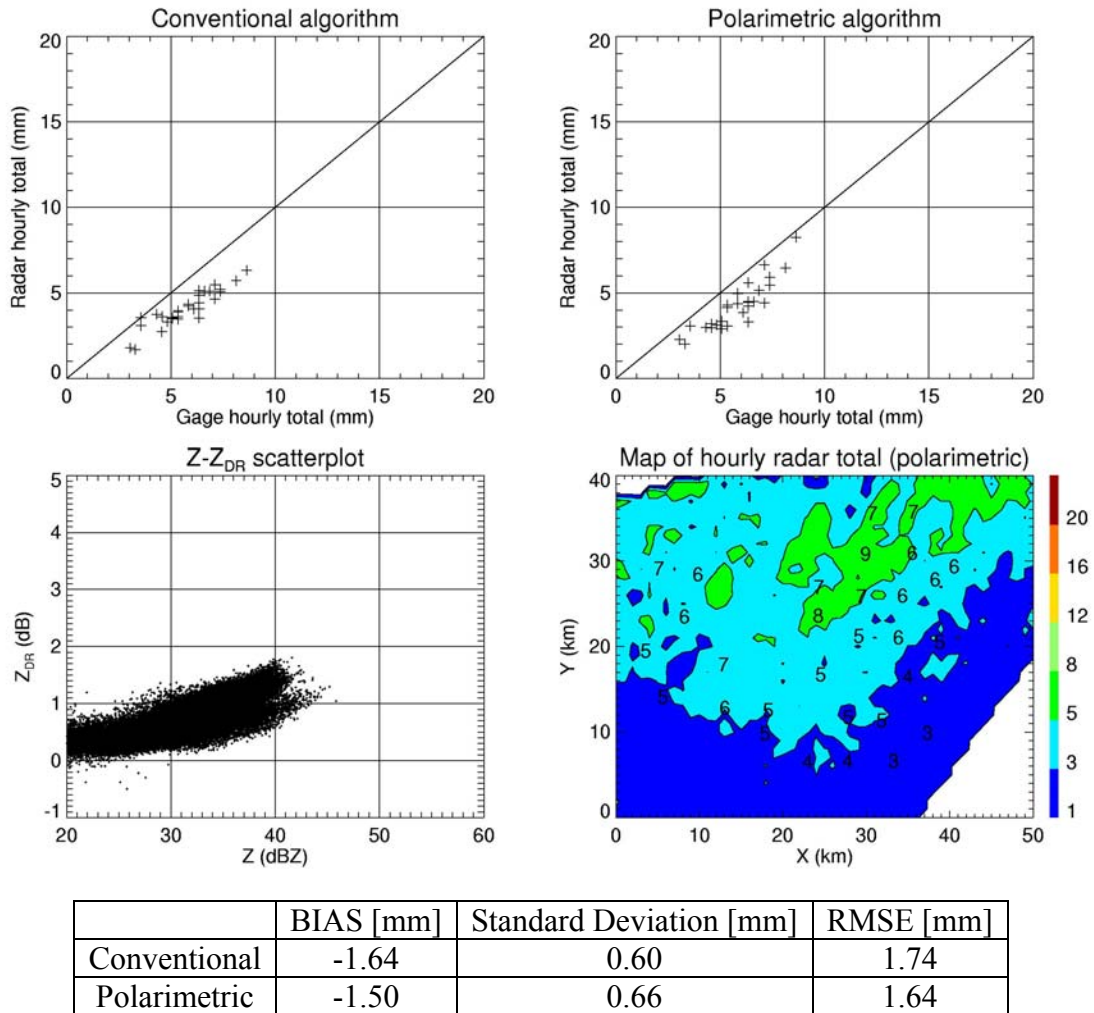


Fig. B27 – Hourly ARS gage totals versus estimates from the R(Z) and R(Z, K_{DP}, Z_{DR}) algorithm (top panels), a Z-Z_{DR} scattergram, and a map of the hourly radar rainfall totals with superimposed gage accumulations (bottom panels) for 24 October 2002 (19-20Z).

Moderate stratiform precipitation over central Oklahoma.

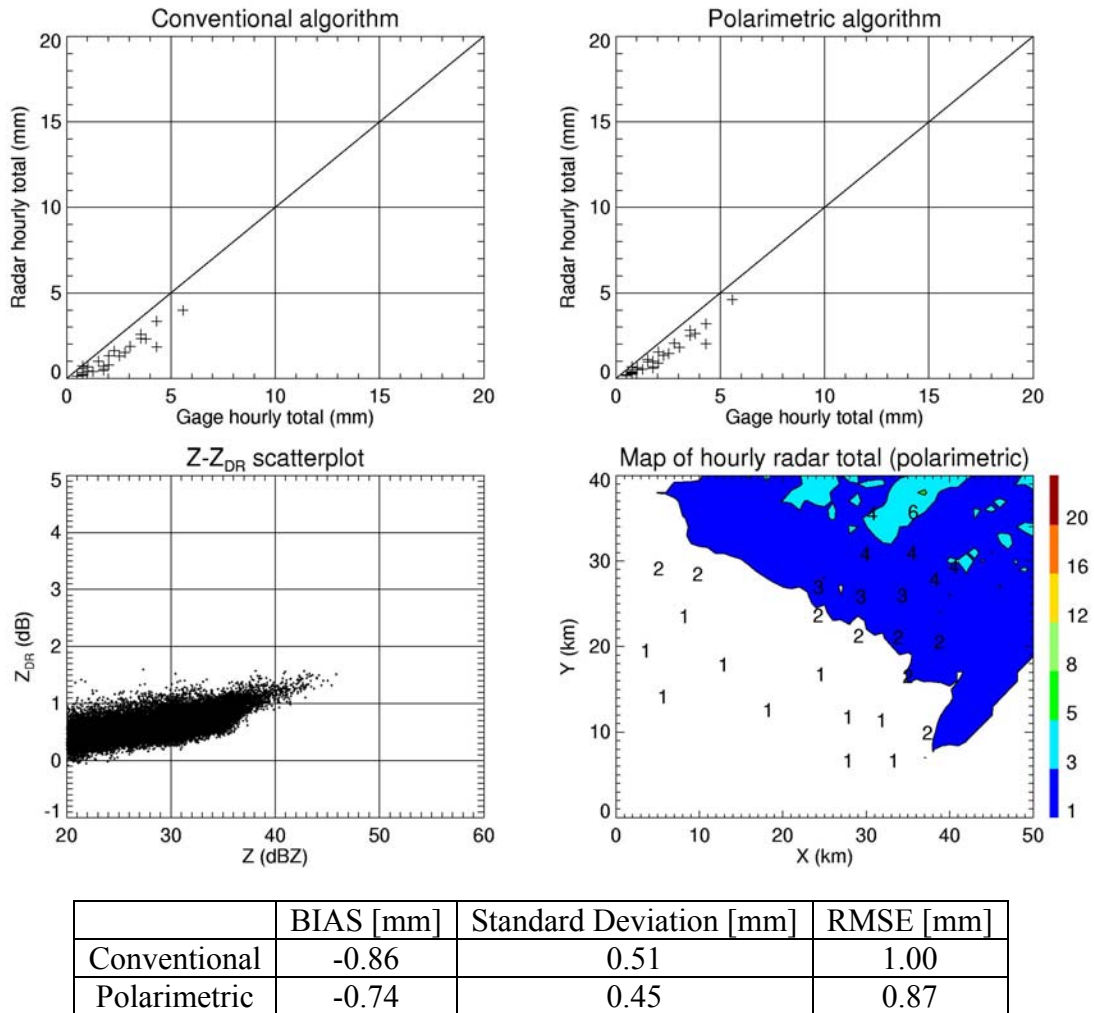
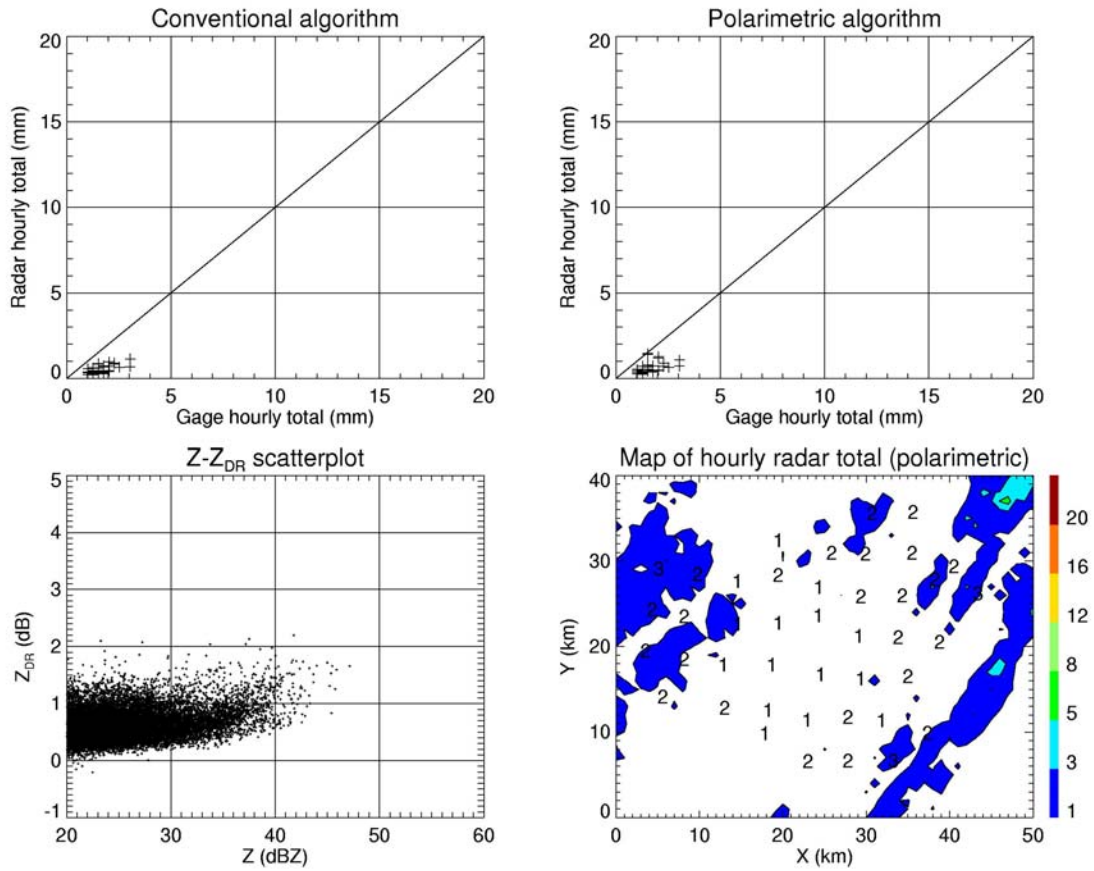


Fig. B28 – Hourly ARS gage totals versus estimates from the R(Z) and R(Z, K_{DP}, Z_{DR}) algorithm (top panels), a Z-Z_{DR} scattergram, and a map of the hourly radar rainfall totals with superimposed gage accumulations (bottom panels) for 24 October 2002 (20-21Z).

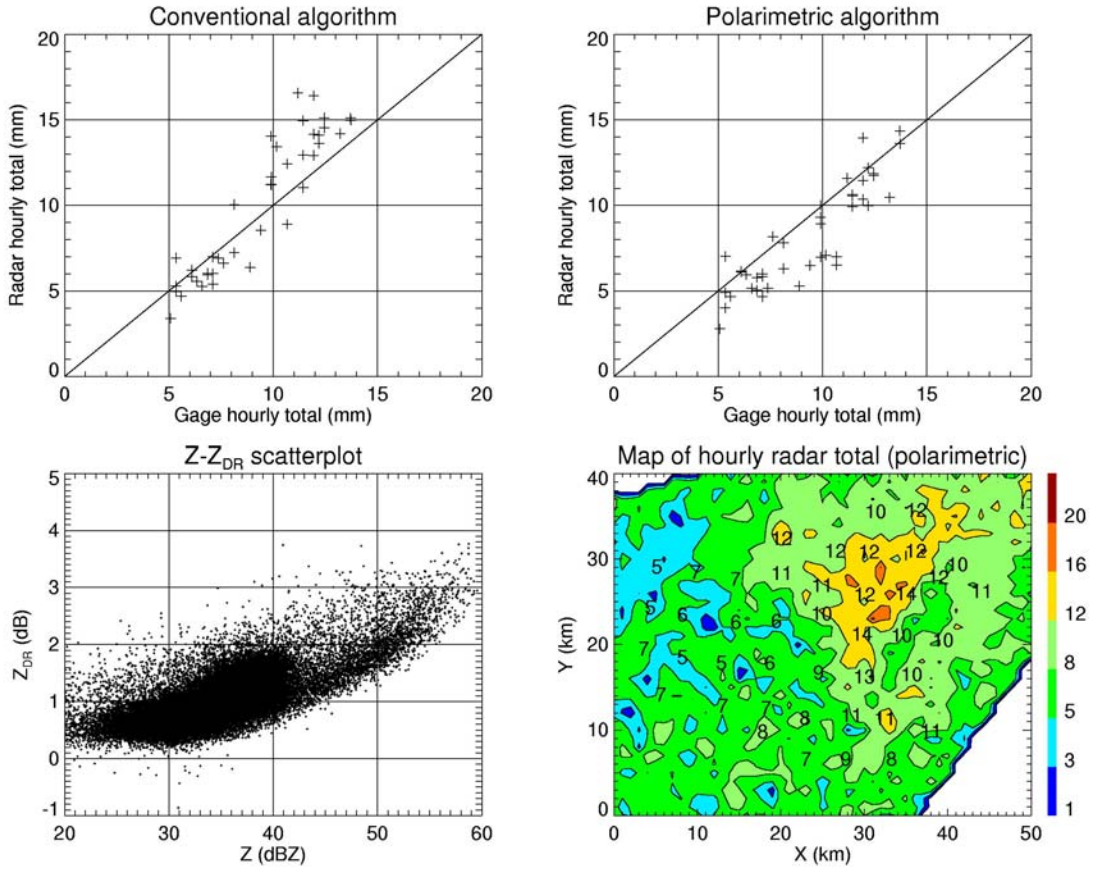
Stratiform precipitation over central Oklahoma associated with a cyclone over Kansas.



	BIAS [mm]	Standard Deviation [mm]	RMSE [mm]
Conventional	-1.15	0.39	1.22
Polarimetric	-1.06	0.44	1.15

Fig. B29 – Hourly ARS gage totals versus estimates from the R(Z) and R(Z, K_{DP}, Z_{DR}) algorithm (top panels), a Z-Z_{DR} scattergram, and a map of the hourly radar rainfall totals with superimposed gage accumulations (bottom panels) for 27 October 2002 (13-14Z).

Leading edge of a squall line with trailing stratiform precipitation over central Oklahoma.



	BIAS [mm]	Standard Deviation [mm]	RMSE [mm]
Conventional	0.73	1.82	1.96
Polarimetric	-1.13	1.36	1.77

Fig. B30 – Hourly ARS gage totals versus estimates from the R(Z) and R(Z, K_{DP}, Z_{DR}) algorithm (top panels), a Z-Z_{DR} scattergram, and a map of the hourly radar rainfall totals with superimposed gage accumulations (bottom panels) for 28 October 2002 (19-20Z).

Widespread stratiform precipitation over southern and central Oklahoma. Snowfall in northern and central Oklahoma.

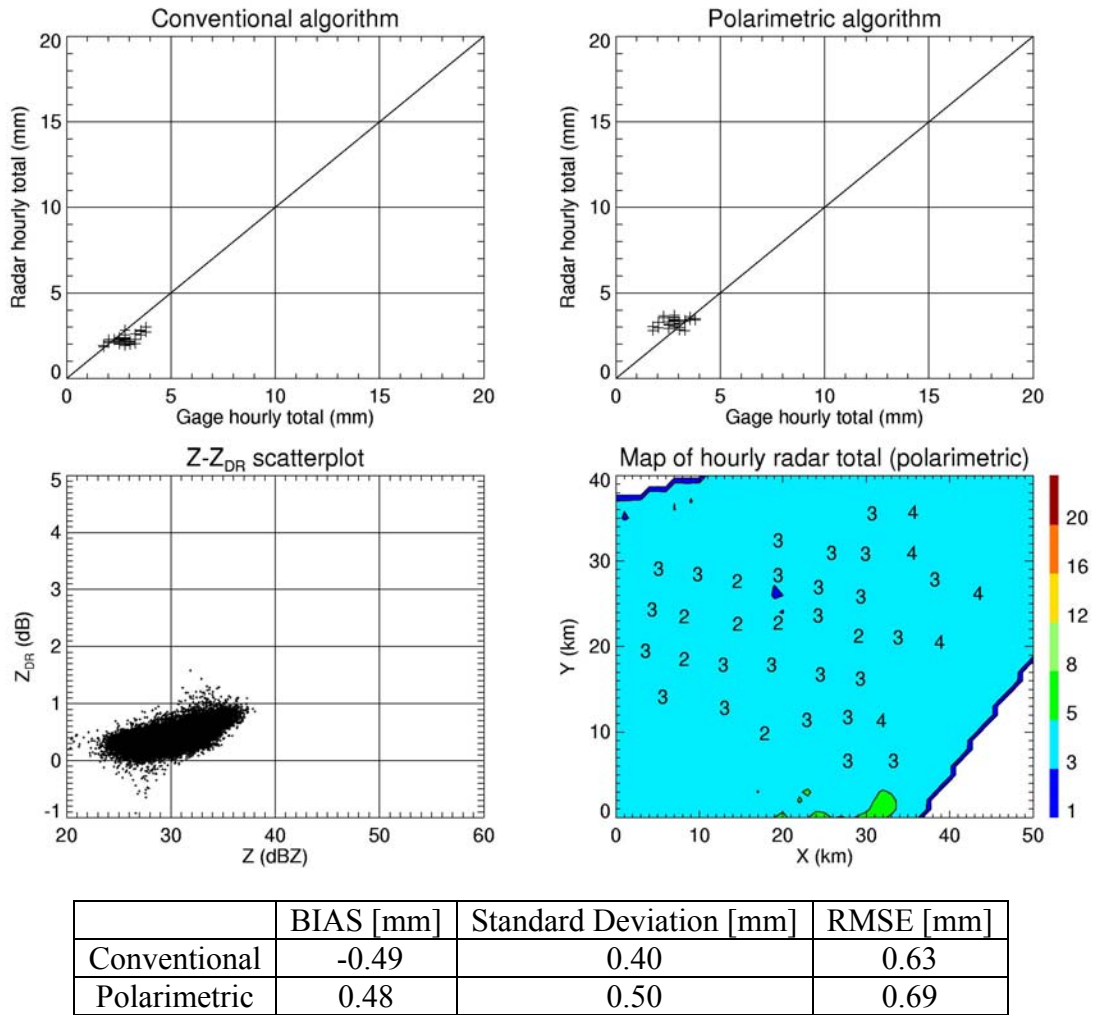


Fig. B31 – Hourly ARS gage totals versus estimates from the R(Z) and R(Z, K_{DP}, Z_{DR}) algorithm (top panels), a Z-Z_{DR} scattergram, and a map of the hourly radar rainfall totals with superimposed gage accumulations (bottom panels) for 3 December 2002 (22-23Z).

Widespread stratiform precipitation over southern and central Oklahoma. Snowfall in northern and central Oklahoma.

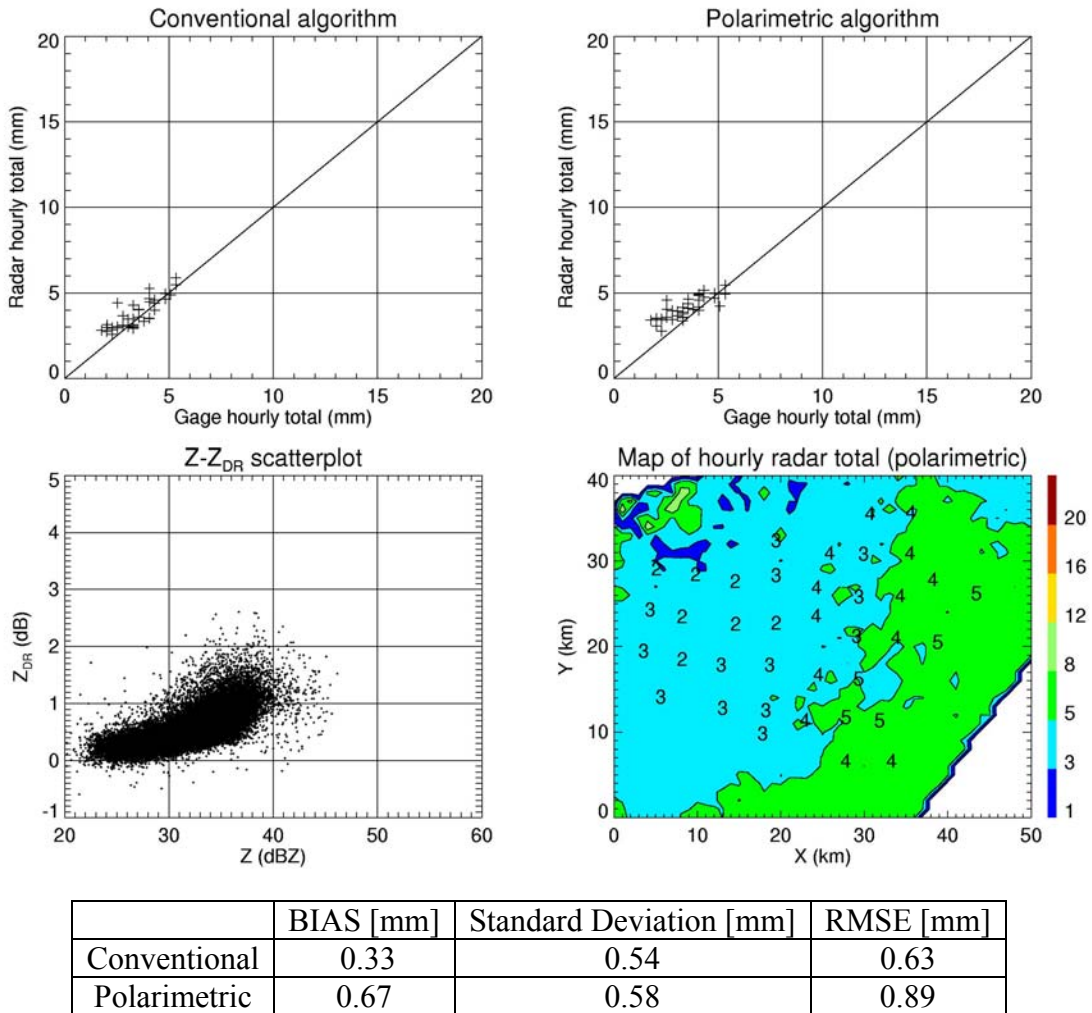
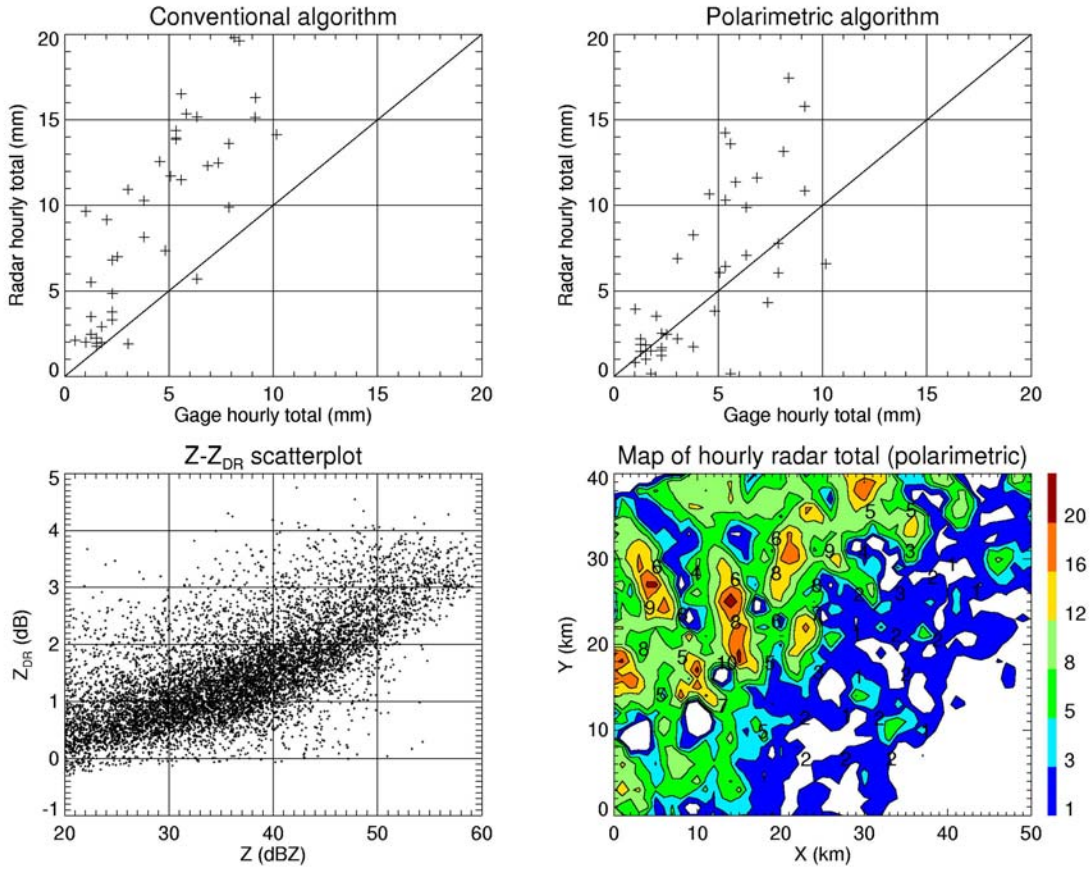


Fig. B32 – Hourly ARS gage totals versus estimates from the R(Z) and R(Z, K_{DP}, Z_{DR}) algorithm (top panels), a Z-Z_{DR} scattergram, and a map of the hourly radar rainfall totals with superimposed gage accumulations (bottom panels) for 4 December 2002 (1-2Z).

Leading edge of an intense squall line with trailing stratiform precipitation.



	BIAS [mm]	Standard Deviation [mm]	RMSE [mm]
Conventional	4.79	3.53	5.96
Polarimetric	1.42	3.35	3.64

Fig. B33 – Hourly ARS gage totals versus estimates from the R(Z) and R(Z, K_{DP} , Z_{DR}) algorithm (top panels), a Z- Z_{DR} scattergram, and a map of the hourly radar rainfall totals with superimposed gage accumulations (bottom panels) for 19 April 2003 (11-12Z).

Trailing stratiform precipitation associated with the rear edge of a squall line passing through central Oklahoma.

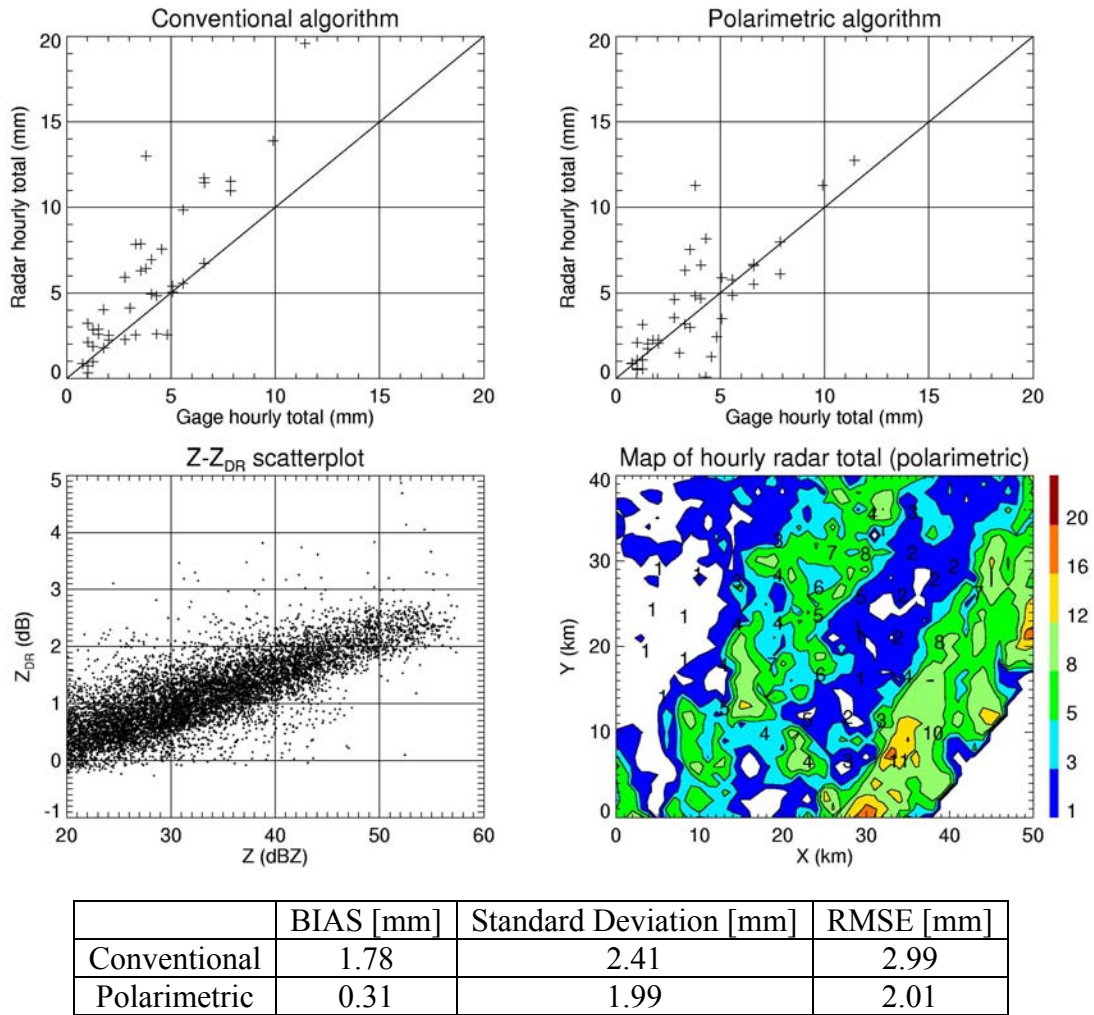


Fig. B34 – Hourly ARS gage totals versus estimates from the $R(Z)$ and $R(Z, K_{DP}, Z_{DR})$ algorithm (top panels), a $Z-Z_{DR}$ scattergram, and a map of the hourly radar rainfall totals with superimposed gage accumulations (bottom panels) for 19 April 2003 (12-13Z).

Isolated intense convective cell in advance of a developing squall line.

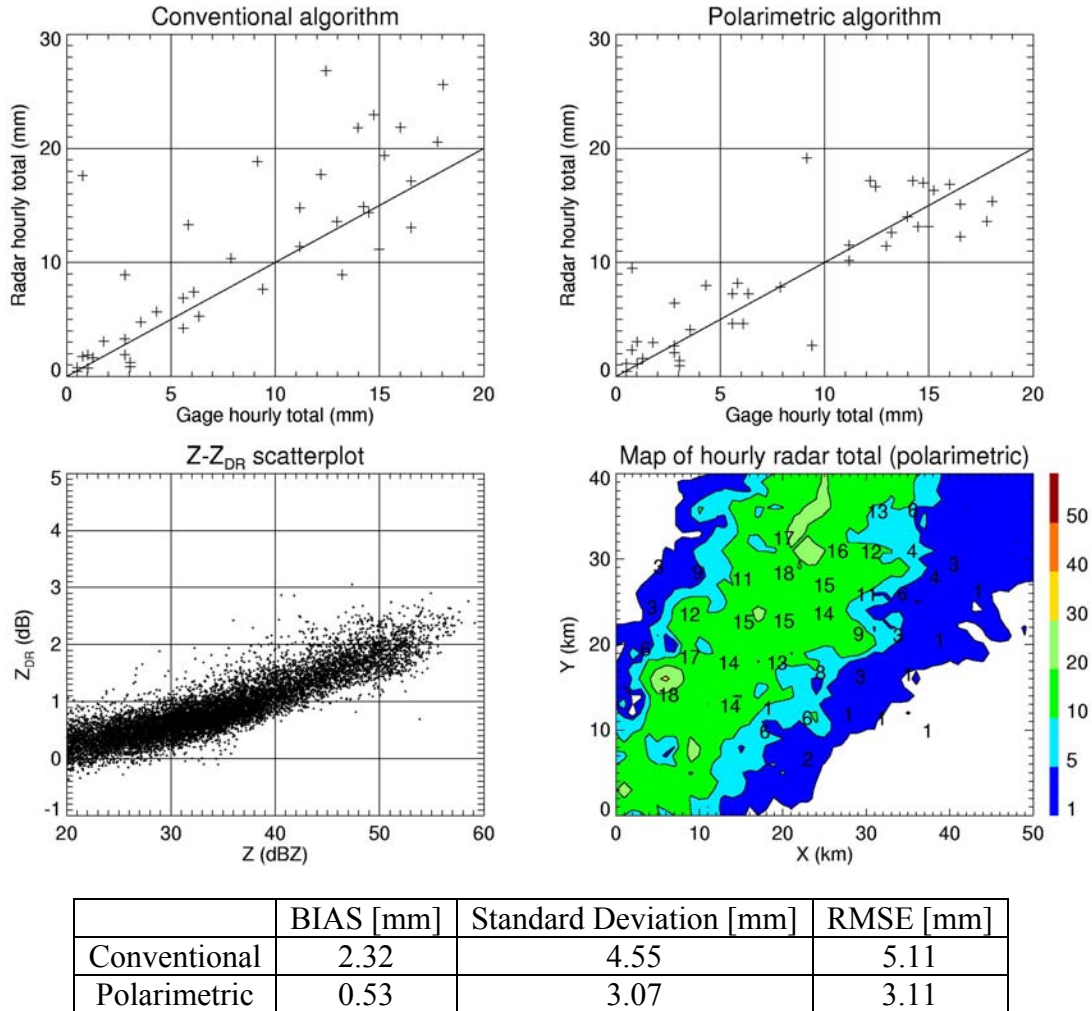


Fig. B35 – Hourly ARS gage totals versus estimates from the R(Z) and R(Z, K_{DP} , Z_{DR}) algorithm (top panels), a Z- Z_{DR} scattergram, and a map of the hourly radar rainfall totals with superimposed gage accumulations (bottom panels) for 23 April 2003 (22-23Z).

Intense convective cell with large hail observed.

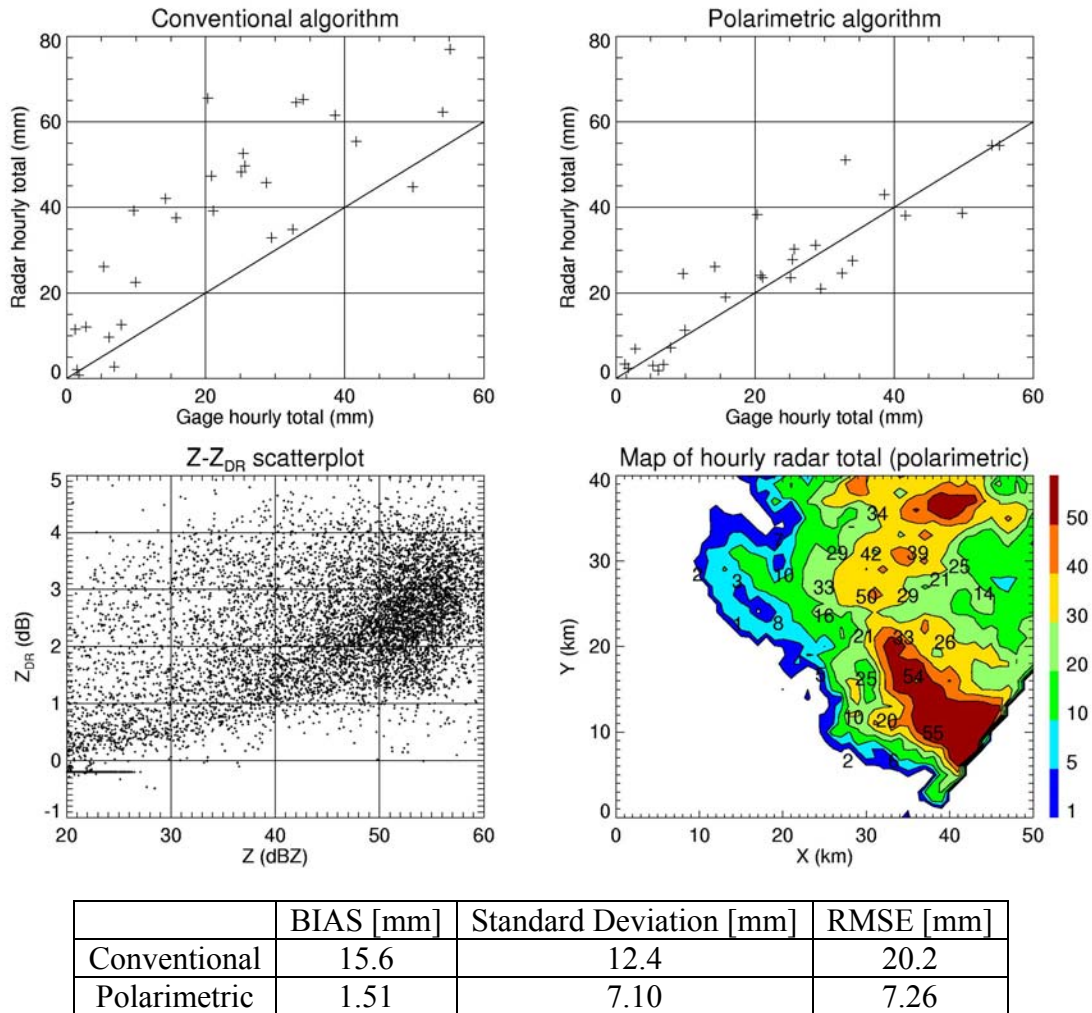


Fig. B36 – Hourly ARS gage totals versus estimates from the R(Z) and R(Z, K_{DP}, Z_{DR}) algorithm (top panels), a Z-Z_{DR} scattergram, and a map of the hourly radar rainfall totals with superimposed gage accumulations (bottom panels) for 14 May 2003 (7-8Z).

Intense convective cell with large hail observed.

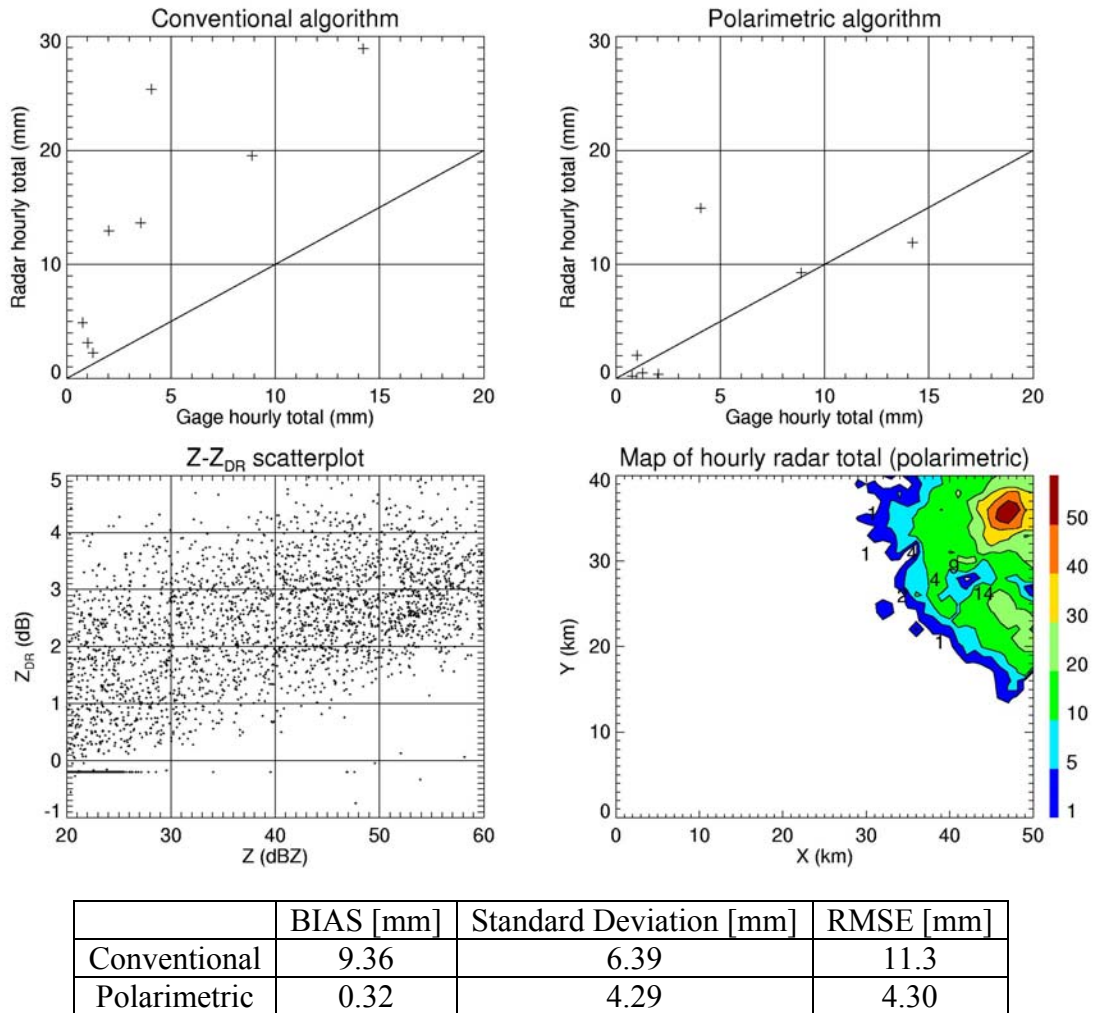


Fig. B37 – Hourly ARS gage totals versus estimates from the $R(Z)$ and $R(Z, K_{DP}, Z_{DR})$ algorithm (top panels), a $Z-Z_{DR}$ scattergram, and a map of the hourly radar rainfall totals with superimposed gage accumulations (bottom panels) for 14 May 2003 (8-9Z).

Developing convective cells with large hail observed over central Oklahoma.

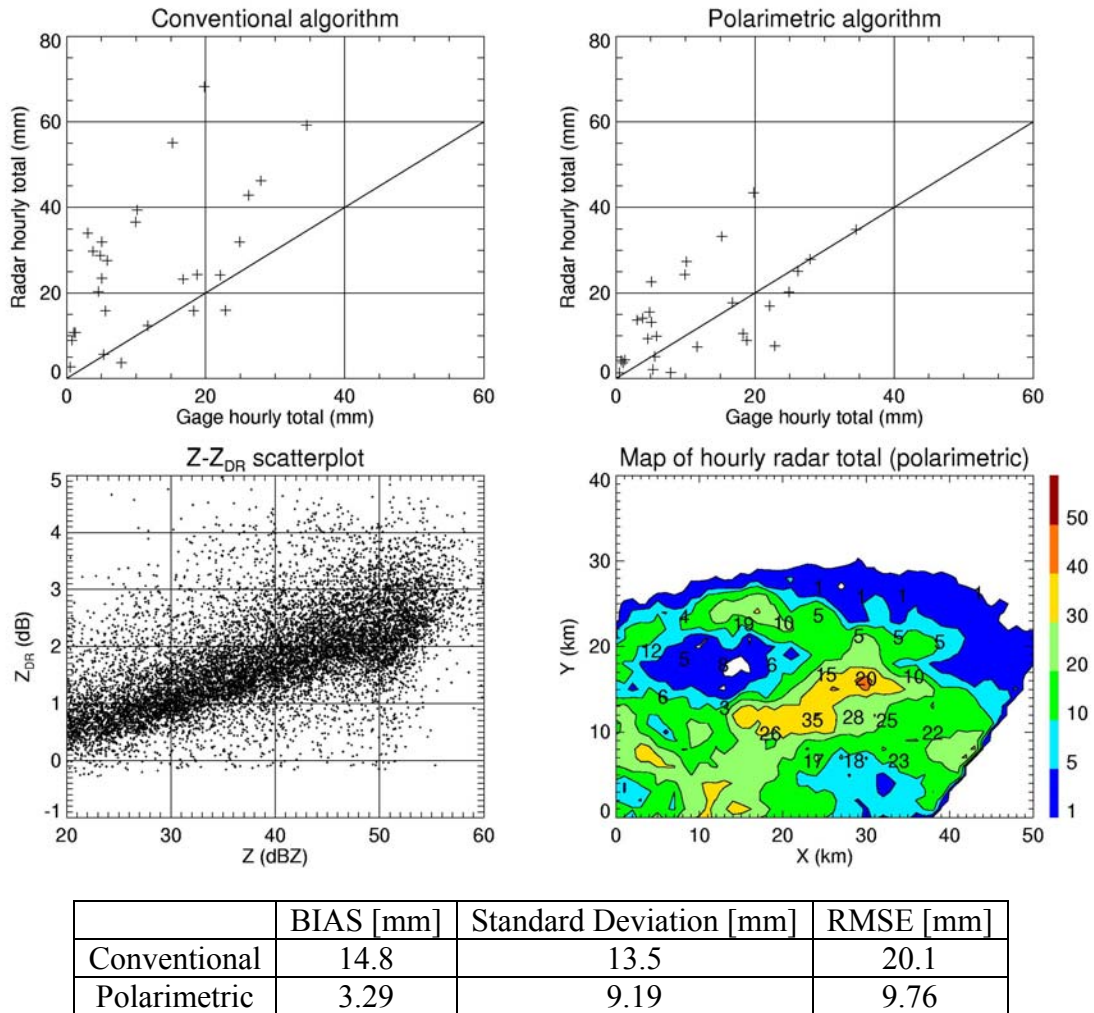


Fig. B38 – Hourly ARS gage totals versus estimates from the R(Z) and R(Z, K_{DP}, Z_{DR}) algorithm (top panels), a Z-Z_{DR} scattergram, and a map of the hourly radar rainfall totals with superimposed gage accumulations (bottom panels) for 20 May 2003 (2-3Z).

Mature convective cells with large hail over central Oklahoma.

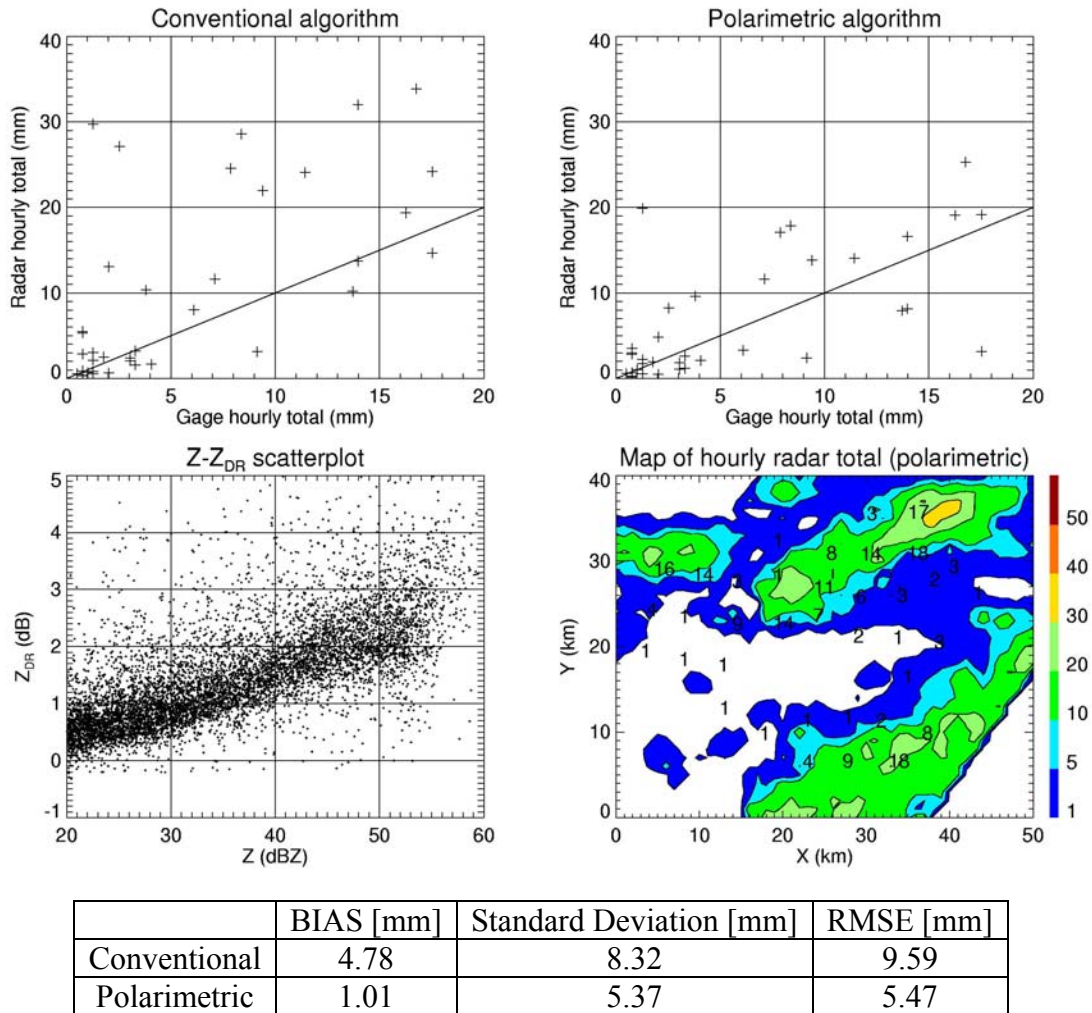
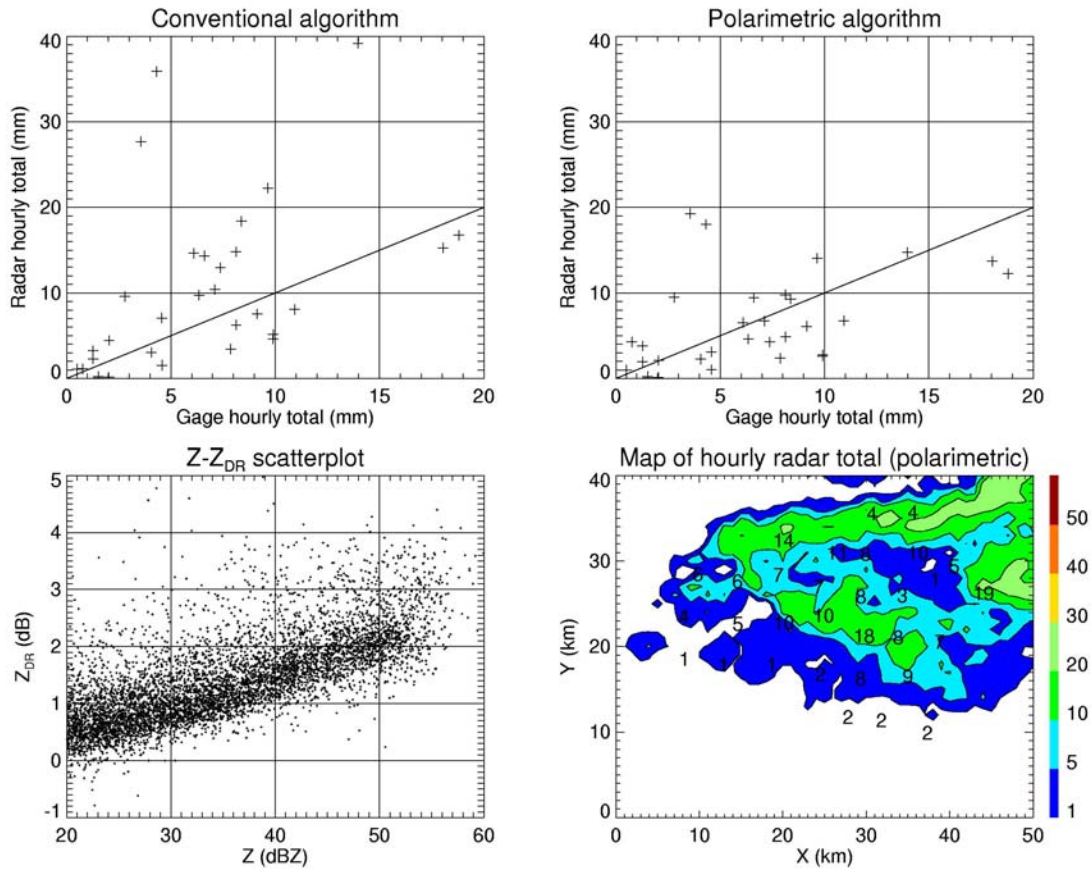


Fig. B39 – Hourly ARS gage totals versus estimates from the R(Z) and R(Z, K_{DP}, Z_{DR}) algorithm (top panels), a Z-Z_{DR} scattergram, and a map of the hourly radar rainfall totals with superimposed gage accumulations (bottom panels) for 20 May 2003 (3-4Z).

Mature convective cells with large hail over central Oklahoma.



	BIAS [mm]	Standard Deviation [mm]	RMSE [mm]
Conventional	3.74	8.73	9.49
Polarimetric	-0.12	5.01	5.01

Fig. B40 – Hourly ARS gage totals versus estimates from the R(Z) and R(Z, K_{DP}, Z_{DR}) algorithm (top panels), a Z-Z_{DR} scattergram, and a map of the hourly radar rainfall totals with superimposed gage accumulations (bottom panels) for 20 May 2003 (4-5Z).

Precipitation associated with the northern edge of a developing MCS over southern Oklahoma/north Texas.

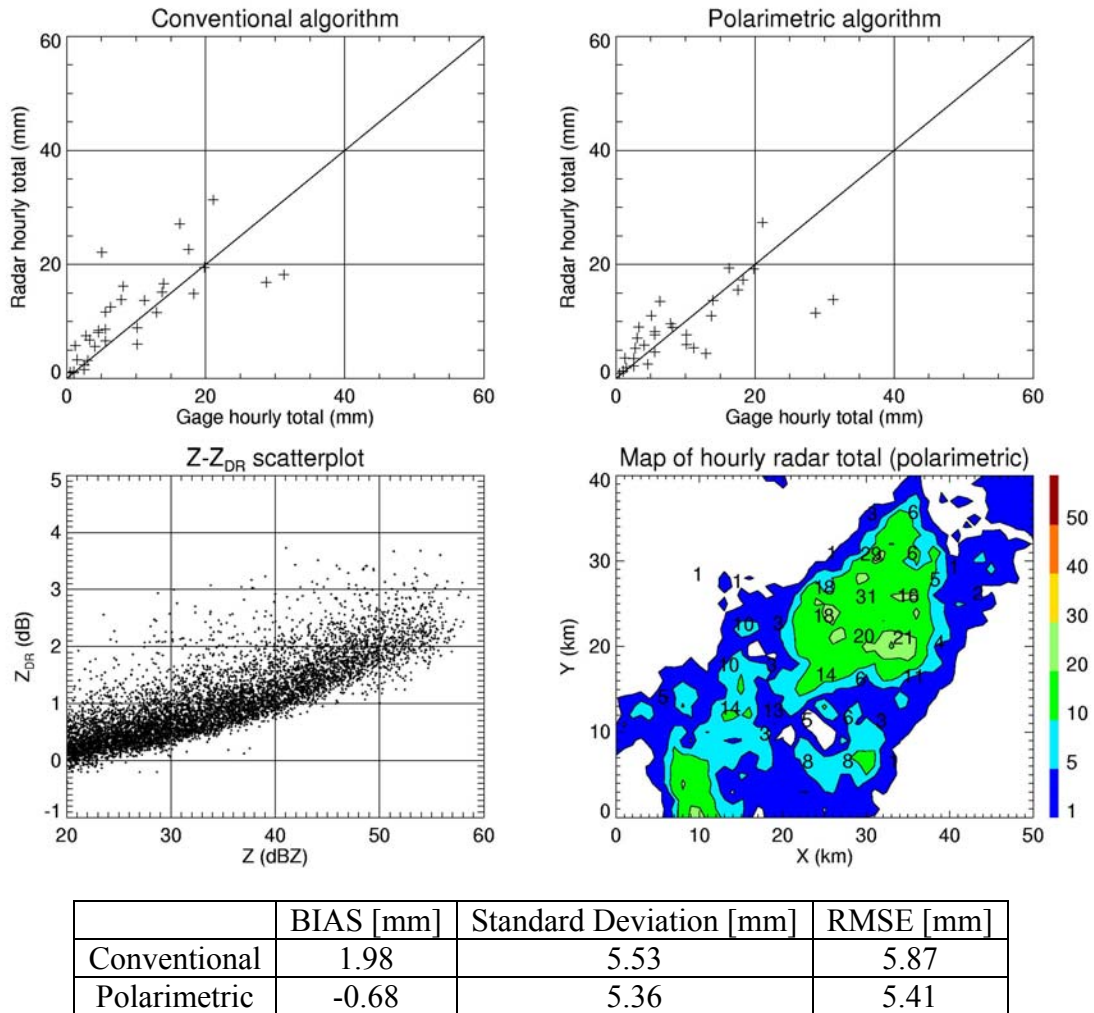


Fig. B41 – Hourly ARS gage totals versus estimates from the R(Z) and R(Z, K_{DP}, Z_{DR}) algorithm (top panels), a Z-Z_{DR} scattergram, and a map of the hourly radar rainfall totals with superimposed gage accumulations (bottom panels) for 5 June 2003 (10-11Z).

Precipitation associated with the northern edge of a developing MCS over southern Oklahoma/north Texas.

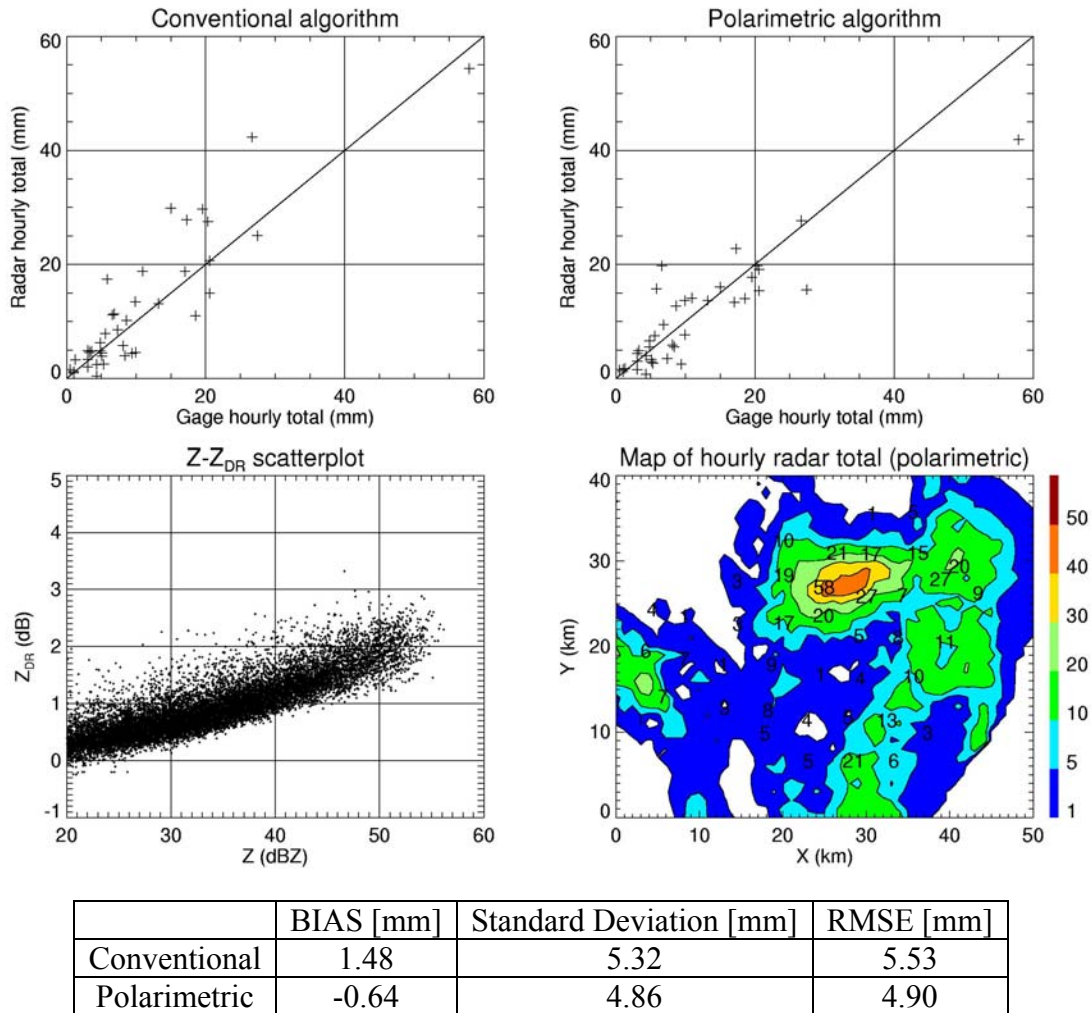


Fig. B42 – Hourly ARS gage totals versus estimates from the R(Z) and R(Z, K_{DP}, Z_{DR}) algorithm (top panels), a Z-Z_{DR} scattergram, and a map of the hourly radar rainfall totals with superimposed gage accumulations (bottom panels) for 5 June 2003 (11-12Z).

Precipitation associated with the northern edge of a developing MCS over southern Oklahoma/north Texas.

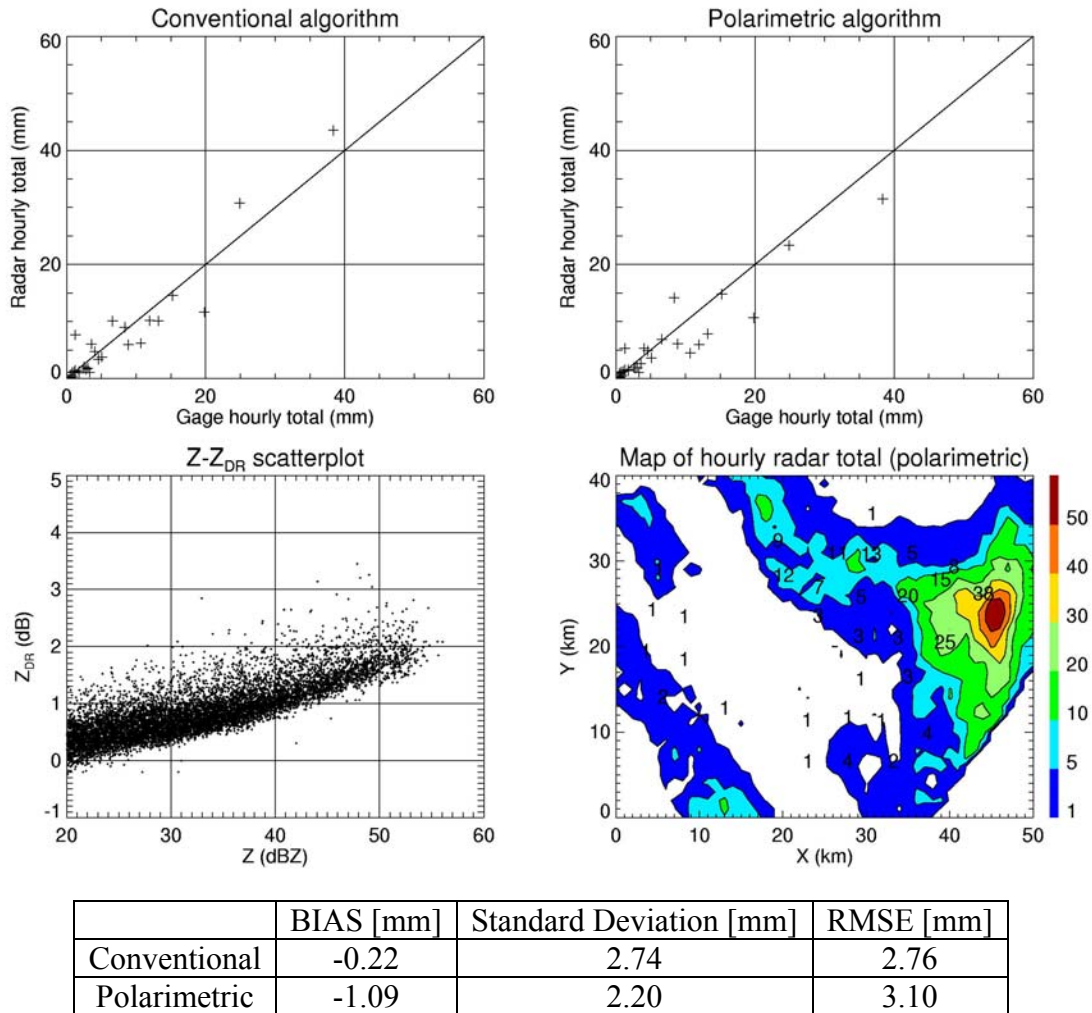


Fig. B43 – Hourly ARS gage totals versus estimates from the R(Z) and R(Z, K_{DP}, Z_{DR}) algorithm (top panels), a Z-Z_{DR} scattergram, and a map of the hourly radar rainfall totals with superimposed gage accumulations (bottom panels) for 5 June 2003 (12-13Z).

Precipitation associated with the northern edge of a developing MCS over southern Oklahoma/north Texas.

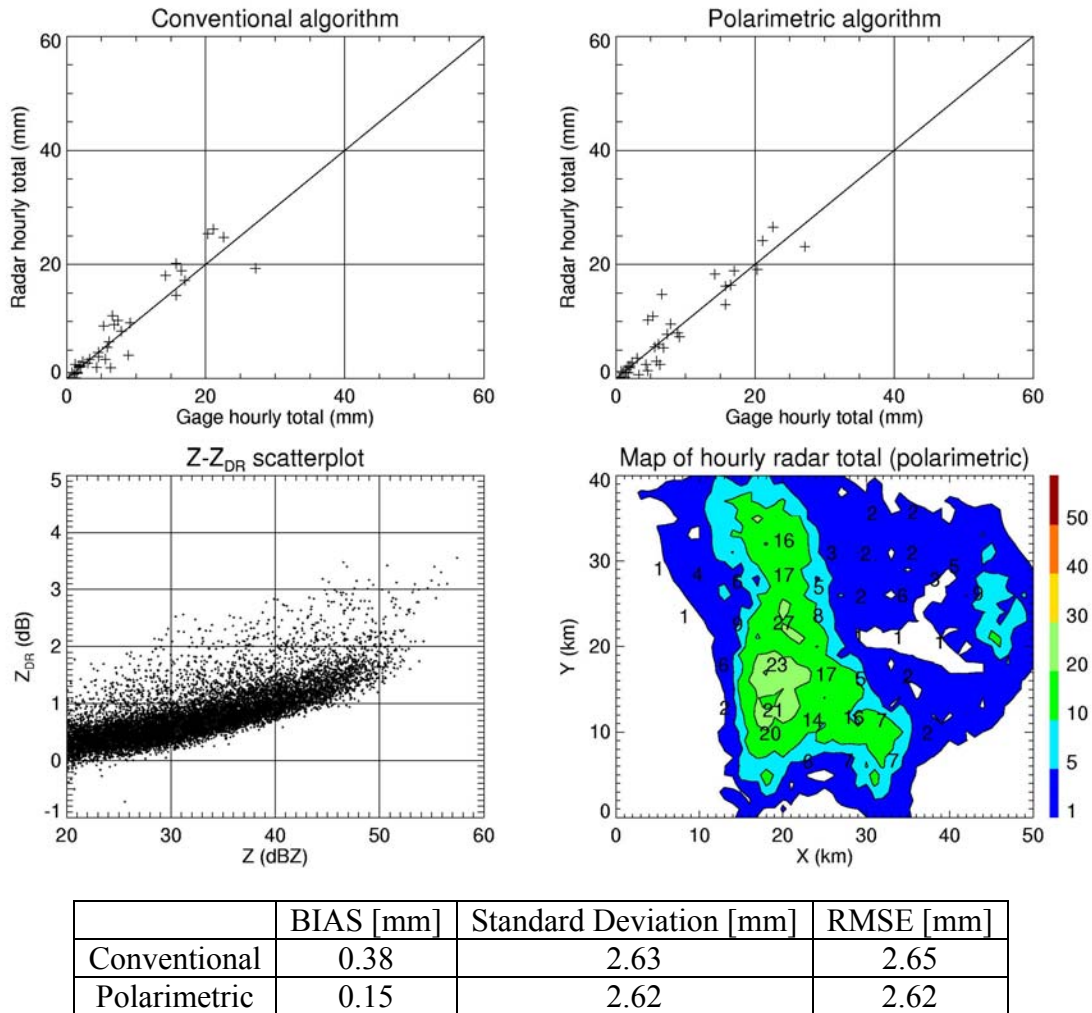
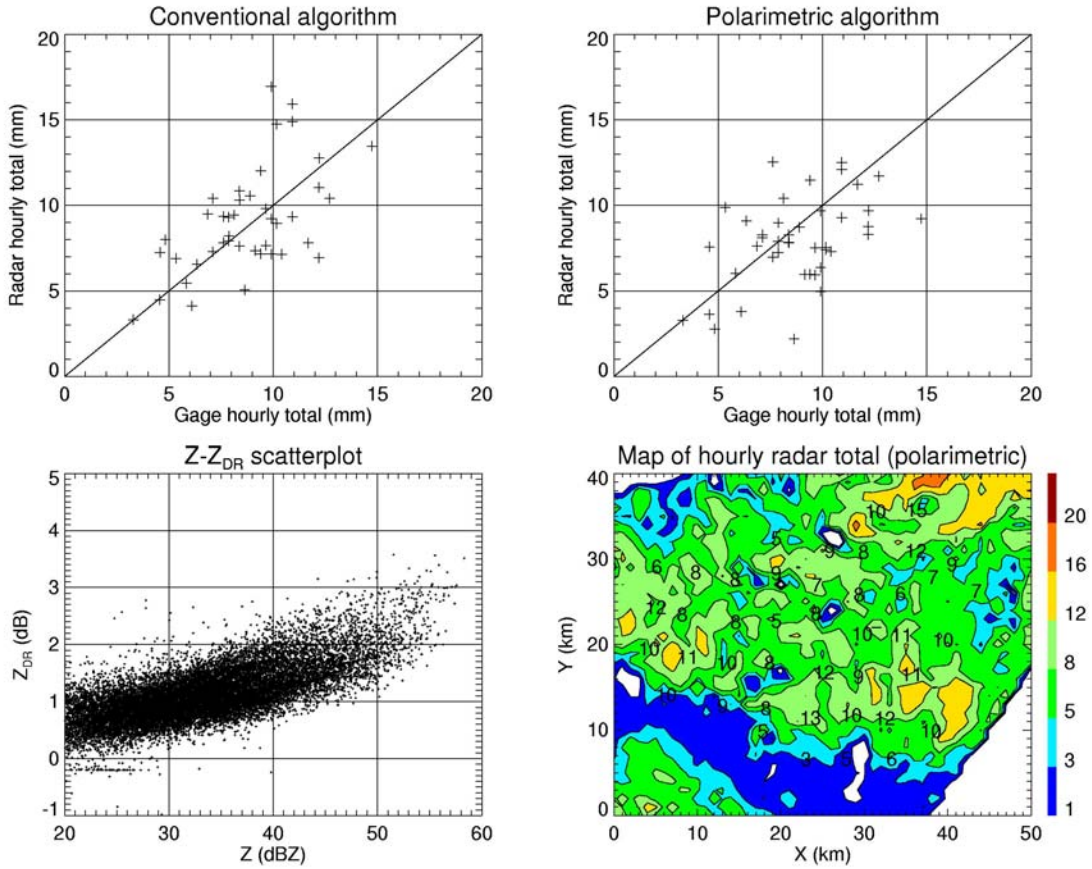


Fig. B44 – Hourly ARS gage totals versus estimates from the R(Z) and R(Z, K_{DP} , Z_{DR}) algorithm (top panels), a Z- Z_{DR} scattergram, and a map of the hourly radar rainfall totals with superimposed gage accumulations (bottom panels) for 5 June 2003 (14-15Z).

Leading edge of an intense squall line passing through central Oklahoma.



	BIAS [mm]	Standard Deviation [mm]	RMSE [mm]
Conventional	0.30	2.56	2.58
Polarimetric	-0.85	2.54	2.68

Fig. B45 – Hourly ARS gage totals versus estimates from the R(Z) and R(Z, K_{DP}, Z_{DR}) algorithm (top panels), a Z-Z_{DR} scattergram, and a map of the hourly radar rainfall totals with superimposed gage accumulations (bottom panels) for 6 June 2003 (3-4Z).

Convective and stratiform precipitation associated with a squall line passing through central Oklahoma.

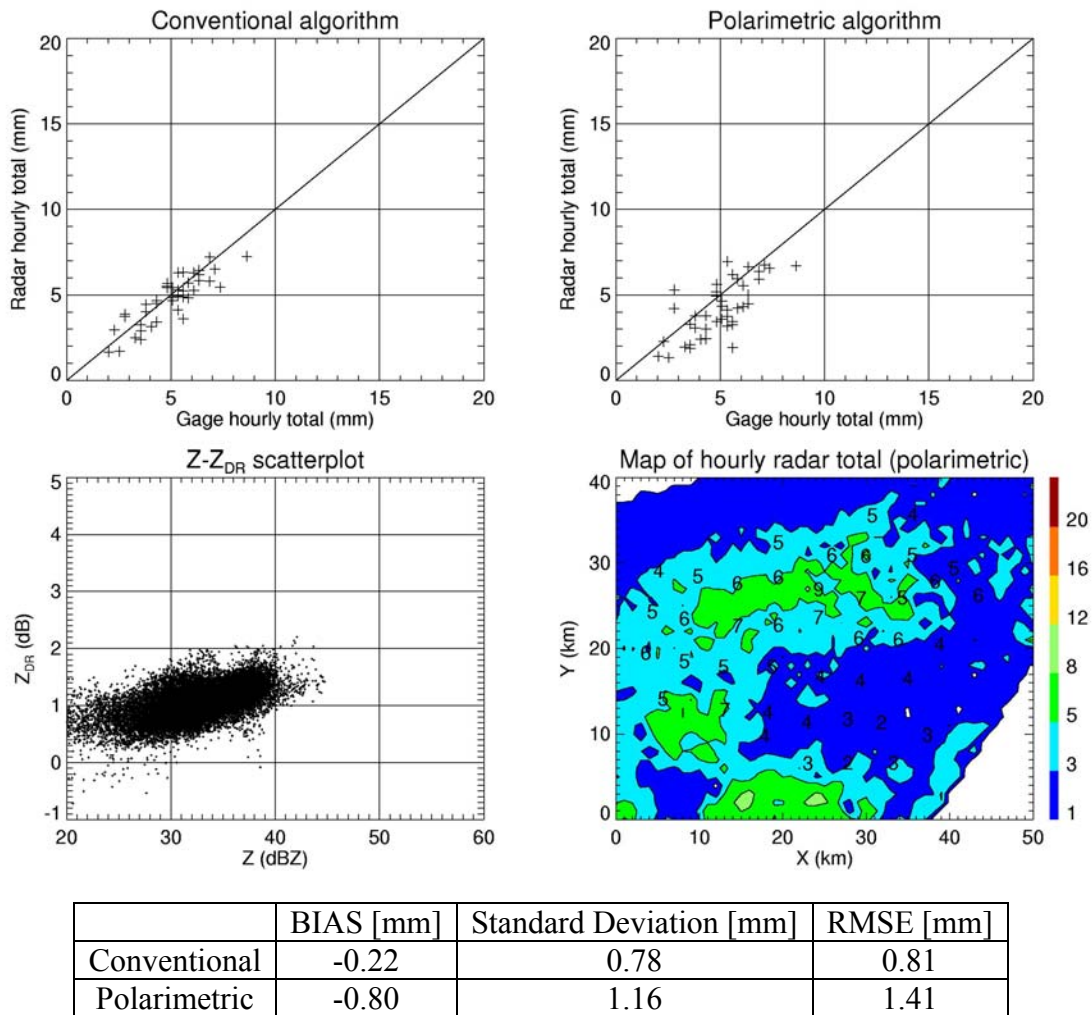


Fig. B46 – Hourly ARS gage totals versus estimates from the R(Z) and R(Z, K_{DP}, Z_{DR}) algorithm (top panels), a Z-Z_{DR} scattergram, and a map of the hourly radar rainfall totals with superimposed gage accumulations (bottom panels) for 6 June 2003 (4-5Z).

Predominantly stratiform precipitation associated with the rear edge of a squall line passing through central Oklahoma.

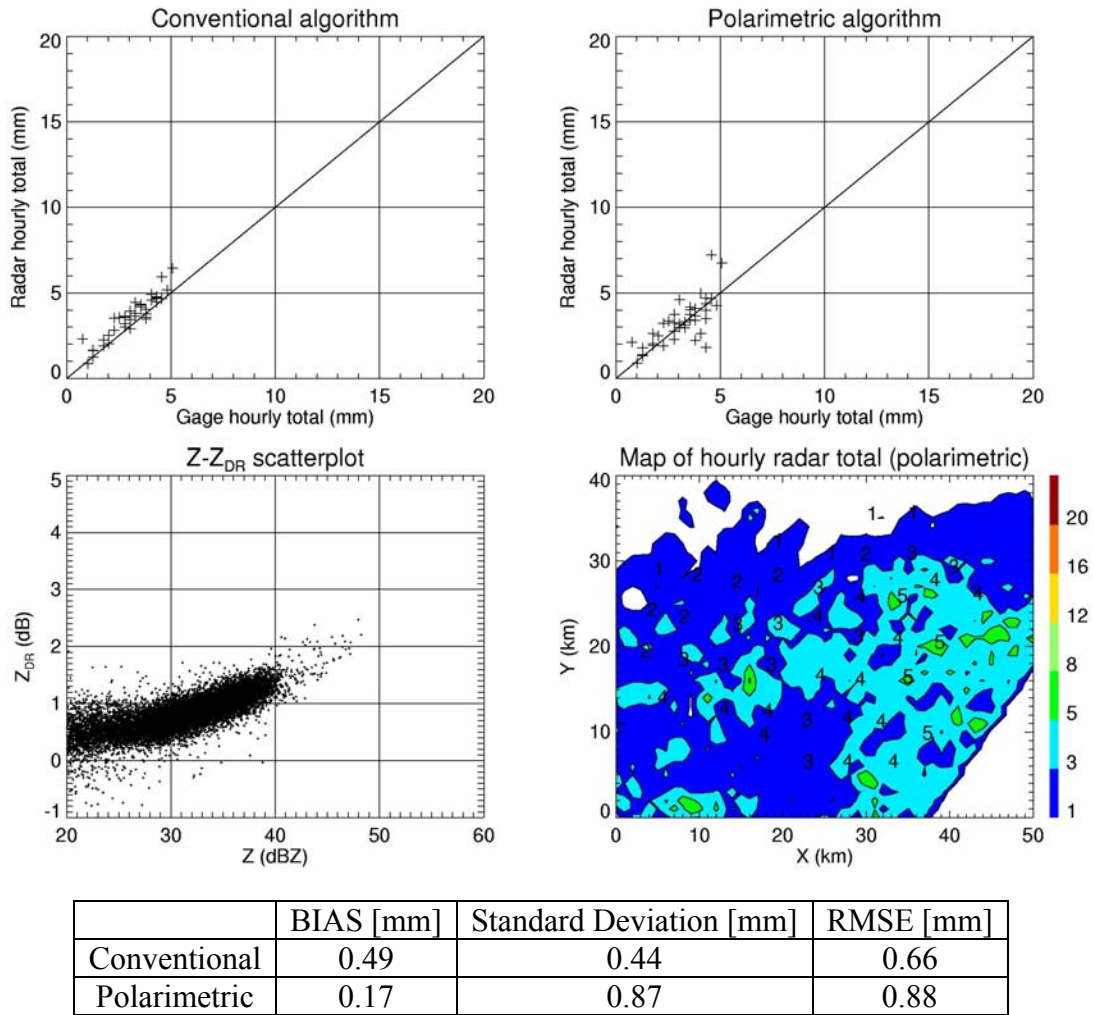


Fig. B47 – Hourly ARS gage totals versus estimates from the R(Z) and R(Z, K_{DP}, Z_{DR}) algorithm (top panels), a Z-Z_{DR} scattergram, and a map of the hourly radar rainfall totals with superimposed gage accumulations (bottom panels) for 6 June 2003 (5-6Z).

Mature convective cell with large hail over the observation network.

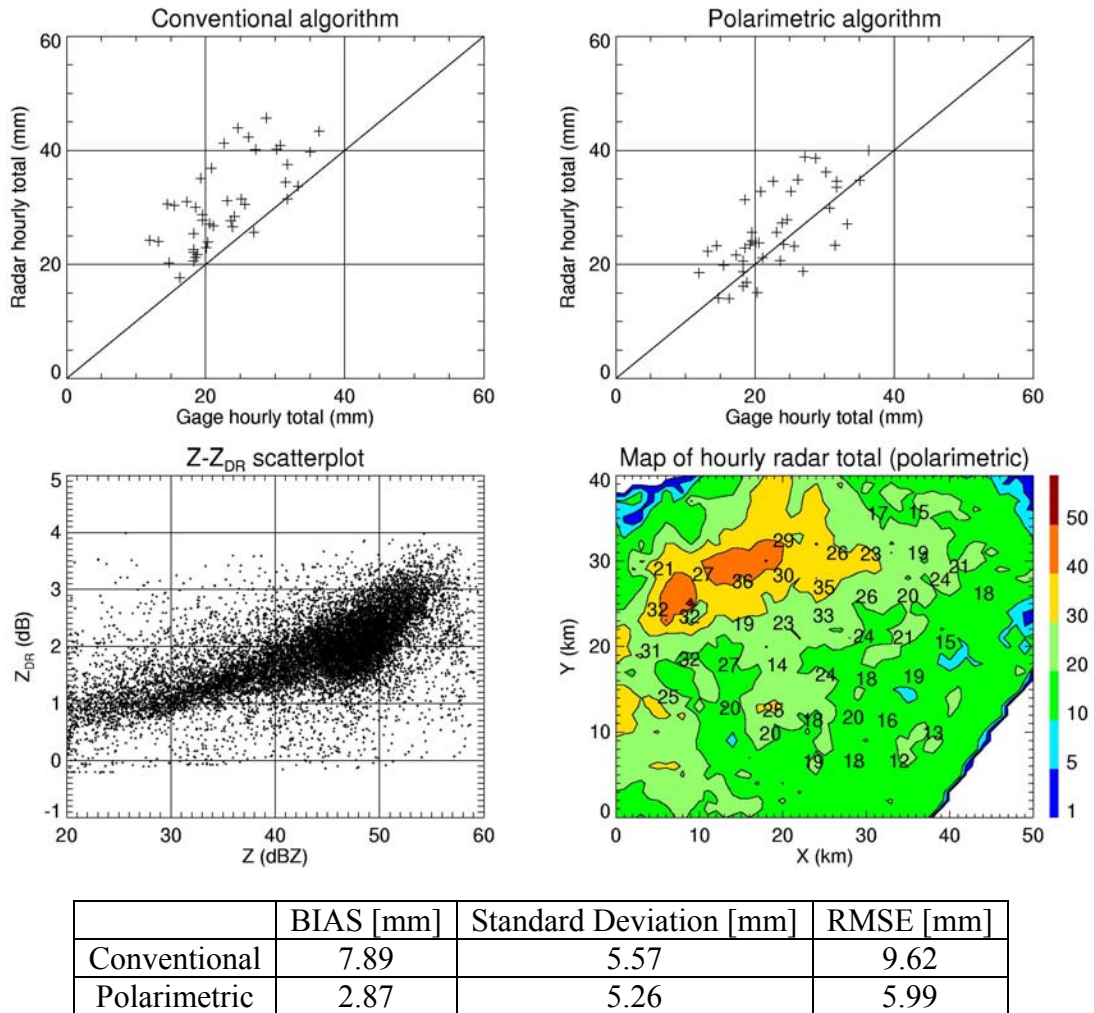


Fig. B48 – Hourly ARS gage totals versus estimates from the R(Z) and R(Z, K_{DP}, Z_{DR}) algorithm (top panels), a Z-Z_{DR} scattergram, and a map of the hourly radar rainfall totals with superimposed gage accumulations (bottom panels) for 12 June 2003 (2-3Z).

Developing convective cell over the observation network.

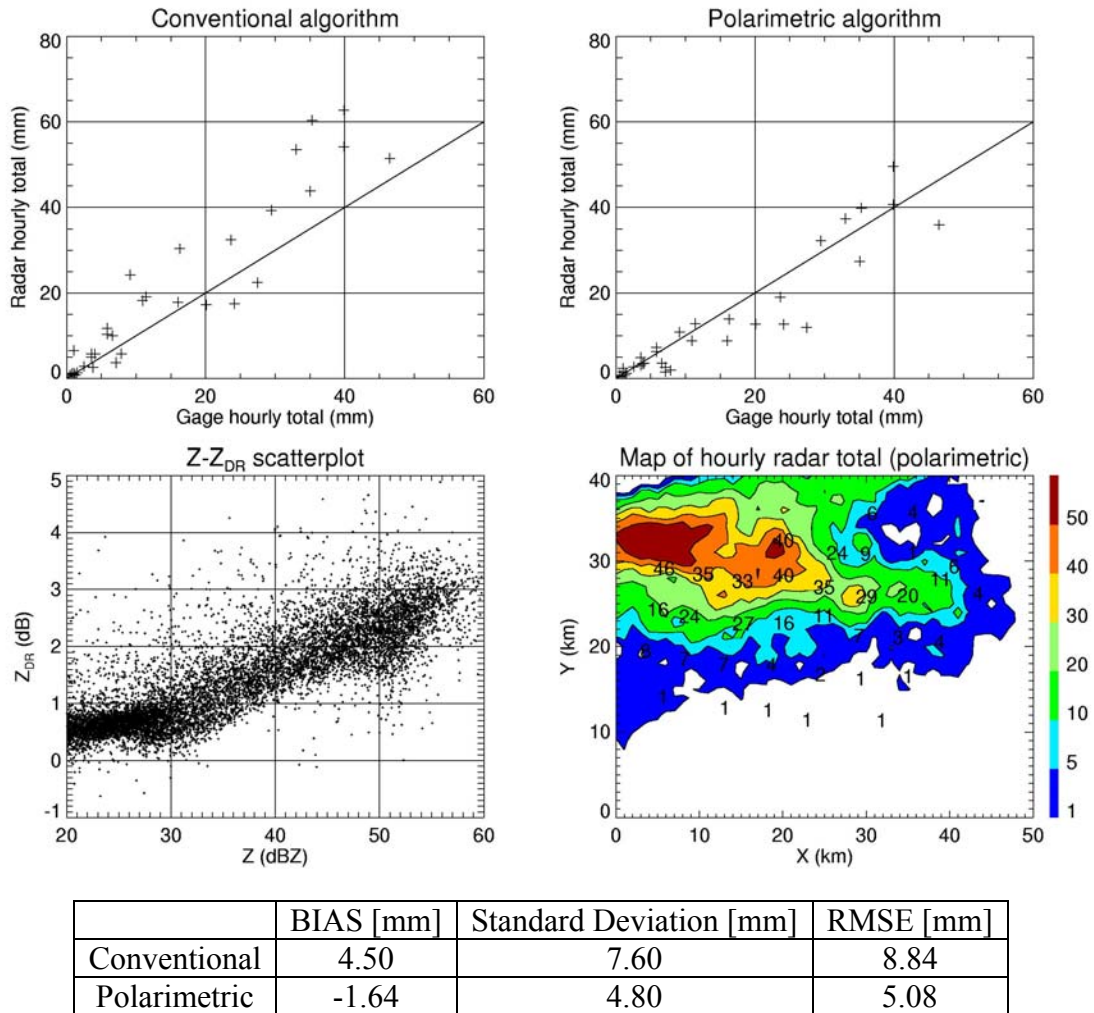


Fig. B49 – Hourly ARS gage totals versus estimates from the R(Z) and R(Z, K_{DP}, Z_{DR}) algorithm (top panels), a Z-Z_{DR} scattergram, and a map of the hourly radar rainfall totals with superimposed gage accumulations (bottom panels) for 13 June 2003 (11-12Z).

Convective cell over the observation network with additional scattered weak precipitation.

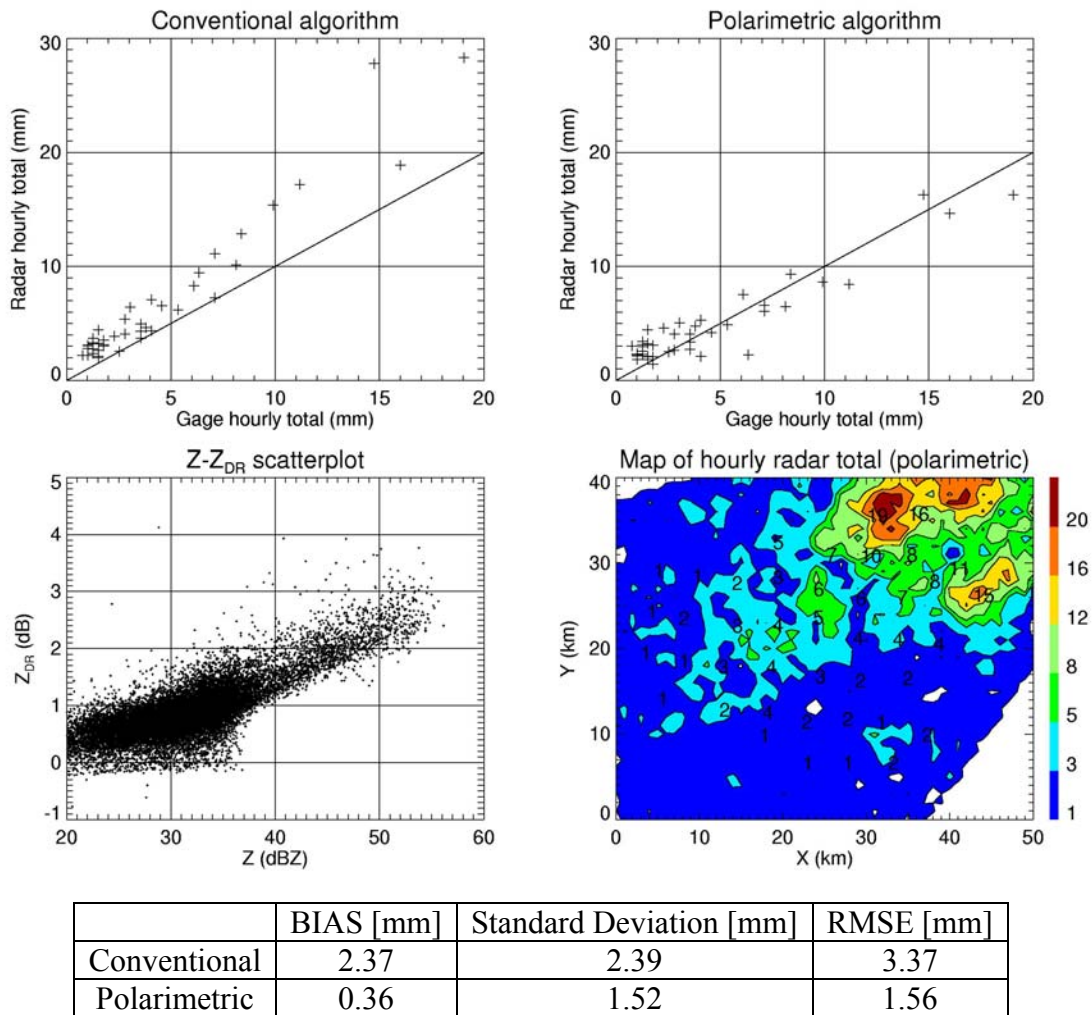


Fig. B50 – Hourly ARS gage totals versus estimates from the R(Z) and R(Z, K_{DP}, Z_{DR}) algorithm (top panels), a Z-Z_{DR} scattergram, and a map of the hourly radar rainfall totals with superimposed gage accumulations (bottom panels) for 13 June 2003 (12-13Z).